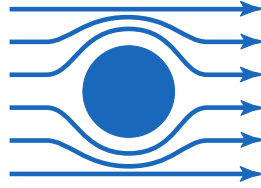




Technische
Universität
München



Walther-Meißner
Institut



Bayerische
Akademie
der Wissenschaften

Superconductor/Ferromagnet Heterostructures for Superconducting Spintronics

Master's thesis
Manuel Müller

Advisor: Prof. Dr. Rudolf Gross
Supervisor: Dr. Matthias Althammer
Garching – November 29, 2019

Contents

1	Introduction	1
2	Sample Fabrication	5
2.1	Magnetron sputter deposition process	5
2.1.1	Operation principle of magnetron sputtering	5
2.1.2	Sample fabrication at the Superbowl	7
2.1.3	Optimization parameters	8
2.1.4	Our sample fabrication process	9
2.2	X-Ray reflectometry	9
2.2.1	Operation principle	9
2.2.2	Results of XRD-reflectometry	10
3	Theoretical concepts	13
3.1	Properties of superconducting thin films	13
3.1.1	Basics of superconductivity	13
3.1.2	Definition of the quasiparticle spin susceptibility χ_s	15
3.2	Key aspects of ferromagnetic resonance	18
3.2.1	Magnetization dynamics	18
3.2.2	Ferromagnetic resonance	19
3.2.3	Spin pumping	22
3.3	Spin pumping into superconductors	23
4	Experimental procedure	25
4.1	Experimental technique	25
4.2	Measurement procedure	27
4.3	Experimental setup	29
5	Coherence peak in SC/FM-multilayers	31
5.1	In-plane-BBFMR results of NbN/Co ₂₅ Fe ₇₅ -multiayer sample series	31
5.2	BBFMR results at cryogenic temperatures	33
5.3	Detection of the superconducting coherence peak	35
6	Manifestations of superconductivity in VNA-based BBFMR	39
6.1	Effect of superconducting layers on complex transmission parameter $ S_{21} $	39
6.2	Effect on the inductive coupling strength L_0	41
6.3	Results for FM/SC-bilayers using different superconductors	46
7	Spin-Orbit Torques in SC/FM heterostructures	49
7.1	Magnetization dynamics parameters of the samples below T_C	51
7.2	Results for Spin-Orbit Torques in SC/FM-heterostructures	53
7.2.1	Results in the normalconducting range	53
7.2.2	Results in the superconducting range	56
7.3	Concluding remarks	65

8	Summary	69
8.1	Superconducting coherence peak in NbN/Co ₂₅ Fe ₇₅ -multilayers	69
8.2	Manifestations of superconductivity in VNA-based BBFMR	70
8.3	Inductive detection of Spin-Orbit Torques in SC/FM heterostructures	70
9	Outlook	73
A	Appendix: Sample Fabrication	77
A.1	Sputtering parameters	77
A.2	Fabrication of the superconducting spin valves	78
A.2.1	The first step	78
A.2.2	The second step	79
A.2.3	The third step	80
B	Appendix: Miscellaneous Results	83
B.1	Mathematica code	83
B.2	Additional coherence peaks for NbN/Co ₇₅ Fe ₂₅ -heterostructures	84
B.3	Raw data of the enhancement parameter for varying superconductors	85
B.4	Temperature dependence of results for NbN/Ni ₈₀ Fe ₂₀ -samples	86

1 Introduction

'Innovation is taking two things that already exist
and putting them together in a new way.'

Tom Freston

This famous quote by Tom Freston, pioneer in the field of cable television and founding member of MTV, holds true in many fields of science particularly in solid state physics, where the properties of materials can be finely tuned by bringing them into contact with one another and pave the way for innovative new technologies. Prominent examples include the generation of two-dimensional electron gases in semiconductor/insulator interfaces of metal oxide semiconductor field effect transistors [MOSFETs] [1], the fundamental building blocks of integrated circuits for computers and electronic devices, as well as the usage of the giant magnetoresistance effect [2, 3] in hard disk drives via the fabrication of FM/NM/FM-trilayer structures. A lesser known but equally fascinating example is the possibility of bringing ferromagnetic and superconducting materials into contact and investigating the changes in their respective properties. Initially, it was assumed that these structures would be impossible to realize as the magnetic stray field of the ferromagnet would lead to a suppression of the superconductivity in the adjacent layer [4], which was also substantiated experimentally by Matthias *et al.* [5]. However, later it was found that superconductivity and magnetism are not mutually exclusive and can even coexist in certain materials [6–8]. Additionally, the superconducting transition temperature T_C of SC/FM-bilayers is not necessarily diminished when compared to a pure SC, but rather exhibits oscillations as a function of the layer thickness of the ferromagnetic layer [9, 10]. In terms of innovative devices, several different experiments have been suggested and realized ranging from the alignment of superconductivity along ferromagnetic domain walls [11, 12] to store data, over ferromagnetic S/F/S-Josephson-junctions for the implementation of phase shifters and qubits [13–16], to the exploitation of magnetoresistive effects, where the T_C in F/S/F-spinvalve structures has been found to depend on the respective alignment of the magnetizations in the F-layers [17, 18]. Over the last decade, the field of SC/FM-interfaces has caught attention in the field of spintronics due to potentially beneficial spin transport properties of superconducting quasiparticles [19, 20] and possibly even the generation of spin-triplett cooper pairs [21–23], to reduce the heating effects commonly found in spintronics devices. While dc-transport experiments report changes in spin signal ΔR and spin diffusion length λ_s [24–26] in superconducting spin-valve structures below T_C , the nonequilibrium magnetization dynamics in the adjacent ferromagnetic layers and the corresponding changes in its magnetization dynamics parameters provide insight on dynamic spin injection into superconductors via spin pumping [27]. This master's thesis aims at detecting alterations in the properties of the ferromagnetic layer in FM/SC-heterostructures related to a change in spin pumping properties into the adjacent superconducting layer below the transition temperature via means of broadband ferromagnetic resonance experiments. To this end, NbN/Co₂₅Fe₇₅ heterostructures are grown by reactive DC-sputtering under ultra-high vacuum conditions and the ferromagnetic resonance of the Co₂₅Fe₇₅-layer is excited by placing the samples onto a coplanar waveguide. In particular, dramatically

enhanced spin transport properties in thermally excited superconducting quasiparticles are theoretically expected to occur slightly below T_C [19, 20, 28]. Hence, the spin pumping induced magnetization damping is studied as a function of temperature, especially in vicinity of the NbN superconducting transition temperature. Additionally, the used phase sensitive detection of the microwave transmission signal allows us to quantitatively extract the inductive coupling strength in these heterostructures and obtain additional information on spin current transport properties based on the method outlined in [29]. Most notably, it provides us with a new tool to investigate the inverse spin Hall effect in superconductors, which circumnavigates the problems of conventional voltage-based measurement techniques [30, 31] as this approach is exclusively sensitive to the spin-current-induced charge current flowing in the superconducting layer. The structure of this thesis is as follows:

We begin by illustrating the sample fabrication process by via dc magnetron sputtering in **chapter 2**. Furthermore, we present the results of XRD-measurements conducted on our samples to verify that the desired thicknesses of the respective layers have been achieved. Afterwards, we introduce the basics of both superconductivity and magnetization dynamics in an externally applied magnetic field H_{ext} in **chapter 3**. For the former we derive only its key properties required to describe our experimental results, spanning from the definition of its most fundamental parameters like London penetration depth λ_L and coherence length ξ_0 to the very specific so-called Bogoliubov-Valatin quasiparticles [BVQP] spin susceptibility χ_s [32, 33] derived from BCS-theory [34]. Thereafter, we turn our attention to the magnetization dynamics and discuss the ferromagnetic resonance observed when we apply an additional oscillating magnetic field perpendicular to the external H_{ext} . Its resulting response is described by the Polder susceptibility and we derive its resonance condition, the Kittel equation for different geometries. With its help we can extract the magnetization dynamics parameters. In particular, we are interested in the Gilbert damping α as we show that it can be a measure of spin currents injected from the FM into adjacent layers via spin pumping. We conclude this chapter by discussing the spin pumping properties of superconductors as function of temperature.

The experimental procedure of conducting VNA-based broadband ferromagnetic resonance [BBFMR] is described in theory and experiment in **chapter 4**. Furthermore, we show the conducted data processing steps to extract the magnetization dynamics parameters.

We then start the discussion of our experimental results by presenting our efforts to detect and quantify changes in the magnetization dynamics parameters of NbN/Co₂₅Fe₇₅-thin films, when cooled below their superconducting transition temperature in the CHAOS-cryostat in **chapter 5**. Our detection of a minor coherence peak in the Gilbert damping α is its focal point and we illustrate our attempts to quantify and compare it to the theoretical calculations in [19].

In **chapter 6**, we discuss how the exotic properties of a superconductor like its perfect conductance or expulsion of magnetic fields impact key measurement quantities in VNA-based BBFMR. We show and quantify how the former alters the magnitude of the complex transmission parameter $|S_{21}|$. Finally, we illustrate how the expulsion of the oscillatory magnetic driving field \mathbf{h}_{rf} in the superconducting layer can either enhance or reduce the inductive coupling strength L_0 between sample and CPW and consequently the FMR amplitude.

In **chapter 7**, we use an inductive measurement technique [29] to detect and quantify field- and damping-like inverse spin-orbit torques [iSOT] in both the normal and superconducting state of $\text{Ni}_{80}\text{Fe}_{20}/\text{NbN}$ -bilayers. The necessary data procedure steps to extract the related spin orbit torque conductivities are outlined and we discuss how the existing method has to be adapted for superconducting materials. Surprisingly, we report dramatic changes in both field- and damping-like iSOT below T_C and attempt to relate these results to both superconducting parameters following BCS-theory as well as existing research in this field. Consequently, we are able to relate changes in the former to the so-called quasiparticle mediated inverse spin Hall effect [QMISHE] [30], while changes in the latter have to our knowledge not been reported yet. However, we are able to relate this result to a Rashba-like confinement of electrons at the SC/FM-interface by the BCS-gap parameter Δ .

Chapter 8 provides a compact overview of the most important research results of this thesis.

Finally, **chapter 9** enlists questions that are still left unanswered and suggests further successive research projects which could not be realized within the limited timespan of this master's thesis. As an example we show our first experimental results for a GMR spin valve grown on top of a superconducting bar, where we attempted the dissipationless switching of the ferromagnetic magnetization mediated by field-like spin-orbit torques by applying superconducting charge currents.

2 Sample Fabrication

This chapter is dedicated to the fabrication process of our superconductor/ferromagnet-heterostructures via means of dc sputtering in the Superbowl ultra-high-vacuum machine. Both the general dc sputtering process and the versatile features of the Superbowl, which make it a suitable tool to grow these special samples, are described. Lastly, we illustrate how we applied X-ray reflectometry by elastic scattering of high energy photons to determine the real thicknesses of the individual layers and obtain information on both their potential crystallographic order as well as surface roughness.

2.1 Magnetron sputter deposition of NbN/Co₂₅Fe₇₅-heterostructures

The growth of functional high quality superconductor-ferromagnet-heterostructures imposes high demands on the used ultra high vacuum machine as an in situ deposition of both layers is favourable for clean SC/FM-interfaces. Hence it must be able to offer optimal growth conditions for both a low-damping ferromagnetic metal for BBFMR as well as a resilient superconductor able to maintain a transition temperature T_C above the boiling point of liquid helium [4.2 K] for low temperature measurements in a liquid helium cryostat. However, ferromagnetic contamination has a detrimental effect on the superconducting target material, which requires the spatially separate growth of ferromagnetic and superconducting layers. This contradiction is solved in the Superbowl ultra-high-vacuum machine by enabling the growth of both ferromagnetic and non-magnetic/superconducting materials in two separate deposition chambers as illustrated in Fig. 2.1. We use the SP2 chamber to grow superconducting NbN and then transfer the sample through the evacuated loadlock into the SP4 chamber to grow the low-damping ferromagnet Co₂₅Fe₇₅.

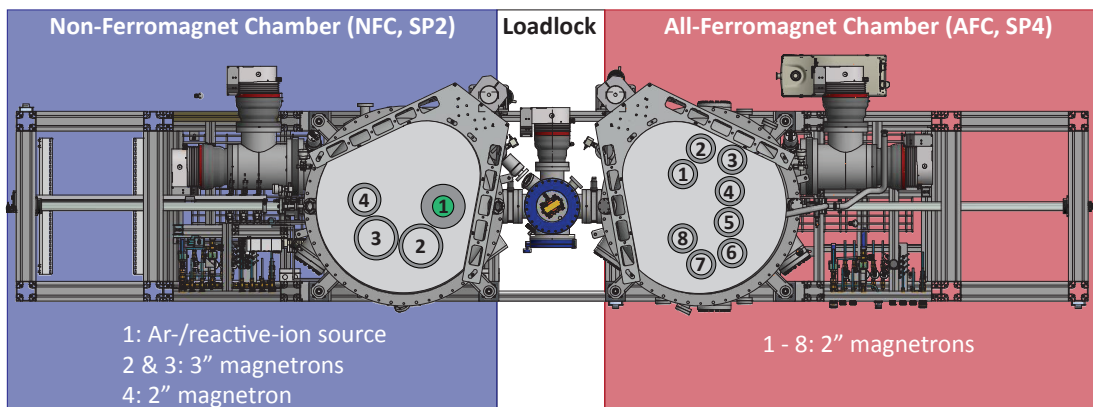


Figure 2.1: Sketch of the Superbowl sputtering machine. Taken from [35].

2.1.1 Operation principle of magnetron sputtering

The deposition of thin films in the Superbowl is realized via dc magnetron sputtering, where a dc voltage of several hundred volts is applied between the target material and an anode ring to accelerate positively charged ions of the injected inert gas [e.g. Argon] and thereby ignite a plasma state. These ions are then accelerated towards the target material, collide with it and lead to the ejection of atoms or even small material clusters from its sur-

face, which evaporate into the sputtering chamber and subsequently adhere to the sample surface [35,36]. This process is illustrated in Fig. 2.2. However, this is only possible, if the ejected target material is not scattered with further inert gas ions before reaching the substrate and hence requires low gas pressures during the sputtering process. Yet at the same time, a sufficient gas pressure is needed to maintain the ionic plasma leading to less ionized atoms as collision partners for the sputtering process of the target material and thereby also lowers the deposition rate. This problem is solved by the magnetron sputtering technique, where the electric field between target material cathode and anode is superimposed with a transversal magnetic field generated by permanent magnets mounted underneath the target, which exerts a Lorentz force on electrons ejected from the ionized gas and forces them on a helical path on their way towards the anode ring. This elongates their travelling distance and hence leads to more collisions with gas atoms to create additional electrons and gas ions in a more dense plasma. Thanks to this method, a stable ion plasma can be realized at low pressures. A rough sketch of this mechanism is shown in Fig. 2.2.

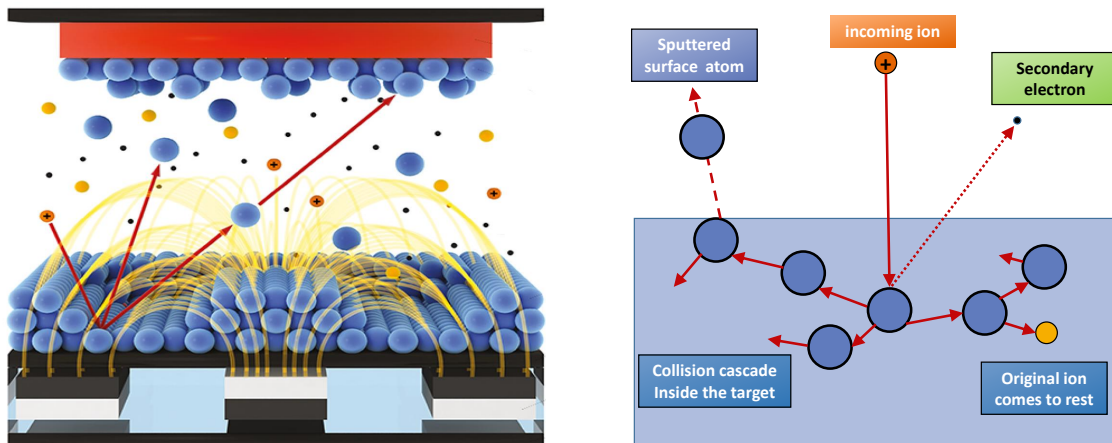


Figure 2.2: Schematic illustration of the magnetron sputtering process. The incident incoming ions cause a cascade of collisions in the target material that triggers the injection of both surface atoms and secondary electrons. The 3D-image was adapted from [37] and the schematic sketch was recreated with matching colour palette from Fig. 1. in [38].

The downside of this method is that the removal of target material is enhanced in the regions, where the horizontal magnetic field lines cause more ionization scattering processes and thus the removal of more material, as can be seen in the characteristic circular grinding spots. This effect decreases the lifetime of a magnetron target and increases the costs of maintenance.

2.1.2 Sample fabrication at the Superbowl

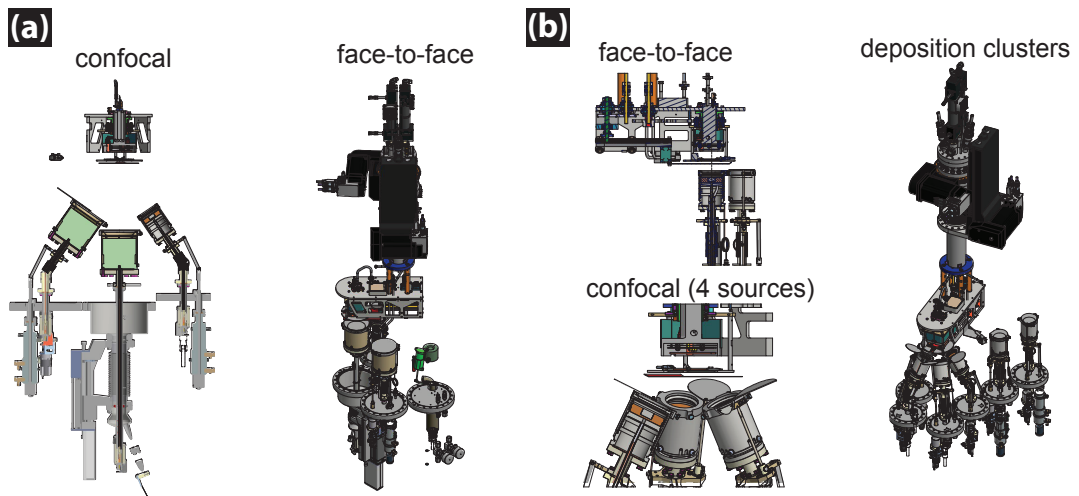


Figure 2.3: Illustration of the magnetron configuration within both chambers of the Superbowl ultra high vacuum machine. (a) illustrates the configuration in the SP2, (b) in the SP4. Adapted from [35].

Fig. 2.3 illustrates the positioning of the magnetrons in the chamber SP2 (a) and SP4 (b). The former contains 3 magnetrons, two of which are tiltable to a confocal configuration, which enables simultaneous sputtering of three targets, while the latter consists of two clusters with four tiltable sources each to sputter up to four materials at the same time. Their base pressure is $<5 \times 10^{-9}$ mbar and during deposition processes a constant Argon gas pressure in the 10^{-3} mbar-range is maintained via the automatic regulation of an adjustable butterfly valve.

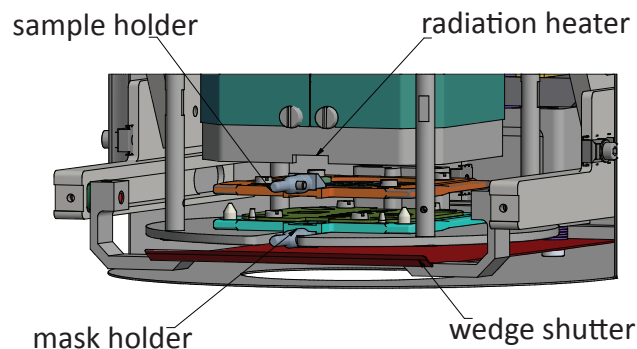


Figure 2.4: Technical drawing of the substrate manipulator used to mount the sample holder in both chambers of the Superbowl. Adapted from [35].

For sample installation, the sample is mounted on a sample holder and inserted into the load-lock [LL] connected to both deposition chambers via pneumatic valves, which is subsequently evacuated. Once it reaches a base pressure below $<1 \times 10^{-6}$ mbar, the sample can be moved to either SP2 or SP4 via a magnetic transfer rod and is placed on a three axes substrate manipulator, as schematically illustrated in Fig. 2.4, controlled by BestecTM-software to move the sample over the desired magnetron and adjust its distance d from the target during the sputtering process. To commence the process, first the wedge shutter

below the sample holder and then the target's magnetron shutter are successively opened. Additionally, the substrate is rotated with 20 rpm during deposition to ensure homogeneous growth across the sample surface. The materials deposition rate is determined in situ by a quartz microbalance, which is also mounted on the substrate manipulator. During deposition its mass increases and the change in its resonance frequency f_{res} can be measured and converted to a deposition rate for given material parameters. From these measurements, we determine the deposition time for obtaining the desired layer thickness. After the deposition time, first the magnetron shutter and following the wedge shutter are closed again and the ion plasma is extinguished. Finally, the sample holder can be transported back to the loadlock, which is subsequently vented to remove the substrate [36].

2.1.3 Optimization parameters

For optimal growth conditions, there are several growth parameters which need to be optimized:

- Deposition rate r : By changing either the target-substrate distance d or the sputtering power P of the source, the rate at which material is deposited on the sample surface can be adjusted. Depending on the desired properties, either a rapid or slow growth rate is favourable. For example, we found that rapidly grown permalloy has a lower gilbert damping α than one grown at a slower r . This is probably due to the fact that fewer defects can form in the material during the reduced growth time. Conversely, for the growth of tungsten, a slow rate is commonly preferred in experiments involving the SMR-effect for precisely this reason, as more defects lead to more extrinsic spin dependent scattering and hence a larger spin Hall angle Θ_{SH}
- Process temperature T_{sample} : A substrate heater mounted on top of the manipulator enables heating the sample to a constant temperature of up to 800°C during deposition. Target atoms sputtered on a heated substrate have a higher kinetic energy and can overcome local potential barriers to find their optimal alignment, but too much thermally induced movement can disturb the optimal layer-formation on the sample surface and lead to unwanted interdiffusion of the materials. Therefore there is a sweet spot for T_{sample} that needs to be determined.
- Deposition pressure p : As established previously, the inert gas pressure during deposition affects the mean free path l of the particles ejected from the target material surface. Heavier particle complexes have a lower l , and thus the careful adjustment of p enables the control over the size of the particles that reach the substrate. This can improve the substrates surface roughness.
- Ratio of inert and reactive gas in reactive sputtering processes x : In order to fabricate compound materials like oxides or nitrides a reactive gas has to be injected during sputtering, which forms radicals in the ion plasma. These radicals react with the sputtered target material to form the desired compound. For an optimal growth of these compound materials, the ideal ratio of inert and reactive gas is required. In the growth process of NbN for example, the superconducting transition temperature T_{C} has been found to sensitively depend on the right Ar/N₂-ratio [39, 40].

- Hysteretic inlet of the reactive sputtering gas: In reactive sputtering processes the free radicals of the reactive gas react with both the ejected target particles as well as the target itself, which can change its electrical conductance. For this reason it is not uncommon to measure a hysteretic behaviour of the target voltage as a function of N_2 -flow in the chamber [35, 40]. This affects both the deposition rate and quality of the grown thin film, so it is advisable to test whether the traversal of a hysteretic path in N_2 -flow before setting it to the optimal ratio x has beneficial effects on the thin film properties.

2.1.4 Our sample fabrication process

Our Superconductor/Ferromagnet-heterostructures were grown on cleaned Si (001) substrate with a $1\ \mu\text{m}$ thick thermally grown SiO_2 -capping layer.

We selected NbN as our superconducting layer for its resilience to magnetic fields and high superconducting transition temperature of up to $T_C = 16.8\ \text{K}$ [41–43]. These properties make NbN an ideal candidate for BBFMR at cryogenic temperatures as it offers both a large margin in T between the boiling point of liquid helium and T_C and also in applied external field $\mu_0 H_{\text{ext}}$, which directly translates to the bandwidth of applicable driving frequencies f in BBFMR, to conduct our experiments. The used growth process follows the recipe optimized in [35] and is listed in Tab. A.1. We grew NbN both on the bare substrate and several heavy metals like Pt to investigate its spin pumping properties.

After the deposition of NbN in the SP2, our substrate is transferred to the SP4 for the growth of a low-damping ferromagnetic material. Here our choice fell on the alloy $\text{Co}_{25}\text{Fe}_{75}$ for its record-low damping in metallic damping [44, 45]. The used growth recipe follows the one optimized at the Superbowl by [36]. Lastly, we deposited a thin capping layer of Ta on our $\text{Co}_{25}\text{Fe}_{75}$ to protect it from oxidization. Throughout the course of this master thesis many different materials were grown and experimented on. Their respective growth parameters are given in Tab. A.2.

2.2 X-Ray reflectometry

To check, whether our fabricated samples possess the desired layer thickness and to investigate the roughness of the thin films for further optimization, we conducted X-ray reflectometry measurements.

2.2.1 Operation principle

X-Ray reflectometry measures the intensity of high-energy photons reflected from the individual layers of the samples thin film under grazing incidence [46–48]. By assuming the classical wave-like behaviour of light, we can use Bragg’s law for constructive interference to describe the measured intensity as a function of the angle of incidence θ .

$$n \cdot \lambda = 2d \cdot \sin(\theta) \quad (2.1)$$

Here λ is the wavelength of the emitted X-rays, d is the thin film layer thickness and n represents the n -th maximum. With this naive approach, one expects to detect maxima of reflected light intensity with a periodicity in θ that is reciprocally proportional to the layer thickness d for low angles of incidence and thereby one obtains an estimate of the layer thickness.

Samples consisting of multiple layers require more sophisticated models, taking into account the Fresnel equations for the reflection and transmission of X-rays at the multiple interfaces of the sample. These models quickly become too demanding to solve analytically and require fitting with numerical simulations. For this purpose we fit our measured data with LeptosTM-fitting software utilizing a simulated annealing optimization procedure. This approach is rather time-consuming, but provides more precise results than a simple Levenberg-Maquardt algorithm [36, 49].

The samples fabricated in this thesis consist of 3 to 6 layers of different materials. In our experiments, better fitting results are achieved under the assumption that the thin Ta-cap layer consists of an oxidized and unoxidized fraction, which requires the inclusion of another layer in our sample model. We decided to forego the addition of additional parameters like surface roughness and material density to reduce the number of parameters in our fit. However, we found that the individual inclusion of surface roughness as a degree of freedom for any of the layers does not significantly affect the fitted curve.

2.2.2 Results of XRD-reflectometry

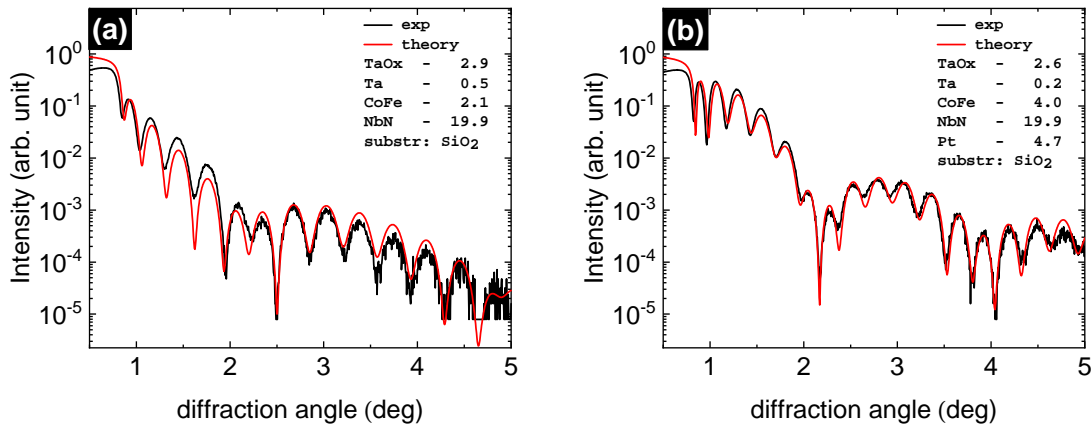


Figure 2.5: Experimental results of the XRD reflectometry measurements [black] for a NbN/Co₂₅Fe₇₅-bilayer (a) and a Pt/NbN/Co₂₅Fe₇₅-trilayer (b) together with the fitted theory curve [red] and corresponding layer thicknesses in nm. The desired stack sequences were (a): NbN (20 nm)/Co₂₅Fe₇₅ (2 nm)/Ta (2 nm) and (b): Pt (5 nm) /NbN (20 nm)/Co₂₅Fe₇₅ (4 nm)/Ta (2 nm).

Two exemplary results are illustrated in Fig. 2.5 for two NbN/Co₂₅Fe₇₅-bilayers, one without seedlayer (a) and one grown on a thin Pt layer (b). The fits match the experimental data rather nicely, particularly with regards to the periodicity of the maxima. Deviations in their height stems from a reduction of the intensity of the scattered photons on rough spots of the sample interface. The desired layer thicknesses were NbN (20 nm)/Co₂₅Fe₇₅ (2 nm)/Ta (2 nm) for (a) and Pt (5 nm) /NbN (20 nm)/Co₂₅Fe₇₅ (4 nm)/Ta (2 nm) for (b), matching

their simulated counterparts quite nicely. Its deviation for the Ta-capping layer is caused by the expansion of the Ta when oxidizing to Ta_2O_5 . We assume that our thin films grown in the Superbowl deviate from the desired layer thickness by no more than $\pm 10\%$.

In addition, 2θ - ω scans at large θ exhibited no crystalline peaks at characteristic angles in any of the NbN/ $\text{Co}_{25}\text{Fe}_{75}$ -bilayers. Only for samples grown on a thin Pt layer, we found a small and broadened peak of around 100 counts manifested at roughly $2\theta = 39.4^\circ$. It can be attributed to reflections from the (111)-plane in cubic Pt albeit slightly shifted from the literature value of 39.72° [50]. This was confirmed with the XRD scan of a thin film Pt 5nm surface, which exhibited the same characteristic when exposed to a temperature of 400°C as used for the growth process of NbN. We assume that all samples investigated within this thesis comprise thin film layers possessing merely a polycrystalline composition.

3 Theoretical concepts

In this chapter we aim to describe the properties of the two antagonising ordering phenomena ferromagnetism and superconductivity and provide the necessary theoretical background to explain the obtained experimental results of this thesis. We begin with a rather rough overview of superconductivity that spans from the definition of its most fundamental parameters like London penetration depth λ_L and coherence length ξ_0 to the very specific so-called Bogoliubov-Valatin quasiparticles [BVQP] spin susceptibility χ_s [32, 33] derived from BCS-theory [34] which is incremental for the theoretical description of quasiparticle spin transport in superconductors. Additionally, we derive properties of the BVQP like excitation energy E_k and DOS $D_s(E_k)$. This is followed up by a general introduction into the fundamentals of magnetization dynamics excited in a ferromagnetic material in an applied external magnetic field. We extend this case by adding an additional perpendicular oscillating driving field and illustrate its magnetic response by deriving the Polder susceptibility [51] and resonance condition, the famous Kittel equation [52]. Lastly, we put the former two working components together and discuss how to measure the spin transport properties of the superconducting material by investigating the spectroscopic parameters of the resonant ferromagnetic layer.

3.1 Properties of superconducting thin films

This section is dedicated to the properties of superconducting thin films. We will list only the key properties required to explain the results given in chapters 5-7. A detailed illustration of this topic in all of its facets can be found in [53, 54].

3.1.1 Basics of superconductivity

In simple terms, superconductivity stems from the attractive interaction of electrons via the virtual exchange of phonons. In this retarded interaction picture, an electron moving in a superconducting material can attract the positively charged atom cores of the underlying lattice and leads to an elastic distortion creating a positive potential mold, which attracts another electron. By viewing this pairing mechanism in momentum-space, it becomes evident that this mechanism favours the pairing of electrons of opposite momentum \mathbf{k} . These electron pairs are called Cooper-pairs [53]. Their relatively large size between 10 nm to 1000 nm depending on the relaxation time τ of the materials atoms leads to the overlapping of the wavefunctions of several Cooper-pairs and forces them onto the phase-locked state $\Psi(\mathbf{r}, t)$ of fixed amplitude $|\Psi_0(\mathbf{r}, t)|$ and phase $\theta(\mathbf{r}, t)$. As a first main property of superconductivity we can thus assume that all charge carriers in the superconductor are part of a macroscopic wavefunction of the form

$$\Psi(\mathbf{r}, t) = |\Psi_0(\mathbf{r}, t)| \cdot e^{i\theta(\mathbf{r}, t)}. \quad (3.1)$$

With the usual quantummechanical normalization conditions

$$|\Psi_0(\mathbf{r}, t)|^2 = n_s(\mathbf{r}, t) \quad (3.2)$$

$$\int |\Psi(\mathbf{r}, t)|^2 dV = N_s, \quad (3.3)$$

where $n_s(\mathbf{r}, t)$ is the local density and N_s the total number of superconducting electrons [55]. The behaviour of a superconductor in the presence of an external electric and magnetic field has been phenomenologically derived by the London brothers in 1935 [56] with a simple two-fluid-model. The perfect conductance of a superconducting charge current \mathbf{J}_s in the absence of an applied electric field \mathbf{E} is described by the first London equation

$$\frac{\partial(\Lambda \mathbf{J}_s)}{\partial t} = \mathbf{E}. \quad (3.4)$$

Here $\Lambda = \frac{m_s}{\mu_0 n_s q_s^2}$, with m_s as the mass and q_s the charge of the Cooper-pairs, is the so called London coefficient. Simply speaking, in the absence of an external \mathbf{E} , the charge current does not change with time, which corresponds to perfect conductance. Conversely, the response of a superconductor to an applied external magnetic field is given by the second London equation

$$\nabla \times (\Lambda \mathbf{J}_s) = -\mathbf{B}. \quad (3.5)$$

By multiplying both sides of the second London equation by $[\nabla \times]$ and using the appropriate Maxwell equation and vector identities, one receives

$$\nabla^2 \mathbf{B} = \frac{\mu_0}{\Lambda} \mathbf{B}. \quad (3.6)$$

This formula relates an external \mathbf{B} -field to screening currents flowing inside the superconducting layer, which completely shield its interior. Hence the magnetic response of a superconductor is perfectly diamagnetic. This effect was first observed by Walther Meißner in 1933 [57]. The physically sound solution of Eq. (3.6) is an exponentially decaying function

$$\mathbf{B}(\mathbf{r}) = \mathbf{B}_0 e^{-\frac{r}{\lambda_L}} \quad (3.7)$$

with the decaying constant

$$\lambda_L = \sqrt{\frac{\mu_0}{\Lambda}} = \sqrt{\frac{m_s}{\mu_0 n_s q_s^2}} \quad (3.8)$$

called the London penetration depth. It is a measure of how deep the magnetic field can penetrate into the superconductor and usually takes values in the 10 nm- to 100 nm range. For the thin-film superconductors in our samples with thickness d_{SC} smaller than λ_L the perfect screening no longer is possible and \mathbf{B} -fields can effectively penetrate the sample. For these cases, the greatly enhanced 2-dimensional London penetration depth λ_{eff} needs to be used [58].

$$\lambda_{eff} = \frac{\lambda_L^2}{d_{SC}} \quad (3.9)$$

However not all superconducting materials exhibit the Meißner effect. Above a certain critical field value $\mu_0 H_{c1}$, some form normal conducting canals to let flux penetrate into the material, with each of them carrying one discrete flux quantum Φ_0 . In these so-called Type-II-superconductors it is more favourable to lose Cooper-pair condensation energy E_C by forming vortices and conversely save field expulsion energy E_B by letting the \mathbf{B} -

field penetrate. The created vortices arrange in a regular triangular lattice, the so-called Abrikosov-lattice [59] as illustrated in Fig. 3.1.

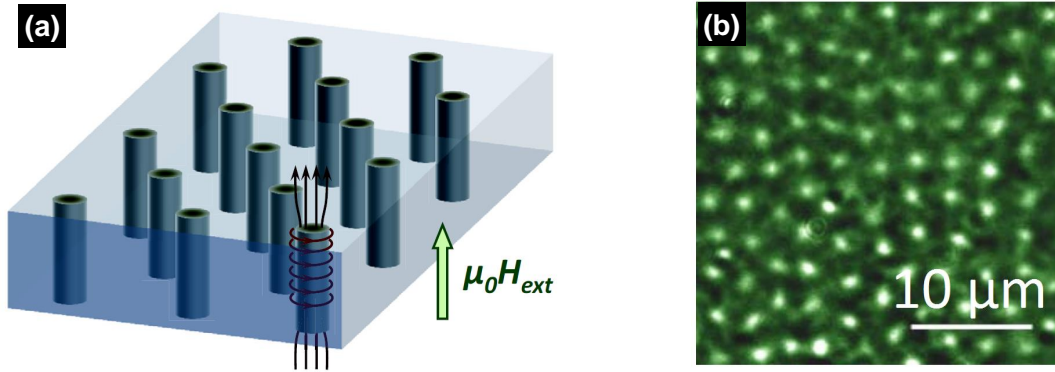


Figure 3.1: (a): Schematic illustration of the vortex lattice in a type II- superconductor. For one vortex, the flux lines and imaging currents are sketched. Taken from [53]. (b): Vortex configuration of a NbSe₂-crystal at 4K in the earth's magnetic field mapped with magneto-optical imaging. Adapted from [60].

The radius of these vortices is given by the Ginzburg-Landau coherence length ξ_{GL} which is the recovery length of the superconductor's order parameter $|\Psi_0(\mathbf{r}, t)|^2$, when exposed to an external perturbation and was first derived by Ginzburg and Landau in 1950 [61]. It is related to the coherence length ξ_0 of a superconductor as defined by Pippard as the measure of non-locality of its response to a perturbation [62]. As E_B scales with λ_L , while the loss in condensation energy is linearly proportional to ξ_{GL} , the type of superconductivity in a material depends on their ratio, the Ginzburg-Landau parameter

$$\kappa = \frac{\lambda_L}{\xi_{GL}}. \quad (3.10)$$

For $\kappa < 1/\sqrt{2}$, the thin film will behave like a type-I-superconductor, while for $\kappa \geq 1/\sqrt{2}$, it will exhibit Type-II-superconductivity

For the used thin film NbN, literature values for λ_L range from 200 nm to 400 nm [42, 43], whereas the coherence length ξ_0 is estimated to be ~ 5 nm [63, 64]. As the theoretical ξ_{GL} usually only deviates slightly from ξ_0 , we expect our thin films to exhibit type-II-superconductivity and the presence of vortices in measurements in out-of-plane geometry, where the external magnetic field \mathbf{H}_{ext} is perpendicular to the sample plane.

3.1.2 Definition of the Bogoliubov-Valatin quasiparticle spin susceptibility χ_s

In this chapter, we aim to explain how thermally excited quasiparticles accumulated in a superconductor respond to an external perturbation $\delta\zeta_{\mathbf{k},\sigma}^{ext}$ with the accumulation of a spin polarization and thereby a magnetization M , by using the Bogoliubov-Valatin-formalism [32, 33] and define the quasiparticle spin susceptibility χ_s which is the key quantity to describe quasiparticle spin transport in superconductors. The presented formalism is kept very brief and follows the detailed derivations provided by Dr. Dietrich Einzel found

in [65–67]. We begin with the Bogoliubov-Valatin diagonalized BCS-Hamiltonian

$$\hat{H}_{\text{BCS}} - \mu \hat{N} = \underbrace{U_{\text{BCS}}(0)}_{T=0} + \underbrace{\sum_{\mathbf{k}} E_{\mathbf{k}} \left[\hat{\alpha}_{\mathbf{k},\uparrow}^\dagger \hat{\alpha}_{\mathbf{k},\uparrow} + \hat{\alpha}_{-\mathbf{k},\downarrow}^\dagger \hat{\alpha}_{-\mathbf{k},\downarrow} \right]}_{T>0}. \quad (3.11)$$

Here μ is the electron chemical potential and \hat{N} is the total fermion operator. The operators $\hat{\alpha}_{\mathbf{k},\uparrow}^\dagger$ and $\hat{\alpha}_{\mathbf{k},\uparrow}$ create and annihilate a fermionic thermal excitation in a quantum state with momentum \mathbf{k} and spin σ $|\mathbf{k}, \sigma\rangle$, the so-called Bogoliubov-Valatin quasiparticles [BVQP]. Lastly $U_{\text{BCS}}(0)$ is the energy of the thermal BCS ground state for $T \rightarrow 0$. The energy spectrum of the BVQP is given by

$$E_{\mathbf{k}} = \sqrt{\xi_{\mathbf{k}}^2 + \Delta^2}, \quad (3.12)$$

where $\xi_{\mathbf{k}}$ denotes the energetic distance of the energy level $\epsilon_{\mathbf{k}}$ from the the chemical potential μ , while Δ represents the superconducting gap energy defined as the energy gap in the excitation spectrum of quasiparticles for $\xi_{\mathbf{k}} = 0$. The BVQP are linear combinations of electron- and hole excitations of opposite spins. As shown in Fig. 3.2(a), their nature continuously evolves from holelike to electronlike with increasing $\xi_{\mathbf{k}}$. The dashed lines display the dispersion relation of normal conducting electrons and holes. It becomes apparent that the quasiparticles are purely holelike for $\xi_{\mathbf{k}} \ll 0$ and pure electrons for $\xi_{\mathbf{k}} \gg 0$. For $\xi_{\mathbf{k}} = 0$, they are the equal superposition of an electron with wavevector \mathbf{k} and a hole with $-\mathbf{k}$ [53].

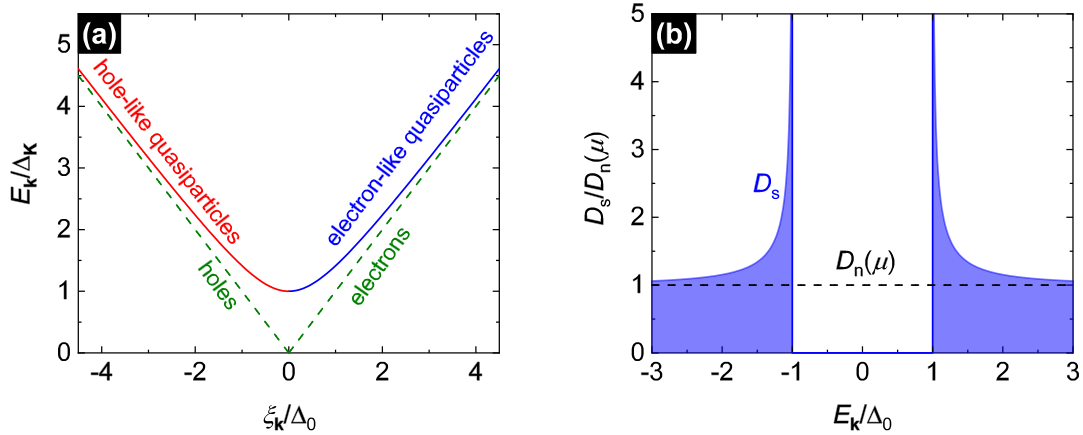


Figure 3.2: (a): Excitation energy $E_{\mathbf{k}}$ of the BVQP [red and blue line], normalized to the gap parameter at $T = 0$ K, Δ_0 , in vicinity of E_F together with the dispersion relation of normal conducting electrons and holes. The dashed green lines indicate the dispersion relations of normal electrons and holes. Recreated from Fig. 13.40 in [53]. (b): quasiparticle density of states as a function of the excitation energy $E_{\mathbf{k}}$ at $T = 0$ K. As a reference, the normalized density of states for the normalconducting state is shown as a dashed black line.

By deriving Eq. (3.12), the quasiparticle density of states $D_s(E_{\mathbf{k}})$ can be written as a function of $E_{\mathbf{k}}$ in the form:

$$D_s(E_{\mathbf{k}}) = D_n(\xi_{\mathbf{k}}) \frac{d\xi_{\mathbf{k}}}{dE_{\mathbf{k}}} = \begin{cases} D_n(\mu) \cdot \frac{|E_{\mathbf{k}}|}{\sqrt{E_{\mathbf{k}}^2 - \Delta^2}}, & \text{if } |E_{\mathbf{k}}| \geq \Delta \\ 0, & \text{otherwise} \end{cases} \quad (3.13)$$

Fig. 3.2(b) illustrates $D_s(E_k)$ together with the density of states of a metal in the normal conducting phase D_n . It becomes apparent that $D_s(E_k)$ diverges at $E_k = \Delta$ and transitions into D_n for $|E_k| \gg \Delta$, as the highly energetic quasiparticles are hardly affected by the superconducting pairing mechanism and effectively convert into normal electrons. The quantum statistics of the BVQP particles is given by the Fermi-Dirac distribution

$$\nu(E_k) = \langle \hat{a}_{\mathbf{k},\uparrow}^\dagger \hat{a}_{\mathbf{k},\uparrow} \rangle = \frac{1}{\exp\left(\frac{E_k}{k_B T}\right) + 1}. \quad (3.14)$$

Its derivative with respect to E_k

$$y_k = -\frac{\partial \nu(E_k)}{\partial E_k} = \frac{1}{4k_B T} \frac{1}{\cosh^2\left(\frac{E_k}{2k_B T}\right)}, \quad (3.15)$$

generates the Yosida function $Y(T)$

$$Y(T) = \langle y_{\mathbf{k}}^{(0)} \rangle$$

$$y_{\mathbf{k}}^{(n)} = \int_{-\infty}^{\infty} d\xi_{\mathbf{k}} \frac{N(\xi_{\mathbf{k}})}{N(0)} \left| \frac{\xi_{\mathbf{k}}}{E_{\mathbf{k}}} \right|^n y_{\mathbf{k}}. \quad (3.16)$$

It describes the temperature dependence of the normalconducting phase n_n as a function of temperature

$$n_n(T) = n_{\text{tot}} Y(T), \quad (3.17)$$

with n_{tot} as the total particle number. Intuitively, in a two-fluid approach, the condensate density of the superconducting phase n_s is given by

$$n_s(T) = n_{\text{tot}} \cdot (1 - Y(T)). \quad (3.18)$$

The temperature-dependent evolution of n_s is shown in Fig. 3.3 together with that of the gap-parameter Δ based on the numerical calculations of Dr. Dietrich Einzel outlined in [65]. The used Mathematica script can be found in Chapter B.1.

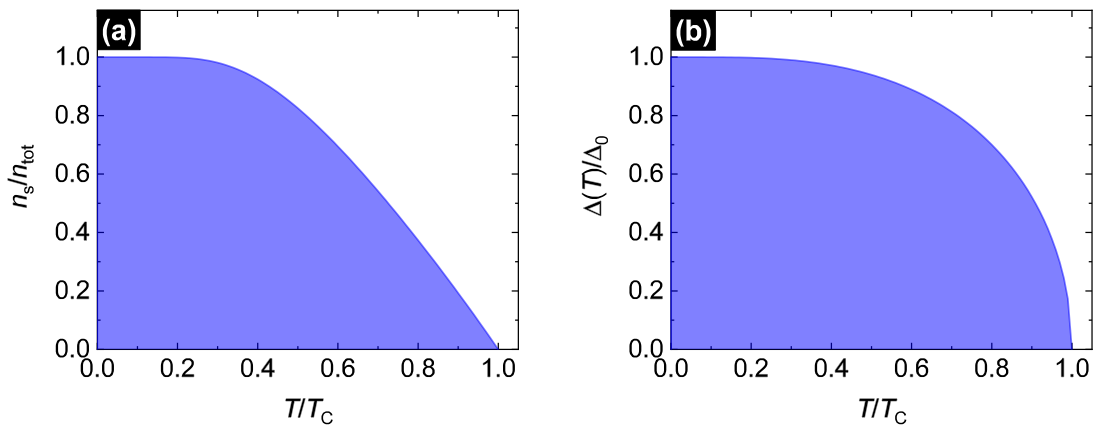


Figure 3.3: Normalized superconducting condensate density n_s/n (a) and energy gap Δ/Δ_0 (b) as a function of reduced temperature T/T_C .

In the following, we explore the local response of the BVQP to external perturbation in the gauge-invariant form

$$\delta\xi_{\mathbf{k},\sigma}^{\text{ext}} = \hbar\mathbf{k} \cdot (\mathbf{v}^{\text{s}} - \mathbf{v}^{\text{n}}) - \mu_{\text{B}}\sigma B_0 = -\delta\xi_{-\mathbf{k},-\sigma}^{\text{ext}}. \quad (3.19)$$

where Here \mathbf{v}^{s} and \mathbf{v}^{n} respectively denote the drift velocity of the superconducting and normal conducting phase, $\mu_{\text{B}} = 9.274 \times 10^{-24}$ J/T is Bohr's magnetron and B_0 denotes an external magnetic field. We forego further derivations and jump straight to the results. The linear response in local particle distribution density $\delta n_{\mathbf{k},\sigma}^{\text{loc}}$ can be expressed as

$$\delta n_{\mathbf{k},\sigma}^{\text{loc}} = n_{\mathbf{k}}(\delta\xi_{\mathbf{k},\sigma}^{\text{ext}}) - n_{\mathbf{k}} = -y_{\mathbf{k}}\delta\xi_{\mathbf{k},\sigma}^{\text{ext}}. \quad (3.20)$$

The net magnetic response M created by this shift in $n_{\mathbf{k}}$ is

$$M = \frac{\mu_{\text{B}}}{V} \sum_{\mathbf{k},\sigma} \delta n_{\mathbf{k},\sigma}^{\text{loc}} = \chi_{\text{s}} B_0. \quad (3.21)$$

The classical relation $M = \chi B$ gives us the BVQP spin susceptibility χ_{s} of the superconductor

$$\chi_{\text{s}} = \frac{\mu_{\text{B}}^2}{V} \sum_{\mathbf{k},\sigma} y_{\mathbf{k}} = \chi_{\text{N}} \langle y_{\mathbf{k}} \rangle = \chi_{\text{N}} Y(T), \quad (3.22)$$

where

$$\chi_{\text{N}} = n_{\text{F}} \mu_{\text{B}}^2 \quad (3.23)$$

is the susceptibility of the normal conducting phase and n_{F} stands for its particle density at the Fermi surface. Notably, just like the normal conducting fluid density n_{n} , χ_{s} is related to the Yosida function [68].

3.2 Key aspects of ferromagnetic resonance

The other macroscopic ordering phenomenon presented in this thesis is that of magnetic ordering in our $\text{Co}_{25}\text{Fe}_{75}$ -layer. The magnetic moments of a ferromagnetic material align in parallel to oneanother below a critical temperature, the so-called Curie-Temperature which we will denote with a small letter T_{c} to avoid confusion with the superconducting transition temperature T_{C} . For $\text{Co}_x\text{Fe}_{1-x}$, T_{c} exceeds 1000 K [69], permitting room temperature pre-characterization measurements . While superconductivity is mediated by phonons creating a polarized distortion in a lattice, ferromagnetic alignment is established by the Heisenberg interaction [70] via the overlapping of electron wave functions of two neighbouring atoms favouring a parallel spin alignment or indirectly mediated by intermediate atoms or electrons. In the following, we will outline the fundamental equations of ferromagnetic resonance and define its spectroscopic parameters.

3.2.1 Magnetization dynamics

The magnetization dynamics in a ferromagnet are most easily described by viewing it as one net magnetic moment devoid of domains or pinned atoms. In this macrospin approach,

the length of the magnetization vector \mathbf{M} comprises the sum of all magnetic moments \mathbf{m}_i in the materials volume V

$$\mathbf{M} = \frac{1}{V} \sum_{\mathbf{m}_i \in V} \mathbf{m}_i. \quad (3.24)$$

The application of an external magnetic field \mathbf{H}_{ext} will lead to a reorientation of this magnetization vector, as the magnetic moment \mathbf{m} is related to angular momentum \mathbf{L} via the gyromagnetic ratio γ

$$\mathbf{m} = \gamma \mathbf{L}. \quad (3.25)$$

This is equal to the exertion of a torque $\boldsymbol{\tau}$ on the magnetization \mathbf{M} in the form

$$\boldsymbol{\tau} = -\mathbf{M} \times \mu_0 \mathbf{H}_{\text{eff}}. \quad (3.26)$$

where we consider that in the Macrospin model, anisotropy and demagnetization fields \mathbf{H}_{ani} and \mathbf{H}_{de} also take non-negligible macroscopic values and hence the magnetization vector \mathbf{M} aligns to a net effective magnetic field \mathbf{H}_{eff}

$$\mathbf{H}_{\text{eff}} = \mathbf{H}_{\text{ext}} + \mathbf{H}_{\text{ani}} - \mathbf{H}_{\text{de}}. \quad (3.27)$$

The dynamic equation of motion of \mathbf{M} can be derived by plugging Eq.(3.25) in Eq. (3.26)

$$\frac{d\mathbf{M}}{dt} = -\gamma \mathbf{M} \times \mu_0 \mathbf{H}_{\text{eff}}, \quad (3.28)$$

describing a circular motion of \mathbf{M} with precession frequency

$$\omega_L = \gamma \mu_0 |\mathbf{H}_{\text{eff}}| \quad (3.29)$$

For the sake of a more realistic model, Gilbert introduced a phenomenological term to Eq. (3.28) in 2004 [71] to account for damping in the Landau-Lifshitz-Gilbert [LLG]-equation

$$\frac{d\mathbf{M}}{dt} = -\gamma \mathbf{M} \times \mu_0 \mathbf{H}_{\text{eff}} + \frac{\alpha}{M_s} \mathbf{M} \times \frac{d\mathbf{M}}{dt}. \quad (3.30)$$

Here α is defined as the Gilbert damping parameter, as the vector $\mathbf{M} \times \frac{d\mathbf{M}}{dt}$ is directed towards the rotation center, effectively reducing the precession amplitude as a function of time. The resulting trajectory for \mathbf{M} is a spiral motion around \mathbf{H}_{eff} .

3.2.2 Ferromagnetic resonance

We extend our model by the addition of an oscillating driving field $\mathbf{h}_{\text{rf}}(t)$ perpendicular to the external static field \mathbf{H}_{ext} as illustrated in Fig. 3.4, which exerts an additional torque $\mathbf{M} \times \mathbf{h}_{\text{rf}}$ on \mathbf{M} that counteracts the damping. This system can be viewed as a driven, damped harmonic oscillator suggesting the existence of a resonant enhancement of amplitude when the driving frequency of \mathbf{h}_{rf} matches the precession frequency ω of \mathbf{M} . This is due to the fact that the displacement of \mathbf{M} caused by \mathbf{h}_{rf} does not average out as a function of time when matching ω . The following derivations will closely follow the compact overviews provided by [36,72] based on extensive derivations found in [73–75].

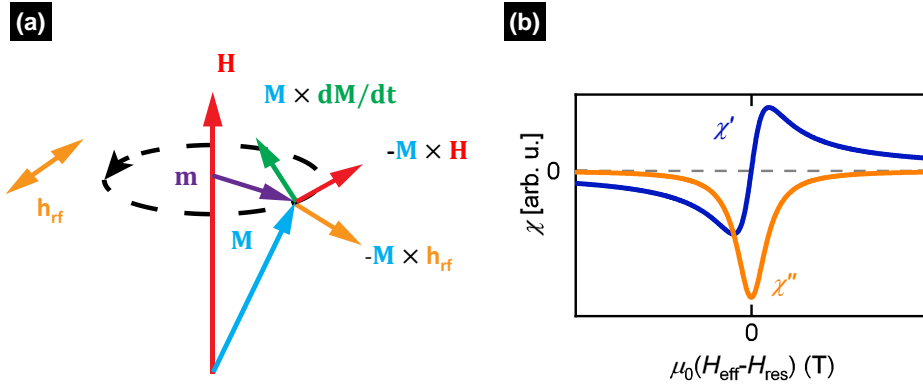


Figure 3.4: Precessional motion of \mathbf{M} in an effective field \mathbf{H} (a) as described by the LLG-equation. The magnetic field \mathbf{H} creates a torque $-\gamma\mathbf{M} \times \mu_0\mathbf{H}_{\text{eff}}$ [red], driving \mathbf{M} along a circular path, reduced in amplitude by the damping term $\mathbf{M} \times \frac{d\mathbf{M}}{dt}$ [green]. In FMR experiments the applied perpendicular oscillatory driving field \mathbf{h}_{rf} exerts an additional torque [orange] counteracting the damping. Upon hitting the resonance frequency of the system, its contribution does not average out and the system absorbs energy from \mathbf{h}_{rf} . The magnetic response χ of the system is illustrated in dispersive real part χ' and dissipative imaginary part χ'' as a function of \mathbf{H}_{eff} in (b). It relates the perpendicular magnetization \mathbf{m} to the oscillatory driving field \mathbf{h}_{rf} by the equation $\mathbf{m} = \chi\mathbf{h}_{\text{rf}}$. Adapted from [72].

We model this problem by describing the response of a finite sample with magnetization \mathbf{M} exposed to a constant external magnetic field applied along the z-axis $\mathbf{H} = H_{\text{ext}}\hat{\mathbf{e}}_z$ and driven by an oscillatory field \mathbf{h}_{rf} in the x-y-plane, triggering a dynamic response $\mathbf{m}(t)$ in the ferromagnet. Furthermore we neglect the anisotropy field \mathbf{H}_{ani} for the sake of simplicity. Under these circumstances, we can split the magnetic field \mathbf{H}_{eff} and magnetization \mathbf{M} into a time-independent and a time-dependent part:

$$\begin{aligned}\mathbf{H}_{\text{eff}} &= \mathbf{H}_{\text{ext}} - \mathbf{H}_{\text{de}} + \mathbf{h}_{\text{rf}}(t) \\ &= (H_{\text{ext}} - N_z M_0)\hat{\mathbf{e}}_z - N_x m_x(t)\hat{\mathbf{e}}_x - N_y m_y(t)\hat{\mathbf{e}}_y + \mathbf{h}_{\text{rf}}(t) \\ \mathbf{M} &= \mathbf{M}_0 + \mathbf{m}(t) = M_0\hat{\mathbf{e}}_z + \mathbf{m}(t)\end{aligned}\quad (3.31)$$

A linear approach of the form

$$\begin{aligned}\mathbf{h}_{\text{rf}}(t) &= (h_{\text{rf},x}\hat{\mathbf{e}}_x + h_{\text{rf},y}\hat{\mathbf{e}}_y) \cdot e^{i\omega t} \\ \mathbf{m}(t) &= (m_x\hat{\mathbf{e}}_x + m_y\hat{\mathbf{e}}_y) \cdot e^{i\omega t},\end{aligned}\quad (3.32)$$

is used for the time-dependent contributions under the premise, that $m_{x/y} \ll M_0$.

This Ansatz is plugged into the LLG-equation (3.30), where we assume, that the static part of the magnetization \mathbf{M}_0 is parallel to the external field and hence $\mathbf{M}_0 \times \mathbf{H}_{\text{ext}} = 0$. The resulting expression

$$\begin{pmatrix} h_{\text{rf},x} \\ h_{\text{rf},y} \end{pmatrix} = \hat{\chi}_{\text{P}}^{-1} \begin{pmatrix} m_x \\ m_y \end{pmatrix}\quad (3.33)$$

provides the Polder susceptibility first derived in 1949 [51] by D. Polder.

$$\begin{aligned}\hat{\chi}_P &= \frac{\mu_0 M_s}{\text{Det}(\hat{A})} \hat{A} \\ \hat{A} &= \begin{pmatrix} A_{11} & \frac{i\omega}{\gamma\mu_0} \\ -\frac{i\omega}{\gamma\mu_0} & A_{22} \end{pmatrix} \\ A_{11} &= H_{\text{ext}} + M_s \cdot (N_y - N_z) + \frac{i\omega\alpha}{\gamma\mu_0} \\ A_{22} &= H_{\text{ext}} + M_s \cdot (N_x - N_z) + \frac{i\omega\alpha}{\gamma\mu_0}\end{aligned}\quad (3.34)$$

It consists of a dispersive real part χ' and a dissipative imaginary part χ'' . Its characteristic behaviour as a function of external magnetic field \mathbf{H}_{ext} is illustrated in Fig. 3.4(b).

With the help of this, we can determine the resonance frequency $f = \omega/2\pi$ as a function of \mathbf{H}_{ext} by solving $\text{Det}(\hat{A}) \stackrel{!}{=} 0$ and taking the real part. This gives the famous Kittel equation

$$f = \frac{\gamma\mu_0}{2\pi} \sqrt{[H_{\text{ext}} + (N_x - N_z) \cdot M_s][H_{\text{ext}} + (N_y - N_z) \cdot M_s]}, \quad (3.35)$$

first derived by its namesake in 1948 [52]. It provides the resonance condition for bulk samples with different demagnetization coefficients N_i depending on the sample geometry. In our case, thin film ferromagnetic samples with ($d \simeq \text{nm}$) allow us to neglect N_i depending on the measurement geometry. We distinguish between

- In the **in-plane-geometry** [ip], the external field \mathbf{H}_{ext} is applied in the sample plane e.g. along the x-axis with $N_x = 1$ and $N_y = N_z = 0$. The in-plane Kittel equation can be expressed as

$$f = \frac{\gamma\mu_0}{2\pi} \sqrt{H_{\text{ext}}(H_{\text{ext}} + M_s)}, \quad (3.36)$$

To account for a further out-of-plane anisotropy field H_k often found in polycrystalline thin films, we replace M_s with an effective magnetization $M_{\text{eff}} = M_s - H_k$ in Eq. (3.36). In our experiments, we sweep the applied field H_{ext} at constant frequency f through the resonant field H_{res} . The required H_{res} for a given f is derived by solving Eq. (3.36) by H_{ext}

$$\mu_0 H_{\text{res}} = -\frac{\mu_0 M_{\text{eff}}}{2} + \sqrt{\left(\frac{\mu_0 M_{\text{eff}}}{2}\right)^2 + \left(\frac{2\pi f}{\gamma}\right)^2}, \quad (3.37)$$

- For the **out-of-plane-geometry** [oop], \mathbf{H}_{ext} is parallel to the surface normal and hence the corresponding demagnetization factors are $N_z = 1$ and $N_x = N_y = 0$. In oop-geometry, the Kittel equation takes the following form:

$$f = \frac{\gamma\mu_0}{2\pi} (H_{\text{ext}} - M_{\text{eff}}) \quad (3.38)$$

Hence the resonance field is:

$$\mu_0 H_{\text{res}} = \mu_0 M_{\text{eff}} + \frac{2\pi f}{\gamma} \quad (3.39)$$

Apart from the resonance field H_{res} at a given frequency f , the Polder susceptibility also provides insight into the damping of the ferromagnetic precession in its imaginary part. By using Eq. (3.34) and solving $\text{Det}(\hat{\chi}_{\text{P}}) \stackrel{!}{=} 0$ for its imaginary part, we obtain a formula describing the fanning out of the Lorentzian resonance peak as a function of driving frequency

$$\Delta H_{\text{HWHM}} = \frac{\omega\alpha}{\gamma\mu_0}, \quad (3.40)$$

where ΔH_{HWHM} is its half width at half maximum [HWHM], whereas α represents the phenomenological damping parameter that comprises all possible damping processes linear in f . In our experimental procedure, two adjustments to this equation must be made. First, the used fitting program provided by [76] utilizes the full width at half maximum [FWHM] for ΔH and thus, we need to multiply Eq. (3.40) by a factor of two. Second, in real experiments it is common for ΔH_{HWHM} not to intersect the origin but being shifted by an offset called the inhomogeneous line broadening H_{inh} . There are a multitude of potential sources for the manifestation of H_{inh} ranging from measurement setup misalignment over inhomogeneities in the sample to two-magnon scattering processes [77]. In rough terms it is a measure for sample quality when compared to literature results for the used ferromagnetic material or samples with identical stack sequence. Finally, we can express the used fitting function as

$$\mu_0\Delta H = \mu_0 H_{\text{inh}} + 2 \cdot \frac{2\pi f\alpha}{\gamma}. \quad (3.41)$$

3.2.3 Spin pumping

The formalism outlined so far displays how we can extract the spectroscopic parameters of our ferromagnetic $\text{Co}_{25}\text{Fe}_{75}$ -samples by fitting $\mu_0 H_{\text{res}}$ and $\mu_0 \Delta H$ as a function of f . Among them, the phenomenological Gilbert damping parameter α is of particular interest as the injection of angular momentum from the precessing magnetization \mathbf{M} of a FM layer into an adjacent normal metal in the form of a dynamic spin current \mathbf{j}_{s} creates an additional dissipation channel for the oscillatory motion of \mathbf{M} called spin pumping and thereby gives rise to an increase in α . According to [27], the created spin current injected across the interface is

$$\mathbf{j}_{\text{s}} = \frac{\hbar}{4\pi} \left(\text{Re}(G_{\uparrow\downarrow})\mathbf{m} \times \frac{d\mathbf{m}}{dt} - \text{Im}(G_{\uparrow\downarrow})\frac{d\mathbf{m}}{dt} \right), \quad (3.42)$$

where $G_{\uparrow\downarrow}$ is the spin-mixing conductance which describes the transport of spins non-collinear to the magnetization of the ferromagnetic layer [78]. Upon examining the symmetry of the two components of formula (3.42) it is apparent that only its real part is damping-like, whereas its imaginary part does not affect α . We obtain the contribution of spin pumping α_{SP} by inserting the former as an additional term in the LLG-equation (3.30). The resulting net alpha is [79]:

$$\alpha = \alpha_0 + \frac{\alpha_{\text{SP}}}{d_{\text{FM}}} \quad (3.43)$$

α_0 represents the intrinsic Gilbert-damping and d_{FM} is the layer thickness of the FM. Due to its reciprocal proportionality to α , very thin FM samples with low d_{FM} are required to sensitively detect changes in the spin transport properties of our FM/SC-samples below

T_C through shifts in α . It must be noted that there are several additional contributions to α in FM/NM-bilayers such as damping induced by eddy currents α_{eddy} in the NM layer scaling with d_{FM}^2 or radiative damping $\alpha_{\text{rad}} \propto d_{\text{FM}}$ originating from the dynamic flux of the precessing \mathbf{M} [80]. To reliably disentangle their respective magnitudes, α needs to be plotted as a function of d_{FM} in a layer-thickness samples series as performed in [36] for $\text{Co}_{25}\text{Fe}_{75}$. Moreover, in recent experiments it has been found that an additional relaxation pathway for α is the loss of spin polarization at the FM/NM-interface called spin memory loss [SML] [81, 82]. This phenomenon was established to explain an increase in α in FM/NM-samples with normal metals of a thickness lower than its spin diffusion length, where spin currents aren't absorbed and consequently spin pumping should only play a minor role. In order to go one step further and correctly scale the contributions of SML and spin pumping to α out of extracted α_{SP} , the magnitude of the dampinglike inverse spin Hall effect created by \mathbf{j}_s has to be quantified with the method in [29, 81].

3.3 Spin pumping into superconductors

We have now established the basic characteristics of thermally excited quasiparticles in the superconducting layer and the resonant magnetization dynamics taking place in an adjacent ferromagnetic layer. In this section we aim to put these two working components together and outline how to investigate spin currents injected from the FM via spin pumping into the SC. We can characterize the spin current transported by superconducting quasiparticles by examining the spin pumping contribution α_{SP} to the Gilbert damping of the FM as a function of temperature. We provide only a rough outline of the detailed theoretical calculations of Inoue *et al.* given in [19].

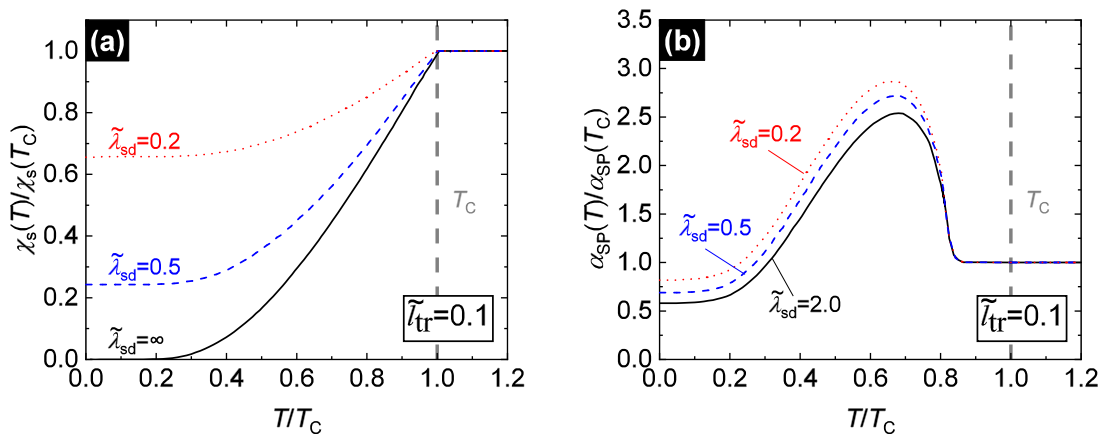


Figure 3.5: (a): Spin susceptibility χ_s of a superconductor as a function of reduced temperature for varying magnitudes of normalized spin diffusion length $\tilde{\lambda}_{sd}$ and a fixed value of normalized mean free path $\tilde{l}_{tr} = 0.1$. (b): Spin pumping contribution to Gilbert-damping α_{SP} as a function of reduced temperatures for varying values of $\tilde{\lambda}_{sd}$ and constant $\tilde{l}_{tr} = 0.1$. Adapted from [19].

We consider a FM/SC-bilayer in an external ip-magnetic field \mathbf{H}_{ext} driven in an external microwave field \mathbf{h}_{rf} with angular frequency ω_{rf} , which resonantly excites magnetization dynamics inside the ferromagnet. As established in the previous section, the injection of

spins at the interface opens up an additional dissipation channel α_{SP} to the net damping α of the macrospin precession in the FM layer. In many-body theory this precession is viewed as the damping of a collective excitation [83] i.e. the magnon mode, which can be related to its self energy $\Xi(\omega)$. In the present case, the injection of angular momentum at the SC/FM-interface from a collective magnon mode to the superconducting quasiparticle fluid is mediated by the s-d-coupling J_{sd} . It can be written as

$$\Xi(\omega) = -\frac{\mu_0 \langle J_{\text{sd}}^2 \rangle}{\sqrt{3} \hbar^2} \sum_{\mathbf{k}} \chi_s^{\mathbf{k}}(\omega), \quad (3.44)$$

where $\chi_s^{\mathbf{k}}(\omega)$ is the dynamic spin susceptibility, which is extrapolated from the static BVQP spin susceptibility χ_s^0 , defined in section 3.1.2, via analytic continuation [$\chi_s^{\mathbf{k}}(\omega) \propto \chi_s^0$]. Upon applying the relation $\alpha_{\text{SP}} \omega_{\text{ac}} = -d_{\text{FM}} \Xi(\omega_{\text{ac}})$ for the spin pumping contribution to Gilbert damping α_{SP} , we arrive at the final result:

$$\frac{\alpha_{\text{SP}}}{d_{\text{FM}}} = \frac{\mu_0 \langle J_{\text{sd}}^2 \rangle}{\sqrt{3} \hbar^2} \sum_{\mathbf{k}} \frac{1}{\omega_{\text{ac}}} \text{Im} \chi_s^{\mathbf{k}}(\omega_{\text{ac}}) \quad (3.45)$$

Here, our extended theoretical overview comes full circle directly relating the Gilbert damping α , a property of our FM layer to the BVQP-spin-susceptibility of the quasiparticle phase in the adjacent superconductor. The remaining task for Inoue *et al.* in [19] was to solve this expression in the presence of impurity spin orbit scattering. The results of their calculations are illustrated in Fig. 3.5 for both the static χ_s^0 (a) and α_{SP} (b) for varying values of spin diffusion length $\tilde{\lambda}_{\text{sd}}$ and mean free path \tilde{l}_{tr} normalized to the BCS-coherence length ξ_{BCS} . Notably for pronounced spin-orbit scattering i.e. low values of $\tilde{\lambda}_{\text{sd}}$, χ_s does not vanish even at $T = 0$ K meaning BVQP can still manifest and contribute to spin pumping. This explains the non-zero values in Fig. 3.5(b) of α_{SP} for these $\tilde{\lambda}_{\text{sd}}$. Furthermore, for $T \rightarrow 0.8 T_C$, a clear coherence peak manifests, rising in peak value with increasing impurity spin-orbit scattering. While the precise reason for its origin is up to debate, one can hand-wavily argue that the divergent quasiparticle density of states $D_s(E_{\mathbf{k}})$ at superconducting gap values $\Delta(T)$ diminishing with increasing temperature give rise to a large magnitude of quasiparticles to transport angular momentum for temperatures slightly below T_C .

Overall, the temperature-dependent behaviour of $\alpha_{\text{SP}}(T)$ provides a characteristic signature which permits to relate potential changes in the Gilbert damping α in our BBFMR-measurements to the altered quasiparticle spin transport properties in superconductors. The detection of the predicted coherence peak in α for temperatures $T \simeq (0.7 - 0.8)T_C$ is one of the central goals of this thesis.

4 Experimental procedure

Within this chapter, we will illustrate in detail how we investigated the properties of the fabricated SC/FM-heterostructures by conducting broadband ferromagnetic resonance at cryogenic temperatures. In this thesis we employed vector network analyzer ferromagnetic resonance [BBFMR] with a coplanar waveguide as it permits measurements in a broad range of frequencies required to reliably fit H_{res} and ΔH as a function of f . Additionally the VNA's ability to measure both the amplitude and phase of the signal enables us to obtain information on field- and damping-like spin-orbit torques [SOT] by employing the data processing method from [29]. The general working principle of VNA-FMR is outlined in section 4.1 closely following the detailed descriptions in [72]. Afterwards, we explain the data processing routine applied on the raw data in section 4.2 to extract H_{res} and ΔH out of the complex transmission parameter S_{21} . We end the chapter by describing the experimental setup for BBFMR at cryogenic temperatures in the Chaos-cryostat and illustrate its working principle in section 4.3.

4.1 Experimental technique

The general experimental setup for VNA-FMR consists of three components: The source of external magnetic field being either an electromagnet or a superconducting 3D-vector magnet for cryogenic temperatures, the VNA itself and a coplanar waveguide [CPW]. A schematic illustration of the experimental setup is shown in Fig. 4.1.

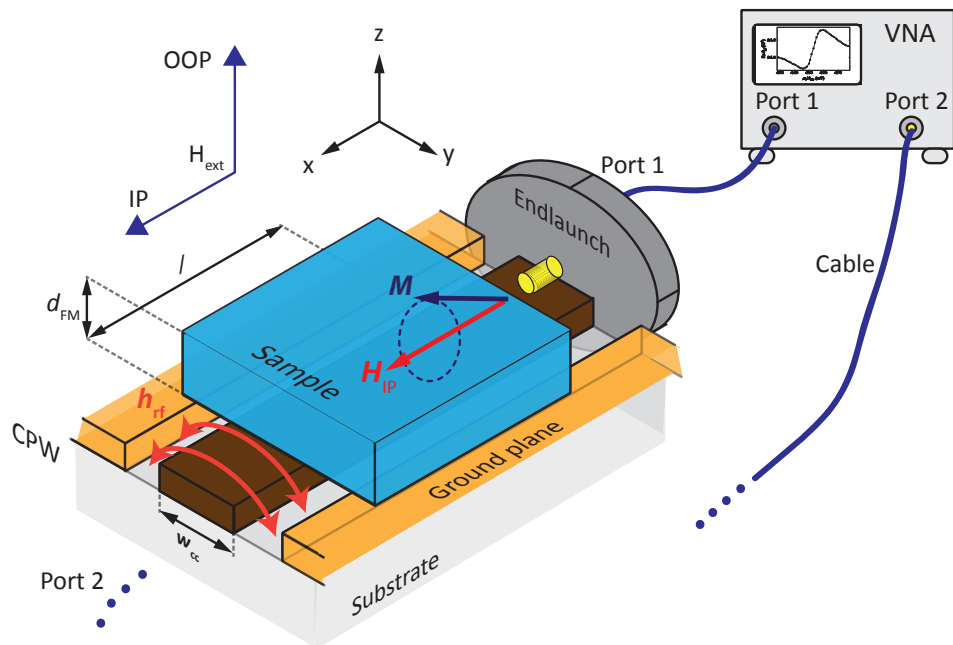


Figure 4.1: Schematic experimental setup for in-plane broadband ferromagnetic resonance [BBFMR]. The sample is placed face-down on a coplanar waveguide [CPW] which consists of a center conductor [brown] and two ground planes [orange]. The CPW is connected to the ports of a vector network analyzer [VNA] via microwave cables attached to the endlaunches. A microwave signal generated by the VNA is coupled into the center conductor via the endlaunches, where it induces an oscillating magnetic field h_{rf} , which drives the magnetization within the sample. Adapted from [72].

The sample is placed face-down on the CPW and the ferromagnetic resonance is excited by a microwave signal generated at port 1 of the VNA and coupled into the CPW via microwave cables attached to endlaunches. In resonance, the sample can absorb energy and we detect a change in the transmitted signal arriving at port 2. We employ transmission measurements where a microwave signal is generated at port 1 and detected at port 2. To this end, we measure the complex transmission parameter S_{21} defined as

$$S_{21} = \frac{V_2}{V_1} = \frac{|V_2|}{|V_1|} e^{i(\phi_2 - \phi_1)}, \quad (4.1)$$

where V_i are the measured complex voltages with magnitude $|V_i|$ and phase ϕ_i of the respective port i . It consists of the background S_{21}^0 caused by the setup and a change of transmission ΔS_{21} caused by the sample. The latter is given by [29]

$$\Delta S_{21} = \frac{S_{21} - S_{21}^0}{S_{21}^0}, \quad (4.2)$$

when presuming a fully impedance-matched rf circuit and neglecting the back-reflected wave S_{11} . The magnetic driving field \mathbf{h}_{rf} in the y-z-plane is generated by an ac charge current through the center conductor, which is a metallic thin film strip with a width $w_{\text{cc}} \simeq 60 \mu\text{m}$. The induced rf-field can be approximated by the Karlqvist equations [84].

$$\begin{aligned} h_y(y, z) &= \frac{1}{\pi} h_0 \left[\arctan \left(\frac{y + \frac{w_{\text{cc}}}{2}}{z} \right) - \arctan \left(\frac{y - \frac{w_{\text{cc}}}{2}}{z} \right) \right] \\ h_z(y, z) &= \frac{1}{2\pi} h_0 \ln \left(\frac{(y + \frac{w_{\text{cc}}}{2})^2 + z^2}{(y - \frac{w_{\text{cc}}}{2})^2 + z^2} \right) \end{aligned} \quad (4.3)$$

Here $h_0 = I/(2w_{\text{cc}})$ is the field amplitude at the center for $y=z=0$. This oscillating magnetic field drives the precession of the sample's magnetization, which in turn induces currents in the CPW according to Faraday's law. On magnetic resonance, these currents oppose the driving currents in the CPW according to Lenz law, such that microwave power is absorbed. By assuming that the sample's inductive coupling adds a complex inductance L_0 in series with the impedance $Z_0 = 50 \Omega$ of the unloaded CPW in a voltage divider model, we can relate the change in transmission ΔS_{21} to L_0 :

$$\Delta S_{21} = \frac{1}{2} \frac{-i\omega L_0}{Z_0 - i\omega L_0} \quad (4.4)$$

The factor $1/2$ is required, as the the complex voltage V_2 is measured between CPW and port 2 and not between the two ports. The sample's inductance L_0 can be calculated with [29]

$$\begin{aligned}
L_0 &= \frac{\mu_0 l}{w_{cc} d_{FM} I^2} \left[\int_{-\infty}^{+\infty} dy \int_{d_{FM}}^{+\delta_s + d_{FM}} dz [\mathbf{q}(y, z) \cdot \hat{\chi}_p(\omega, H_0) \cdot \mathbf{h}_{rf}(y, z, I)] \right] \\
&\quad \cdot \left[\int_{-\infty}^{+\infty} dy \int_{d_{FM}}^{+\delta_s + d_{FM}} dz [\mathbf{q}(y, z) \mathbf{h}_{rf}(y, z, I)] \right] \\
&= \frac{\mu_0 l d_{FM}}{4 w_{cc}} [\chi_{yy}(\omega, H_0) + \chi_{zz}(\omega, H_0)] \eta^2(\delta_s, w_{cc}),
\end{aligned} \tag{4.5}$$

where l is the sample's length on the CPW and the function \mathbf{q} describes the normalized spatial amplitude of the FMR mode [29]. For the fundamental mode, we assume $\mathbf{q} = 1$ over the entire sample. In ip-geometry both susceptibility components χ_{yy} and χ_{zz} have to be taken into account, whereas in oop-geometry, only its y-component χ_{yy} contributes. Additionally the function $\eta(\delta_s, w_{cc})$ accounts for a finite spacing δ_s between sample and coplanar waveguide. It can take values from 1, when they are in direct contact, to zero at infinite distance.

$$\eta(\delta_s, w_{cc}) = \frac{2}{\pi} \arctan\left(\frac{w_{cc}}{2\delta_s}\right) \tag{4.6}$$

With Eq. (4.5) relating the susceptibility $\hat{\chi}_p$ to the inductive coupling strength between CPW and sample L_0 , we can also derive an expression for the complex transmission parameter S_{21} directly scaling with $\hat{\chi}_p$ by inserting Eq. (4.4) under the assumption $\omega L_0 \ll Z_0$ in formula (4.2) and using the upper expression for L_0 from (4.5). We obtain

$$\begin{aligned}
S_{21}(\omega, H_0) &= S_{21}^0(\omega) \cdot (1 + \Delta S_{21}) = S_{21}^0(\omega) \cdot \left(1 - \frac{i\omega L_0}{2Z_0}\right) \\
&= S_{21}^0(\omega) \cdot \left(1 - i \frac{\omega}{2Z_0} \frac{\mu_0 l d_{FM}}{4 w_{cc}} [\chi_{yy}(\omega, H_0) + \chi_{zz}(\omega, H_0)] \eta^2(\delta_s, w_{cc})\right) \\
&= S_{21}^0(\omega) - i A e^{i\phi} [\chi_{yy}(\omega, H_0) + \chi_{zz}(\omega, H_0)].
\end{aligned} \tag{4.7}$$

Here A is the resonance amplitude comprising all the geometrical constants, like for example l and w_{cc} as well as setup parameters, whereas ϕ accounts for the phase change of the signal when traversing the system.

4.2 Measurement procedure

There are two different approaches to conduct BBFMR: On the one hand one can sweep the VNA driving frequency f at a fixed external field H_{ext} in 'frequency-swept FMR' or on the other hand fix f and sweep H_{ext} through H_{res} in the so-called continuous wave CW (mode). For our measurements, we chose the latter and swept H_{ext} within a range of $3\Delta H$ around H_{res} , with the VNA's IF-bandwidth [IFBW] set to 1 Hz at a power level of 0 dBm to obtain a good signal to noise ratio [SNR]. The reason for this choice is the time-consuming field-stabilization process in the Chaos-cryostat slowing frequency-swept FMR down substantially, when compared to the CW-mode.

Most BBFMR measurements in this thesis were conducted in ip-geometry due to the field-range of the horizontal axes of the 3D vector magnet being limited to 2.5 T, which is only

marginally higher than the effective magnetization of $\text{Co}_{25}\text{Fe}_{75}$ at $\mu_0 M_{\text{eff}} = 2.2 \text{ T}$ [44, 45]. This leaves only a very minor frequency range to drive FMR in oop-configuration. In ip-geometry, the Polder-susceptibility $\hat{\chi}_{\text{ip}}$ (3.34) takes the following form [$N_x = 1$, $N_y = 0$, $N_z = 0$]:

$$\hat{\chi}_{\text{ip}} = \frac{\mu_0 M_s}{D} \begin{pmatrix} H_{\text{ext}} + i\frac{\Delta H}{2} & +\frac{i\omega}{\mu_0\gamma} \\ -\frac{i\omega}{\mu_0\gamma} & H_{\text{ext}} + M_s + i\frac{\Delta H}{2} \end{pmatrix} \quad (4.8)$$

$$D = \left(H_{\text{ext}} + M_s + i\frac{\Delta H}{2} \right) \left(H_{\text{ext}} + i\frac{\Delta H}{2} \right) - \left(\frac{\omega}{\mu_0\gamma} \right)^2$$

Here we use the abbreviation $\Delta H = \frac{2\omega\alpha}{\gamma\mu_0}$. To account for the background S_{21}^0 , we fit a linear function $S_{21}^0 = C_0 + C_1 H_{\text{ext}}$ with the complex offset C_0 and slope C_1 following the approach by Nembach *et al.* in [85]. Upon dividing the susceptibility by $\mu_0 M_s$, to stay consistent with the formalism in [29], we obtain the final result for our fitting function

$$S_{21}(H_{\text{ext}})|_{\omega} = C_0 + C_1 \cdot H_{\text{ext}} - iAe^{i\phi} \cdot \frac{\chi_{yy}(H_{\text{ext}}) + \chi_{zz}(H_{\text{ext}})}{\mu_0 M_s}. \quad (4.9)$$

In Fig. 4.2(a) and (b), exemplary raw data of S_{21} as a function of H_{ext} are shown together with the fitted theory curve according to Eq. (4.9). In our measurements, we recorded $S_{21}(H_{\text{ext}})$ in the range from [5-50] GHz in steps of 0.5 GHz. The extracted behaviour of H_{res} and ΔH of the corresponding sample as a function of frequency in ip-geometry is shown in 4.2(c) and (d) respectively, together with the fitting curves following Eq. (3.37) and (3.41) to extract the spectroscopic parameters of the $\text{Co}_{25}\text{Fe}_{75}$ -layer.

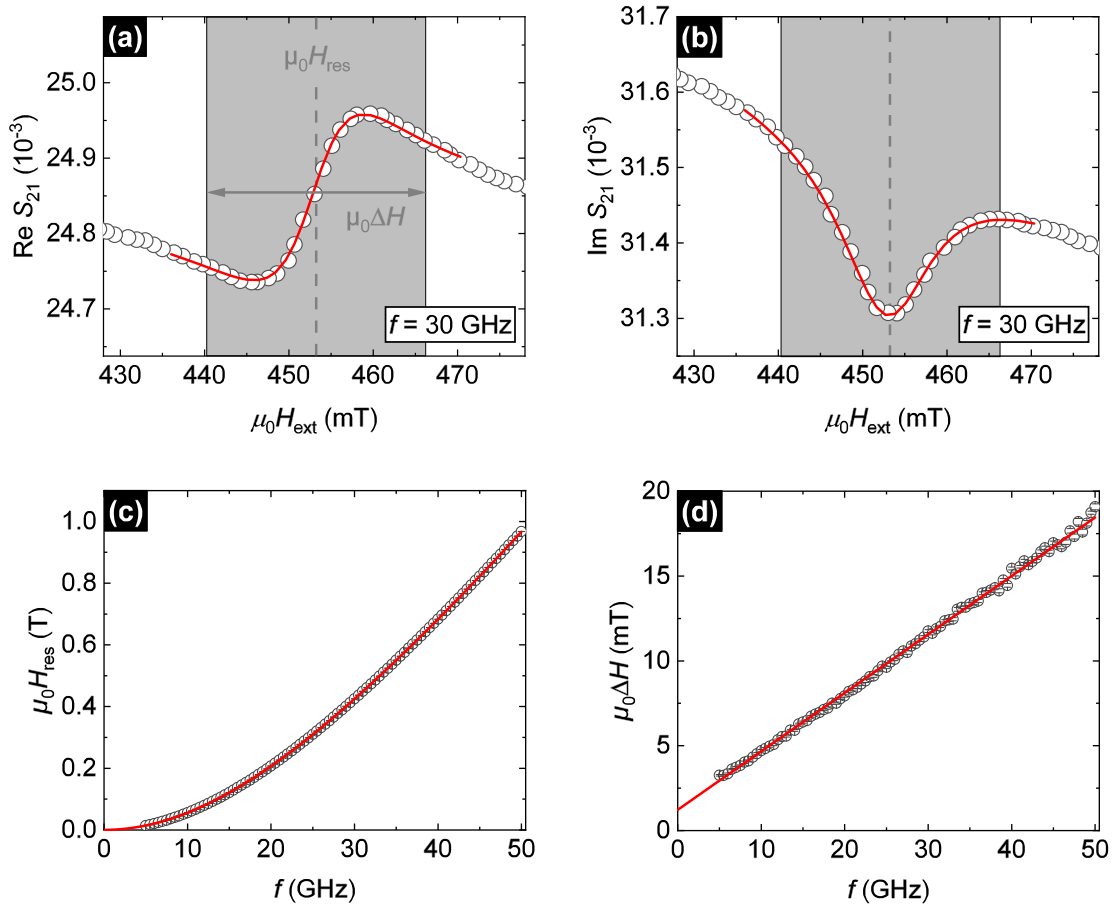


Figure 4.2: Raw data obtained from ip-VNA measurements conducted in the Chaos-cryostat at room temperature of a NbN/Co₂₅Fe₇₅-bilayer comprising [Cu (5 nm)/NbN (16 nm)/Co₂₅Fe₇₅ (3 nm)/Ta (2 nm)]. By fitting the real (a) and imaginary part (b) of the complex susceptibility χ according to Eq. 4.9, the resonance position and linewidth can be extracted. In (c) and (d), the latter are plotted as a function of frequency and fitted according to Eq. (3.37) and (3.41), respectively to extract the spectroscopic parameters of the FM-layer.

4.3 Experimental setup

To conduct BBFMR at cryogenic temperatures, we require an experimental setup, which can couple microwave signals in a wide range of frequencies into an environment with controllable magnetic field and temperature capable of producing temperatures below the T_C [76]. To this end, we used the CHAOS liquid helium cryostat, which utilizes the evaporation of liquid helium through an adjustable needle valve to cool the samples space in the pumped variable temperature insert [VTI] in the range from [2-300] K. Superconducting 3D vector magnets in the liquid helium bath provide the external magnetic field from [0-2.5] T in the horizontal x-y-plane and [0-6] T along the vertical z-axis. A rough sketch of our measurement setup is shown in Fig. 4.3(a).

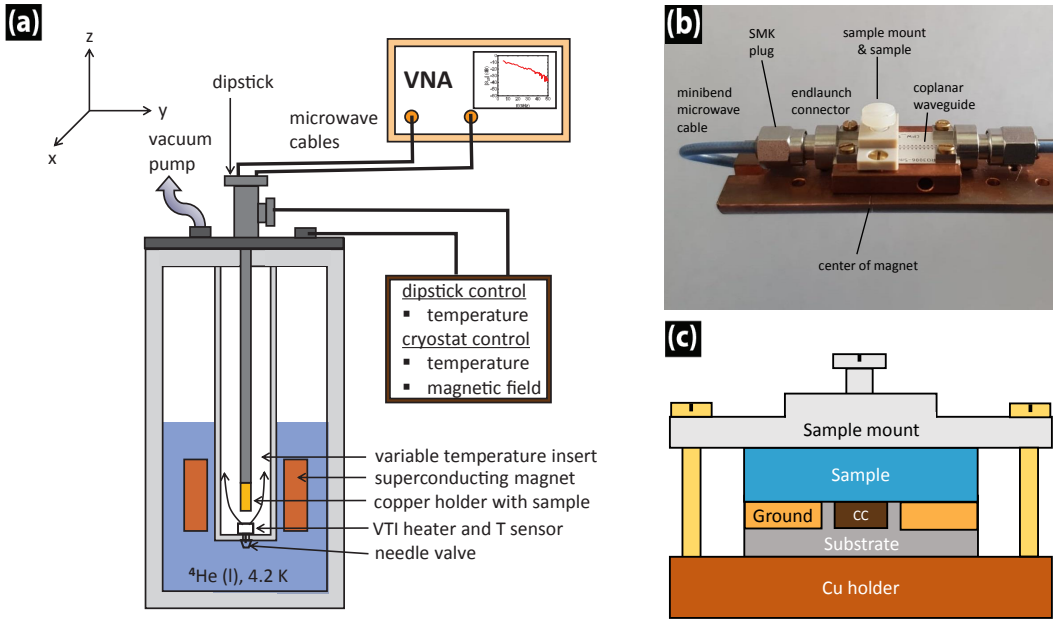


Figure 4.3: (a): Schematic illustration of Chaos helium flow cryostat together with RF measurement dipstick connected to the VNA via microwave cables. The dipstick is inserted into the variable temperature insert [VTI], where the sample temperature is regulated by controlling the helium flow through the needle valve, which is then subsequently evaporated at the VTI heater. The external magnetic field H_{ext} is created by superconducting 3D vector magnets inside the helium tank. Adapted from [86]. (b): Measurement assembly for BBFMR at cryogenic temperatures. The sample is fixed via sample mount on a CPW on a copper holder together with two end launch connectors that are in turn connected to minibend microwave cables. The holder is mounted on the copper lower part of a cryogenic dipstick which contains a temperature sensor and a resistive heater. Replicated from Fig. 2.3 in [87]. (c): Used sample mounting technique. Two brass screws are tightened to attach sample mount and subjacent sample to the CPW and copper holder. An additional plastic screw is used to avoid substrate bending above the CC.

The sample is placed face-down and along its short side [$l = 6$ mm] on a CPW [see Fig. 4.3(c)] on a copper holder at the end of a RF measurement dipstick as shown Fig. 4.3(b). Both ends of the CPW are attached to microwave cables in the dipstick which are in turn connected to a VNA. To ensure equal sample mounting and similar spacing δ_s between sample and CC, we measured S_{21} during mounting and tightened the screws until the magnitude of $|S_{21}|$ took the value $\simeq -27$ dB at 25 GHz. Additional DC wires for a temperature sensor and a resistive heater allow a better sample temperature stability $\Delta T_{\text{sample}} < 10$ mK [86]. In our measurements we set the opening of the needle valve to 18% and used the 2nd heater level of the sample heater range for measurements below 25 K. This resulted in a VTI pressure of $p \simeq 50$ mbar. Higher VTI-pressures had a detrimental effect on our measurements as the flux of helium vapour can cause minor vibrations of the dipstick. Additionally, we used a 20 minutes timer before starting a CW sweep to enhance temperature stability as even small fluctuations ΔT can affect S_{21} . Due to the limited field range [$\mu_0 H_{\text{ext}} \leq 2.5$ T] in oop-configuration, we conducted most of our BBFMR measurements in ip-geometry with $\mathbf{H}_{\text{ext}} \parallel \mathbf{z}$.

5 Superconducting coherence peak in NbN/Co₂₅Fe₇₅-multilayers

We begin our presentation of the experimental results by showing our research on the detection and quantification of the changes in the magnetization dynamics parameters of NbN/Co₂₅Fe₇₅-thin films, when these samples are cooled below their superconducting transition temperature in the CHAOS cryostat. Here, we focus on the investigation of the coherence peak in the Gilbert damping as predicted by [19, 20]. As discussed in Section 3, this coherence peak originates from the enhanced spin transport properties of superconductors at temperatures close to T_C , where an abundance of thermally excited BVQP are formed. To this end, it is important to determine the net contribution of spin pumping to the total extracted α . Thus, we utilize ip-BBFMR measurements on two sample series with a varying Co₂₅Fe₇₅ thickness d_{FM} and with or without a Pt spin sink [Pt (5 nm)/NbN (20 nm)/Co₂₅Fe₇₅ (d_{FM})/Ta (2 nm)] and [NbN (20 nm)/Co₂₅Fe₇₅ (d_{FM})/Ta (2 nm)]. By analysing the ip-BBFMR results for these two sample series, we can directly quantify the spin pumping contribution α_{SP} from the d_{FM} -dependence of α . As a next step, we prove that these results can be extended to cryogenic temperatures by illustrating the negligible changes in the magnetization dynamics parameters for two NbN/Co₂₅Fe₇₅-bilayers with and without a Pt spin sink, recorded over a broad range of temperatures spanning from RT to slightly above T_C . As a final result, we present the ip-BBFMR results for these two samples upon traversing T_C down to the lowest stable temperatures possible in the CHAOS cryostat. Most importantly, we indeed detect a small coherence peak in α in the expected temperature region $[0.7-0.8]T_C$ for both samples. Finally, we utilize our thickness dependent data to quantify the net change in spin pumping α_{SP} and compare our experimental results to the theoretical calculations of Inoue *et al.* illustrated in Fig. 3.5. We conclude this chapter with a discussion of the physical origins of the significant reduction in the height of the coherence peaks in our experiments.

5.1 In-plane-BBFMR results of NbN/Co₂₅Fe₇₅-multiayer sample series

To extract the spin pumping contribution α_{SP} to the total Gilbert damping α , we prepared two Co₂₅Fe₇₅ layer thickness series, one with a Pt spin sink [Pt(5 nm)/NbN (20 nm)/Co₂₅Fe₇₅ (d_{FM})/Ta(2 nm)] and one without [NbN (20 nm)/Co₂₅Fe₇₅ (d_{FM})/Ta(2 nm)] by UHV sputtering. For the Co₂₅Fe₇₅ layer we varied the thickness in the range $1\text{nm} \leq d_{\text{FM}} \leq 6\text{ nm}$ and measured their respective spectroscopic parameters by conducting ip-BBFMR at the Bruker-electromagnet in the frequency range from $5\text{ GHz} \leq f \leq 26.5\text{ GHz}$ at room temperature. The results obtained for effective magnetization $\mu_0 M_{\text{eff}}$ and the Gilbert damping α are plotted as function of $1/d_{\text{FM}}$ in Fig. 5.1. We note that the effective g -factor and the inhomogeneous broadening $\mu_0 H_{\text{inh}}$ did not display a clear dependence on d_{FM} and thus are not shown here. The results are in agreement to the layer thickness series conducted in [36] for Co₂₅Fe₇₅.

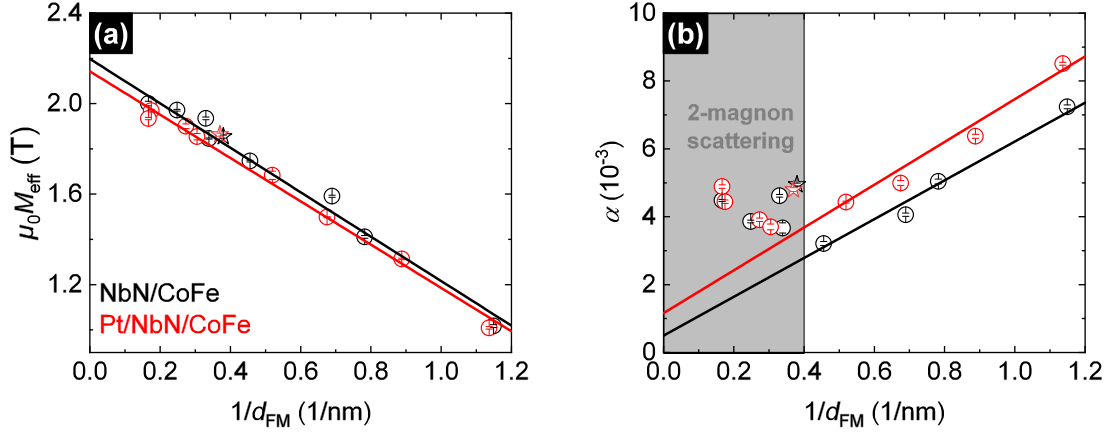


Figure 5.1: Ip-BBFMR results at room temperature for the layer thickness series' comprising NbN (20 nm)/Co₂₅Fe₇₅ (d_{FM})/Ta (2 nm) with [red] and without [black] a Pt (5 nm) spin-sink seedlayer. The effective magnetization (a) and net Gilbert damping (b) are plotted as a function of $1/d_{\text{FM}}$. Their extrapolated saturation magnetizations are $\mu_0 M_s^{\text{noPt}} = (2.20 \pm 0.03)$ T and $\mu_0 M_s^{\text{Pt}} = (2.14 \pm 0.03)$ T. The damping parameter α is fitted linearly in the range, where magnon-magnon scattering is negligible. The resulting fit parameters are listed in Table 5.1. The samples represented with a star symbol are the ones investigated at cryogenic temperatures in the CHAOS cryostat.

From Fig. 5.1 it is clear that for both sample series M_{eff} is directly proportional to $1/d_{\text{FM}}$. We can extract the bulk saturation magnetization $\mu_0 M_s$ from the y-axis intercept. For our two sample series we obtain $\mu_0 M_s^{\text{noPt}} = (2.20 \pm 0.03)$ T [without Pt spin sink] and $\mu_0 M_s^{\text{Pt}} = (2.14 \pm 0.03)$ T [with Pt spin sink]. These results nicely agree with previous experiments conducted in the Master thesis of Luis Flacke and published in Ref. [44]. This confirms that the magnetic properties of the Co₂₅Fe₇₅ are not changed by the growth on the superconducting NbN layer. The extracted Gilbert damping displayed in Fig. 5.1(b) exhibits a much richer behaviour. For $1/d_{\text{FM}} > 0.4 \text{ nm}^{-1}$, we find a linear increase in α for both sample series. In contrast, for $1/d_{\text{FM}} < 0.4 \text{ nm}^{-1}$ [highlighted in grey in Fig. 5.1 (b)], we observe a non-systematic dependence on $1/d_{\text{FM}}$. We attribute this to more pronounced magnon-magnon scattering in the thicker samples, which renders an additional relaxation path for the oscillating magnetization. The magnitude of 2-magnon scattering is strongly influenced by the surface roughness in our thin films and thus may vary from sample to sample, as apparent from the scattering of the data points for thicker films. In order to extract α_{SP} we utilize a linear fit to α for both sample series in the range $1/d_{\text{FM}} > 0.4 \text{ nm}^{-1}$. The slope of this fit directly yields α_{SP} , while the intercept gives the intrinsic Gilbert damping α_0 . We list the extracted fitting parameters in Tab. 5.1.

Series	α_0 [10^{-3}]	α_{SP} [10^{-3} nm]
no Pt	0.50 ± 0.86	5.72 ± 0.69
Pt	1.16 ± 0.38	6.30 ± 0.49

Table 5.1: Gilbert damping contributions extracted from the fit of $\alpha(d_{\text{FM}}^{-1})$ in Fig. 5.1 for both sample series.

The intrinsic Gilbert damping α_0 values are in the high 10^{-4} -/low 10^{-3} -range as expected from previous results in [36, 44, 45] for Co₂₅Fe₇₅. For a better comparison, we utilize α_{SP} to

calculate the spin mixing conductance $G_{\text{eff}}^{\uparrow\downarrow}$ according to [88].

$$\alpha_{\text{SP}} = 2 \frac{\gamma \hbar^2 G_{\text{eff}}^{\uparrow\downarrow}}{4e^2 M_s} \quad (5.1)$$

The resulting $G_{\text{eff,noPt}}^{\uparrow\downarrow} = (2.5 \pm 0.3) \times 10^{14} \Omega^{-1}\text{m}^{-2}$ and $G_{\text{eff,Pt}}^{\uparrow\downarrow} = (2.7 \pm 0.2) \times 10^{14} \Omega^{-1}\text{m}^{-2}$ again quantitatively match the values obtained in [36, 80]. From these results we conclude that the excellent magnetization dynamic properties of the $\text{Co}_{25}\text{Fe}_{75}$ layer are not affected when grown on NbN.

5.2 In-plane-BBFMR results at cryogenic temperatures

In order to extend our measurements to cryogenic temperatures, we inserted two samples, namely a Pt (5nm)/NbN (20 nm)/ $\text{Co}_{25}\text{Fe}_{75}$ (2.6 nm)/Ta (2 nm) and a NbN (20 nm)/ $\text{Co}_{25}\text{Fe}_{75}$ (2.6 nm)/Ta (2 nm) sample into the CHAOS cryostat. We then conducted ip-BBFMR as a function of temperature starting at RT and cooling down to slightly above T_C [$T > 10$ K]. The extracted magnetization dynamics parameters as function of temperature are shown in Fig. 5.2.

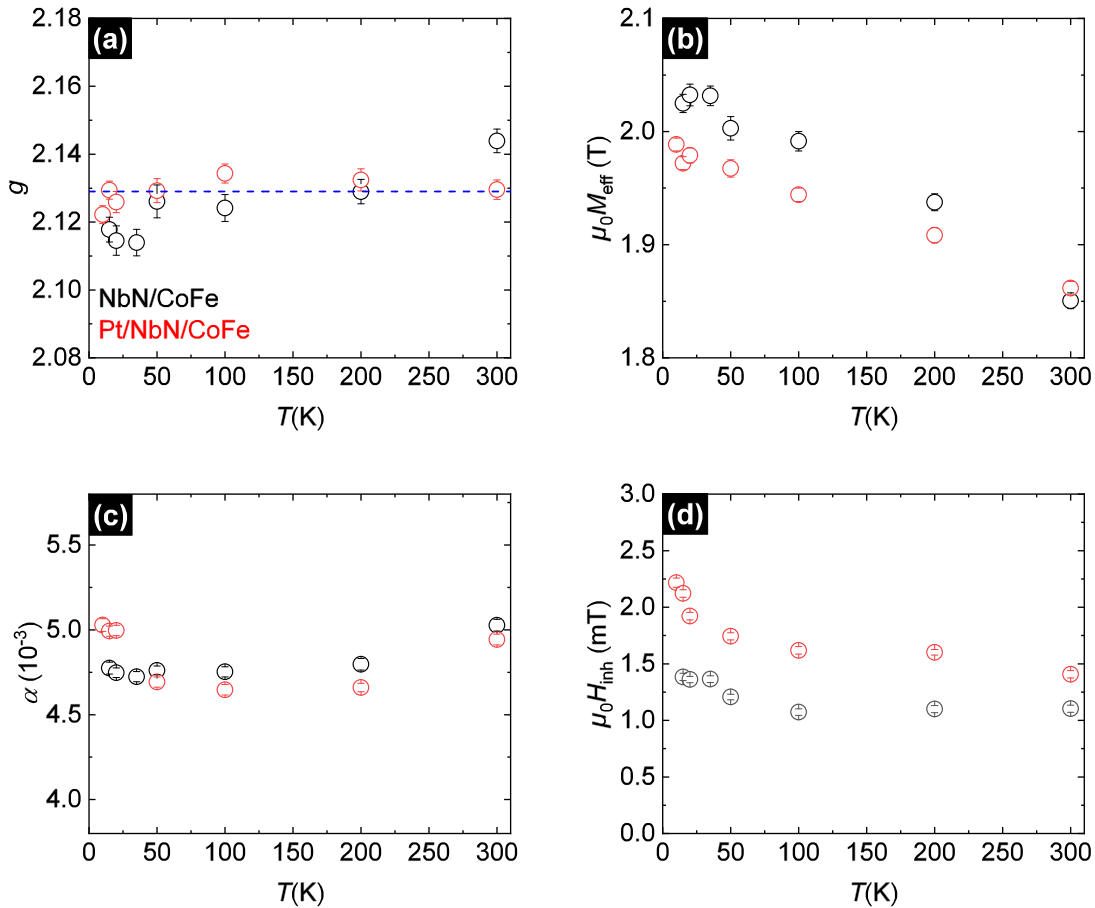


Figure 5.2: Temperature dependence of the magnetization dynamics parameters for the samples investigated in the CHAOS cryostat [black: NbN (20 nm)/Co₂₅Fe₇₅ (2.6 nm)/Ta (2 nm)] and [red: Pt (5nm)/NbN (20 nm)/Co₂₅Fe₇₅ (2.6 nm)/Ta (2 nm)] for $T > T_C$. (a): The g -factor displays no clear dependence on T , while the effective magnetization decreases for increasing temperature due to the thermal excitation of magnons. (c) and (d) illustrate the changes of the Gilbert damping α and inhomogeneous broadening $\mu_0 H_{\text{inh}}$, respectively. The increase in α and $\mu_0 H_{\text{inh}}$ at low temperatures visible in the sample with Pt-seed may originate from the enhanced conductivity of Co₂₅Fe₇₅ for low T , which improves the spin transport into Pt.

As evident from Fig. 5.2(a), the g -factor for both samples remains constant and exhibits no strong temperature dependence. The effective magnetization in Fig. 5.2(b) increases with decreasing T attributed to the corresponding increase in saturation magnetization. Following the same line of arguments, the freezing out of magnon modes and the corresponding contribution of magnon-magnon scattering to α is expected to reduce for lower T . Indeed, in Fig. 5.2(c) we find a decrease in α for $100 \text{ K} \leq T \leq 300 \text{ K}$ for both samples. However, for the sample with Pt spin sink one finds an increase in α for even lower T . This may indicate an enhancement in the spin pumping contribution to α and thus improved spin transport conditions from the Co₂₅Fe₇₅ layer across the NbN layer into the Pt spin sink. For $\mu_0 H_{\text{inh}}$ in Fig. 5.2(d) we find a temperature independent behaviour for the sample without Pt spin sink. In contrast, $\mu_0 H_{\text{inh}}$ increases with decreasing temperature for the sample with Pt spin sink. Overall the spectroscopic parameters of Co₂₅Fe₇₅ exhibit only minor changes with T and hence we can assume that the values for α_{SP} , extracted at 300 K are also valid at cryogenic temperatures.

5.3 Detection of the superconducting coherence peak

Upon cooling the samples down further, we entered the vicinity of the superconducting transition temperature. Here we conducted BBFMR in the range from 2.5 K to $T > T_C$ in steps of 1 K and 0.5 K in the region of interest around $T \approx [0.7-0.8] T_C$. The measured magnetization dynamics parameters as function of the temperature normalized to the samples respective T_C are illustrated in Fig. 5.3.

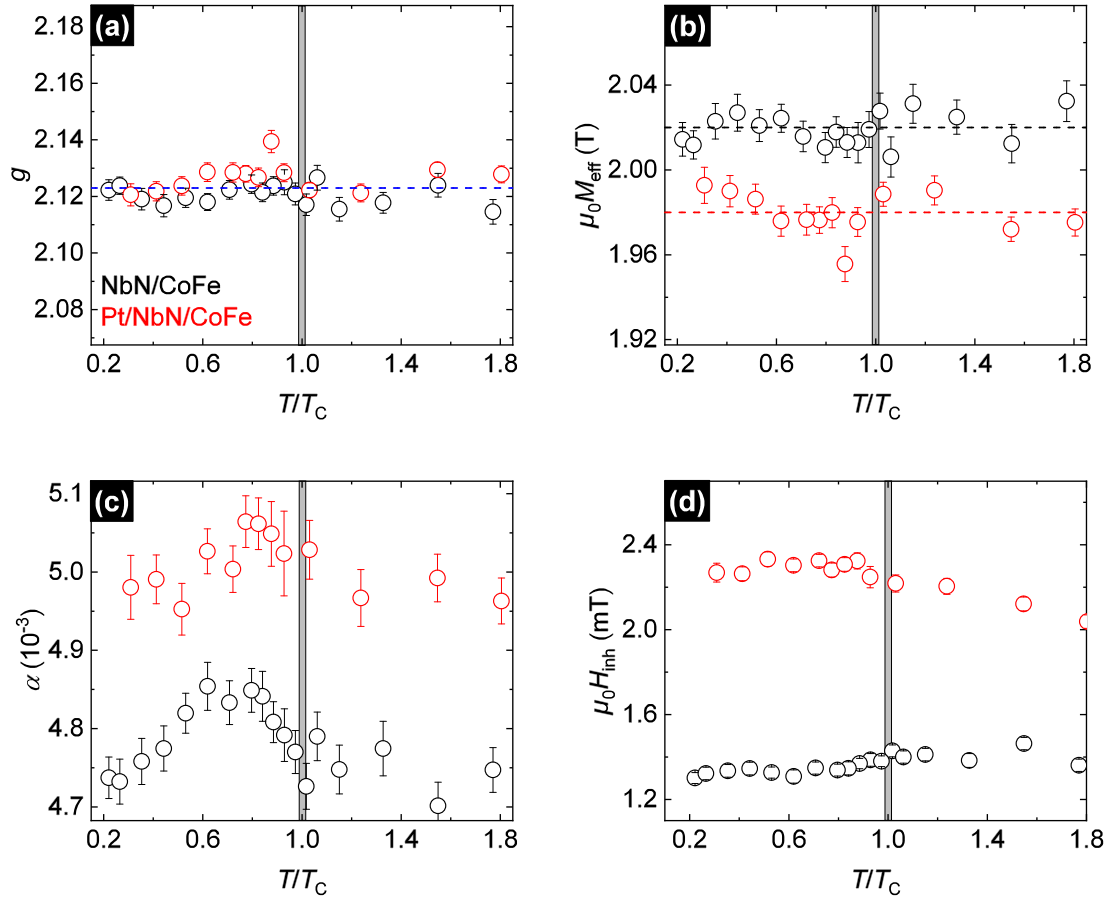


Figure 5.3: Temperature dependence of spectroscopic parameters for the samples investigated in the CHAOS cryostat in the proximity of T_C . Both The g -factor (a) and the effective magnetization (b) display no clear dependence on temperature. (c) and (d) illustrate the changes of the Gilbert damping α and inhomogeneous broadening $\mu_0 H_{\text{inh}}$, respectively. As theoretically predicted, a minor peak in α manifests in both samples for $T \approx [0.7-0.8] T_C$. Minor alterations are also visible in $\mu_0 H_{\text{inh}}$, which slightly increases/decreases at T_C in the sample with/without Pt-seedlayer.

As expected neither the g -factor [see Fig 5.3(a)] nor the effective magnetization $\mu_0 M_{\text{eff}}$ [see Fig 5.3(b)] exhibit any changes once the NbN-layer becomes superconducting and remain roughly constant within the examined range of temperatures. For the damping α in Fig. 5.3(c) we do indeed observe minor peak-like structures with a maximum around $T \approx [0.7-0.8] T_C$ for both samples. However, this maximum in α is more visible in the sample without Pt spin sink [black symbols in Fig.5.3(c)]. The inhomogeneous linewidth $\mu_0 H_{\text{inh}}$ in Fig. 5.3(d) changes only slightly below T_C : For the sample with Pt spin sink, $\mu_0 H_{\text{inh}}$ increases with decreasing T , while for the sample without Pt spin sink, it reduces with

decreasing T . While the origin of this change is unknown, it reveals, that the measurement of the FMR resonance line width ΔH for just one fixed frequency as performed in previous studies [23, 89] is not enough to draw definitive conclusions on the temperature dependence of α . This would also explain the contradictory results of these two publications. While Bell *et al.* observed a reduction in ΔH [89], Jeon *et al.* claim that spin pumping can either be enhanced or suppressed depending on the selected spin sink layer [23]. Our results indicate that because both offset H_{inh} and slope α of ΔH exhibit changes below T_C , one will either observe an increase or decrease in ΔH depending on the chosen microwave frequency f . Thus, only BBFMR conducted over a broad range of frequencies f allows to quantify the changes in α as a function of temperature.

In order to quantitatively compare the magnitude of our coherence peak to the theoretical calculations of Inoue *et al.* in [19], we calculate the spin pumping contribution in the superconducting range normalized to that above T_C using our layer thickness series fit results for α_{SP} from Tab. 5.1

$$\frac{\alpha_{\text{SP}}(T)}{\alpha_{\text{SP}}(T_C)} = 1 + \frac{\Delta\alpha \cdot d_{\text{FM}}}{\alpha_{\text{SP}}}. \quad (5.2)$$

Here $\Delta\alpha$ is the deviation of α from its average value in the normal state [$T_C < T \leq 12$ K]. The results from this analysis are plotted in Fig. 5.4.

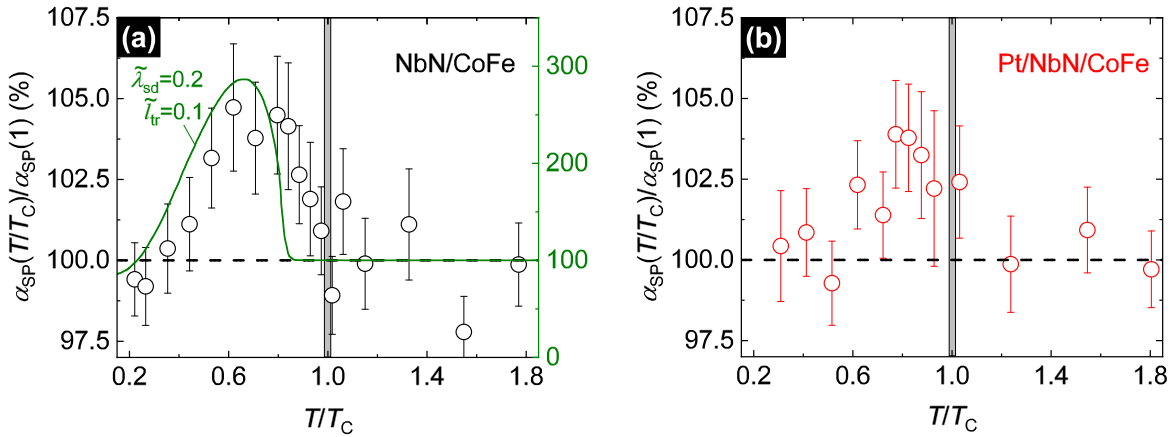


Figure 5.4: Spin pumping contribution to the Gilbert damping α_{SP} normalized by its value in the normal state above T_C as a function of reduced temperature for the NbN/Co₂₅Fe₇₅-bilayers without (a) and with (b) Pt-seedlayer. This procedure allows to compare the magnitude of the coherence peak with the theoretical predictions of Inoue *et al.* [19]. In (a), we additionally plot one exemplary theoretical curve from the results in Fig. 3.5 as a green line. Our peak value is substantially lower than its theoretical counterpart, which may be caused by large values of normalized $\tilde{\lambda}_{\text{sd}}$ and mean free path \tilde{l}_{tr} . The height of the coherence peak has been found to sensitively depend on these two parameters.

Upon matching our experimental results to the theoretical predictions, it becomes apparent that the real coherence peak position is slightly shifted in T and its value of $\approx 5\%$ is an order of magnitude smaller than even the lowest results in [19] for the largest normalized spin diffusion length $\tilde{\lambda}_{\text{sd}} = 100$ and mean free path $\tilde{l}_{\text{tr}} = 90$. For comparison, we use available literature values for $l = 3.96$ Å [90], $\xi_0 \sim 5$ nm [63, 64] and $\lambda_{\text{sd}} = 14$ nm for NbN [91] to calculate the experimental $\tilde{\lambda}_{\text{sd}}^{\text{exp}} = 2.8$ and $\tilde{l}_{\text{tr}} = 0.08$ in our case. Hence the calculations in [19]

would forecast a much larger coherence peak than observed experimentally, but there are several arguments to explain our results. Firstly, the coherence length ξ_0 , by which $\tilde{\lambda}_{\text{sd}}$ and \tilde{l}_{tr} are normalized, depends on the purity of the thin film according to [55,92]

$$\xi(T) = \xi^\infty(T) \left(1 + \frac{\xi^\infty(T)}{l} \right)^{-1/2}, \quad (5.3)$$

and is therefore diminished in our samples. Here $\xi^\infty(T)$ represents the coherence length of an idealized bulk sample in the absence of scattering [$l \rightarrow \infty$]. By inserting the upper literature values in Eq. (5.3), we receive the reduced $\xi(0) \approx 1.4$ nm. Consequently, realistic values for $\tilde{\lambda}_{\text{sd}}^{\text{exp}}$ and \tilde{l}_{tr} are larger by a factor of roughly 4 for our investigated samples, but nonetheless remain much lower than their theoretical counterparts. However, it must be noted that the calculations of Inoue *et al.* [19] were performed for an insulating ferromagnet assuming no spin backflow from the superconducting spin sink. Neither of these presumptions are valid in our case, $\text{Co}_{25}\text{Fe}_{75}$ is a ferromagnetic metal (FM) and spin memory loss may substantially contribute to α_{SP} [81,82]. For a FM the coherence peak is expected to be diminished due to the suppression of superconductivity at its interface when charge carriers from the superconducting layer are able to enter the adjacent FM [28,93,94]. Our results indicate, that NbN is resilient enough to maintain fractional superconductivity even at the interface and thus exhibits a minor coherence peak. To test this conjecture, we fabricated a similar sample using the superconductor Nb, exhibiting much lower critical magnetic fields than NbN, and recorded the magnetization dynamics parameters as function of temperature. The results for α and $\mu_0 H_{\text{inh}}$ for this thin film are illustrated in Fig. 5.5.

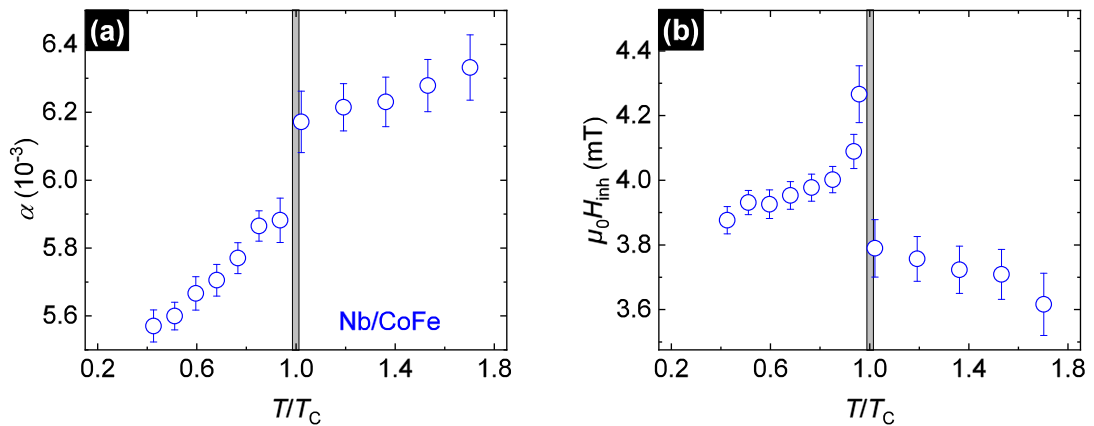


Figure 5.5: Gilbert damping α (a) and inhomogeneous broadening $\mu_0 H_{\text{inh}}$ (b) as a function of reduced temperature for a Nb (40 nm)/ $\text{Co}_{25}\text{Fe}_{75}$ (2.6 nm)/Ta (2 nm) sample. Instead of exhibiting a coherence peak slightly below T_C , the Gilbert damping α abruptly reduces to a lower value and steadily decreases for lower temperatures. This indicates the blocking of spin pumping into the Nb-layer, as superconducting BVQP are suppressed at the interface by the proximity of $\text{Co}_{25}\text{Fe}_{75}$. The further decrease in α for lower T is due to the freezing out of the remaining quasiparticles. Conversely, the inhomogeneous linewidth $\mu_0 H_{\text{inh}}$ discontinuously increases at T_C and converges towards a value that is slightly larger than in the normalconducting range.

As expected, the behaviour of the damping α with temperature in Fig. 5.5(a) is quite different than that of the previous NbN samples, displaying no coherence peak but in-

stead an immediate reduction in α once the Nb-layer transitions into its superconducting state. We attribute this result to the suppression of BVQP to carry angular momentum at the Nb/Co₂₅Fe₇₅-interface, due to the absence of BVQP to carry angular momentum under the presumption that the superconducting phase is greatly depleted in the vicinity of the Co₂₅Fe₇₅-layer and only gradually recovers within the lengthscale $\xi(T)$. Following this chain of reasoning, the observed further decrease in α is due to the freezing out of the remaining BVQP with temperature. These results are in line with those in [89] for Nb, however the observed change in $\mu_0 H_{\text{inh}}$ at T_C weakens this comparison, as Bell *et al.* merely observed a decrease in total FMR linewidth ΔH at a fixed microwave frequency $f = 9.5$ GHz. These results for the Nb/Co₂₅Fe₇₅ samples support our theory that the detected superconducting coherence peak is much smaller than theoretic predictions due to the interfacial reduction of the SC phase. Nonetheless, it can be detected because of the resilient nature of NbN enabling it to manifest a substantial amount of BVQP for angular momentum transport at the interface. Hence, no such coherence peak is observed in samples containing the less resilient Nb instead. Taking into account additional measurements conducted during this thesis [Appendix B.2], we find a superconducting coherence peak of varying magnitude and temperature width in almost all NbN/Co₂₅Fe₇₅-samples. This strengthens the case, that its origin lies in the manifestation of BVQP to carry angular momentum and not in noise-related measurement fluctuations around T_C . Thus, our measurements provide first time evidence that the manifestation of a superconducting coherence peak is not limited to FMI/SC-heterostructures, but can also be detected in low-damping FM in direct contact to resilient SC's.

6 Manifestations of superconductivity in VNA-based BBFMR

In the previous section, we illustrated how the magnetization dynamics parameters of a thin film of the ferromagnet $\text{Co}_{25}\text{Fe}_{75}$ change with temperature when brought into contact with a superconductor. In particular, we were able to detect a peak-like structure in its damping parameter α , which indicates enhanced spin transport properties below T_C . However, these are not the only measurement parameters exhibiting changes when the sample becomes superconducting. In addition, both the perfect conductance and expulsion of magnetic fields in the superconductor significantly affect key measurement quantities in VNA-based BBFMR. This chapter is dedicated to illustrate and explain these changes. The perfect conductance effect alters the sample's surface impedance Z_{eff} and thereby the magnitude of the complex transmission parameter $|S_{21}|$. We illustrate these changes and utilize an existing formula for $|S_{21}(Z_{\text{eff}})|$ derived by Schmidt *et al.* [95] together with an expression of Z_{eff} for superconductors to fit the recorded behaviour of $|S_{21}|$ as a function of sample temperature. By using this approach we obtain estimates for both T_C and the London penetration depth λ_L of the superconducting layer. We compare the latter to literature values and discuss the feasibility of our method. Thereafter we show how the expulsion of the oscillatory magnetic driving field \mathbf{h}_{rf} in the superconducting layer can either enhance or reduce the inductive coupling strength L_0 between sample and CPW and consequently the FMR amplitude. For the former case the ferromagnet is sandwiched between SC and CPW, effectively being driven from both sides, while in the latter case the superconductor is grown on top of the FM layer and attenuates \mathbf{h}_{rf} and thereby diminishes L_0 . To this end, we used $\text{Ni}_{80}\text{Fe}_{20}$ [Permalloy, Py] as our FM, because the magnetization dynamics parameters of $\text{Co}_{25}\text{Fe}_{75}$ change dramatically, when altering the growth conditions. Permalloy has a higher α making the detection of changes in spin pumping more challenging, but is more resilient and thus does not exhibit changes upon for example inverting the sample's stack sequence. Finally, we discuss how these parameters vary depending on the used superconducting material and show our experimental results for different superconductors.

6.1 Effect of superconducting layers on the complex transmission parameter $|S_{21}|$

In our experiments, a very simple way to determine the transition temperature for our samples placed in the CHAOS cryostat is to measure the magnitude of the complex transmission parameter $|S_{21}|$ on the VNA while cooling it down slowly. Once the sample temperature drops below T_C , a dramatic increase in $|S_{21}|$ occurs rising further for lower temperatures until it approximately takes the form of an unloaded CPW for these cryogenic temperatures as illustrated in Fig. 6.1(a).

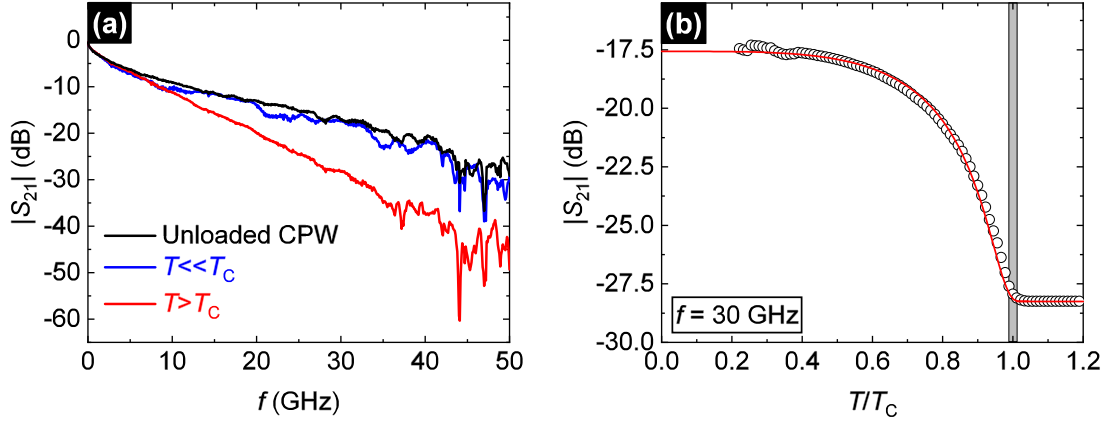


Figure 6.1: (a): Magnitude of the complex transmission parameter $|S_{21}|$ as function of frequency f for a sample with the stack sequence Pt (5 nm)/NbN (16 nm)/Py (6 nm)/Ta (2 nm) recorded both slightly above and far below the superconducting transition temperature T_C . A drastic improvement in transmission below T_C becomes apparent, with $|S_{21}|$ taking roughly the form of an unloaded CPW. In (b) the recorded change in $|S_{21}|$ at a fixed microwave frequency $f = 30$ GHz is shown as a function of normalized temperature, steeply increasing once the NbN-layer becomes superconducting. It is fitted using Eq. (6.4) to extract the London penetration depth $\lambda_L = (1.12 \pm 0.06) \mu\text{m}$.

To unambiguously attribute this phenomenon to the sample's superconducting transition, we recorded $|S_{21}|$ at a fixed frequency of 30 GHz as a function of sample temperature. The results are shown in Fig. 6.1(b). As the observed changes in $|S_{21}|$ manifest abruptly and no further alterations occur for $T > T_C$, it is reasonable to presume that the changes in $|S_{21}|$ are indeed caused by the onset of superconductivity. For a quantitative description of the observed behaviour we used the results of Schmidt *et al.* in [95]. They derived an expression for $|S_{21}|$ normalized by the transmission parameter of an unloaded CPW $|S_{21}^0|$.

$$\left| \frac{S_{21}}{S_{21}^0} \right| \propto \exp\left(-\frac{|\gamma_0 Z_{\text{eff}}| l}{2Z_0}\right). \quad (6.1)$$

Here l represents the sample's length on the CPW, Z_{eff} and Z_0 stand for the thin film surface impedance and unloaded CPW-impedance, respectively. Additionally $\gamma_0 = \omega/v_{\text{ph}}$ is the complex propagation factor and v_{ph} is the phase velocity of microwaves in the CPW. From Eq. (6.1) it becomes clear why for $T < T_C$, $|S_{21}|$ looks like that of an unloaded CPW as the magnitude of Z_{eff} is very small in the superconducting phase. For its quantitative description in our SC/FM-heterostructures we use the following expression [55]:

$$Z_{\text{eff}}(\omega) = \frac{1}{2} \mu_0^2 \omega^2 \lambda_{\text{eff}}^3 \sigma_0 \frac{n_n}{n} - i \cdot \mu_0 \omega \lambda_{\text{eff}} \quad (6.2)$$

In this case, σ_0 is the normal conductance of the superconducting layer, n_n/n is the fraction of the normalconducting phase below T_C and λ_{eff} is the thin film London penetration depth defined in Eq. (3.9). We simplify Eq. (6.2) by only considering its imaginary part, usually being the dominant contribution for temperatures not too close to the transition temperature. The T -dependence of $|S_{21}|$ is then just governed by that of the London penetration

depth λ_L , most commonly described by the Casimir-Görter-model [96]:

$$\lambda_L(T) = \frac{\lambda_L(0)}{\sqrt{1 - (T/T_C)^4}} \quad (6.3)$$

By inserting Eq. (6.2) into (6.1) and taking its temperature dependence into account, we obtain the final result

$$|S_{21}| = |S_{21}^{\text{NC}}| + |\Delta S_{21}| \exp\left(-\frac{|\gamma_0| l \mu_0 \omega \lambda_L^2(0)}{2Z_0 d_{\text{SC}} (1 - (T/T_C)^4)}\right) \quad (6.4)$$

for our fitting function with $|S_{21}^{\text{NC}}|$ representing the complex transmission magnitude in the normalconducting range and $|\Delta S_{21}|$ being its change below T_C . The resulting fit curve is shown in Fig. 6.1(b). When applying the values $d_{\text{SC}} = 16$ nm, $l = 6$ mm, $v_{\text{ph}} = 1.8 \cdot 10^8$ m/s [used by Schmidt et. al. in Ref. [95]] and $Z_0 = 50 \Omega$, the extracted London penetration depth is $\lambda_L = (1.12 \pm 0.06) \mu\text{m}$, which is considerably larger than literature values for NbN, ranging from 200 nm to 400 nm [42, 43]. However, just like for the coherence peak in section 5, a correction factor according to [55, 92] must be applied of the form

$$\lambda_L(0) = \lambda_L^\infty(0) \left(1 + \frac{\xi^\infty(0)}{l}\right)^{1/2}. \quad (6.5)$$

Using $l = 3.96 \text{ \AA}$ [90] and $\lambda_L^\infty(0) = 300$ nm, we obtain $\lambda_L(0) \approx 1 \mu\text{m}$, which agrees well with our experimental results. It should be noted that an unusually large λ_L has been observed for SC/FM-bilayers in Ref. [97], where it was attributed to the depletion of the superconducting fluid density n_s at the FM interface. However, in our samples the large λ_L may as well be explained by finite size effects and a reduction in the superconducting coherence length ξ_0 due to changes in the normalconducting mean free path of the superconducting layer as established in chapter 5.

6.2 Effect of superconductivity on the inductive coupling strength L_0

Another key property which indicates the transition into superconductivity is the amplitude of the FMR signal, which is a direct measure of the inductive coupling strength between sample and CPW, being either enhanced or attenuated below T_C depending on the stack sequence. If the superconductor is located below the ferromagnetic $\text{Ni}_{80}\text{Fe}_{20}$, we see a stronger FMR signal and conversely if it is 'sandwiched' between FM and CPW, it diminishes the detected change in transmission ΔS_{21} . Exemplary BBFMR-measurement results as a function of temperature for two NbN/ $\text{Ni}_{80}\text{Fe}_{20}$ -heterostructures with opposite stack sequence, are illustrated in Fig. 6.2. For the sample with $\text{Ni}_{80}\text{Fe}_{20}$ being placed in between the NbN layer and the CPW we indeed observe a drastic increase in the FMR signal strength below T_C [see Fig. 6.2 (a)]. In contrast, if the NbN is in between the $\text{Ni}_{80}\text{Fe}_{20}$ layer and CPW we find as predicted a reduction in the FMR signal strength in the superconducting state [see Fig. 6.2 (b)].

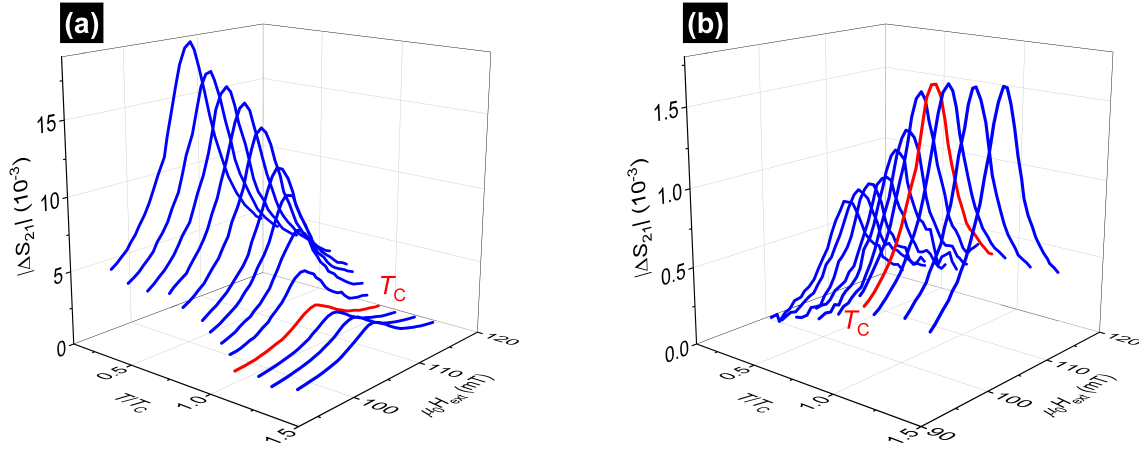


Figure 6.2: Magnitude of the change in $|S_{21}|$ in the vicinity of the ferromagnetic resonance recorded at a frequency of 10 GHz and plotted as a function of both reduced temperature and external field for two samples with opposite stack sequences [(a): Pt (5 nm)/NbN (16 nm)/Ni₈₀Fe₂₀ (6 nm)/Ta (2 nm), (b): NbN (5 nm)/Ni₈₀Fe₂₀ (6 nm)/NbN (16 nm) /Pt (5 nm)]. In (a), an immediate enhancement in FMR amplitude manifests below T_C increasing further for lower temperatures to approximately 7 times the magnitude of the normal range. For the inverted sample (b) the opposite effect occurs with the signal strength decreasing to about 0.4 times its value above T_C . This indicates that this phenomenon is caused by superconducting screening currents, which either enhance or attenuate the CPW driving field h_{rf} depending on the sample's stack sequence.

These findings can be well explained by superconducting image charge currents repelling the field of the CPW h_{rf} . Hence we are dealing with a system, where the ferromagnetic layer is exposed to driving fields from both the CC of a CPW at distance δ_s , h_{rf}^{CPW} , and superconducting image currents flowing directly at its interface h_{rf}^{SC} . Depending on the sample's stack sequence, these two components either add for Substrate/SC/FM-samples, where the ferromagnet is driven from both sides, or oppose each other for substrate/FM/SC-structures, where the superconducting image currents effectively shield the FM from h_{rf}^{CPW} . Both cases are schematically illustrated in Fig. 6.3(b).

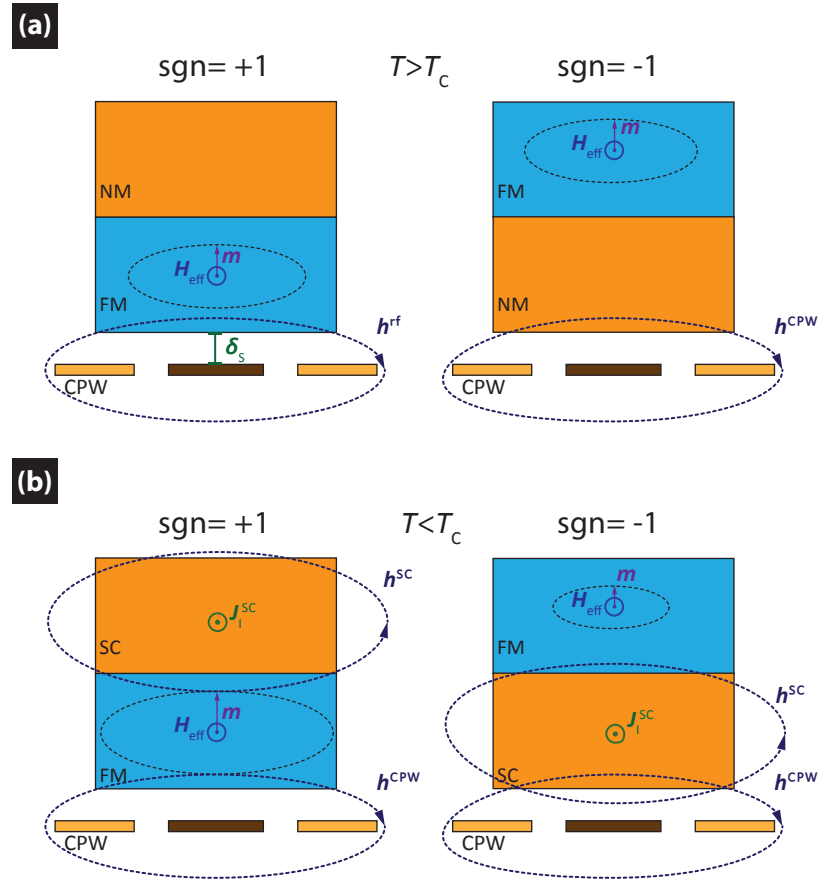


Figure 6.3: Illustration of the driving field components h^i affecting the ferromagnetic sample for $\text{sgn} = \pm 1$ above (a) and below (b) the superconducting transition temperature T_C . For $T > T_C$, the FM-layer is asymmetrically driven from its top side by the driving field of the CPW h^{CPW} . This results in an equal precession magnitude for the macrospin magnetization \mathbf{m} independent of the stack sequence. In the case $T < T_C$, superconducting image currents create an additional driving field contribution h^{SC} , which depending on the stack sequence either enhances or depletes the total driving field h^i and correspondingly the precession amplitude of \mathbf{m} for $\text{sgn} = +1$ or $\text{sgn} = -1$ respectively.

In order to quantify the resulting change in inductive coupling strength L_0 we follow the approach by Rosa in [98] and model the superconductor and center conductor of the CPW as two current-carrying sheets of width w_{cc} , length l and separation δ_s , which provides a mutual inductance L_{12} of

$$L_{12} = \frac{\mu_0}{4\pi} 2l \left[\ln \left(\frac{2l}{R} - 1 \right) \right], \quad (6.6)$$

where R is given by

$$R = \sqrt{w_{cc}^2 + \delta_s^2} \left(\frac{\delta_s}{\sqrt{w_{cc}^2 + \delta_s^2}} \right)^{\left(\frac{\delta_s}{w_{cc}} \right)^2} \exp \left[\frac{\delta_s}{w_{cc}} \arctan \left(\frac{\delta_s}{w_{cc}} \right) - \frac{3}{2} \right]. \quad (6.7)$$

Below T_C , the superconducting NbN is in the Meißner-phase under the assumption $h_{\text{rf}} \ll H_{C1}$ and responds to the oscillatory driving field \mathbf{h}_{rf} by generating image currents I_{SC} to prevent the magnetic field from entering. By treating the superconducting NbN-layer as a perfectly conducting sheet of width w_{cc} and length l , its geometric self-inductance L_{geo} can

be calculated as [98]:

$$L_{\text{geo}} = \frac{\mu_0}{4\pi} 2l \left[\ln \left(\frac{2l}{w_{\text{cc}}} + \frac{1}{2} \right) \right] \quad (6.8)$$

The total inductance of the superconducting layer L_{SC} comprises both the geometric self-inductance L_{geo} and the kinetic inductance L_{kin}

$$L_{\text{SC}} = L_{\text{geo}} + L_{\text{kin}}. \quad (6.9)$$

For superconductors, the kinetic energy of charge carriers is non-negligible due to their long mean free paths. In a charge current, it is equivalent to the energy invested in creating the corresponding magnetic field, which can be related to the kinetic inductance L_{kin} of a conductor. Regarding superconducting thin film strips of length l , width w_{cc} and thickness d , the latter takes the form [99, 100]

$$L_{\text{kin}}(T) = \frac{\mu_0 \lambda_{\text{L}}(T)^2 \cdot l}{w_{\text{cc}} d}, \quad (6.10)$$

in the case $d < \lambda_{\text{L}}$, which is valid in our samples. Following the single lumped-element-inductor approach in [29] to describe the sample-CPW-system, we can relate I_{SC} to known quantities with

$$I_{\text{SC}} = \frac{L_{\text{SC}} I}{L_{12}} \quad (6.11)$$

By using the quantified superconducting image currents in Eq. (6.11), we can derive a new expression for the net total driving field h_{rf} at the position of the FM layer

$$\begin{aligned} h_{\text{rf}} &= h_{\text{rf}}^{\text{CPW}} + h_{\text{rf}}^{\text{SC}} = \frac{\eta(z, w_{\text{cc}})}{2w_{\text{cc}}} (I + \text{sgn} \cdot I_{\text{SC}}) \\ &= \frac{\eta(z, w_{\text{cc}}) I}{2w_{\text{cc}}} \left[1 + \text{sgn} \cdot \frac{\ln \left(\frac{2l}{w_{\text{cc}}} + \frac{1}{2} \right) + \frac{2\pi\lambda_{\text{L}}^2}{w_{\text{cc}}d}}{\ln \left(\frac{2l}{R} - 1 \right)} \right], \end{aligned} \quad (6.12)$$

where $\text{sgn} = \pm 1$ denotes the stack sequence [$\text{sgn} = +1$ for Substrate/SC/FM and $\text{sgn} = -1$ for Substrate/FM/SC]. Both contributions to h_{rf} are plotted in Fig. 6.4(a) as function of δ_{s} for $\lambda_{\text{L}} = 1 \mu\text{m}$ to match the results of section 6.1.

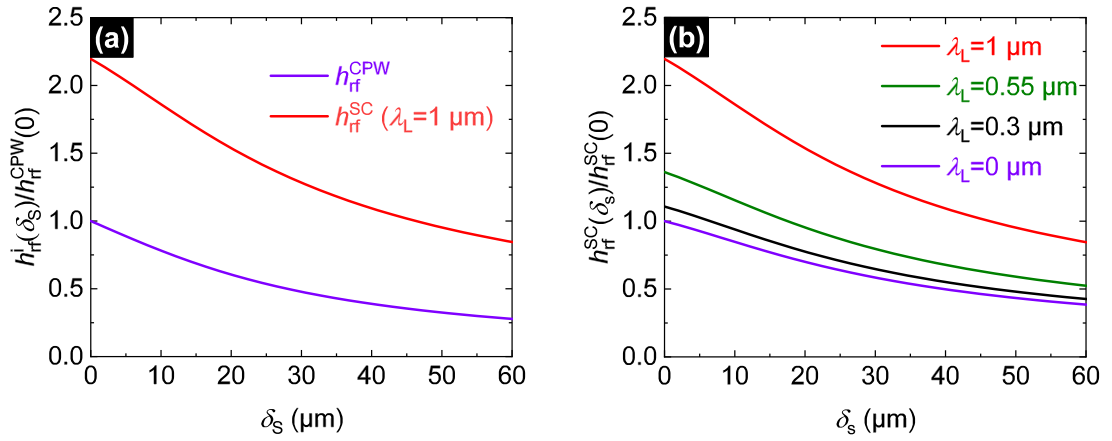


Figure 6.4: (a): Decay of the driving field components felt by the ferromagnet as a function of spacing between sample and CPW δ_s . $h_{\text{rf}}^{\text{CPW}}$ represents the contribution generated by the CC of the CPW, while the field generated by image currents in the SC in direct contact to the ferromagnetic layer is represented by $h_{\text{rf}}^{\text{SC}}$. (b): Decay of the driving field component generated by the SC $h_{\text{rf}}^{\text{SC}}$ as function of δ_s using varying λ_L . For lower λ_L , its contribution is reduced. In the absence of kinetic inductance [$\lambda_L = 0 \mu\text{m}$] the magnitude of $h_{\text{rf}}^{\text{SC}}$ is equal to that of the CC.

If we instead insert lower values for λ_L which are more in line with the literature results, the magnitude of $h_{\text{rf}}^{\text{SC}}$ decays with decreasing λ_L and converges towards $h_{\text{rf}}^{\text{CPW}}$ for $L_{\text{kin}} = 0 \text{ H}$ as illustrated in Fig. 6.4(b). The net driving field h_{rf} scales quadratically with the inductive coupling strength L_0 in Eq. (4.5) so we can determine the alteration of the FMR amplitude caused by superconducting image currents with

$$\frac{L_0^{\text{SC}}}{L_0} = \left(\frac{h_{\text{rf}}^{\text{CPW}} + h_{\text{rf}}^{\text{SC}}}{h_{\text{rf}}^{\text{CPW}}} \right)^2. \quad (6.13)$$

Since we are able to extract δ_s experimentally by applying the data processing of Berger *et al.* [29], outlined in depth in chapter 7, we can obtain a quantitative estimate of λ_L by adjusting its value so that the theoretical enhancement/attenuation factors for the distance δ_s^{exp} match our experimental findings. The resulting theoretical L_0^{SC}/L_0 for $\text{sgn} = +1$ (a) and $\text{sgn} = -1$ (b) are shown in Fig. 6.5 as function of δ_s for varying values of λ_L . We marked the experimentally determined sample spacing $\delta_s^{\text{exp}} = [20-30] \mu\text{m}$ and scaling factor ranges for L_0^{SC}/L_0 [extracted from Fig. 7.5(a) and (b)] as grey rectangles.

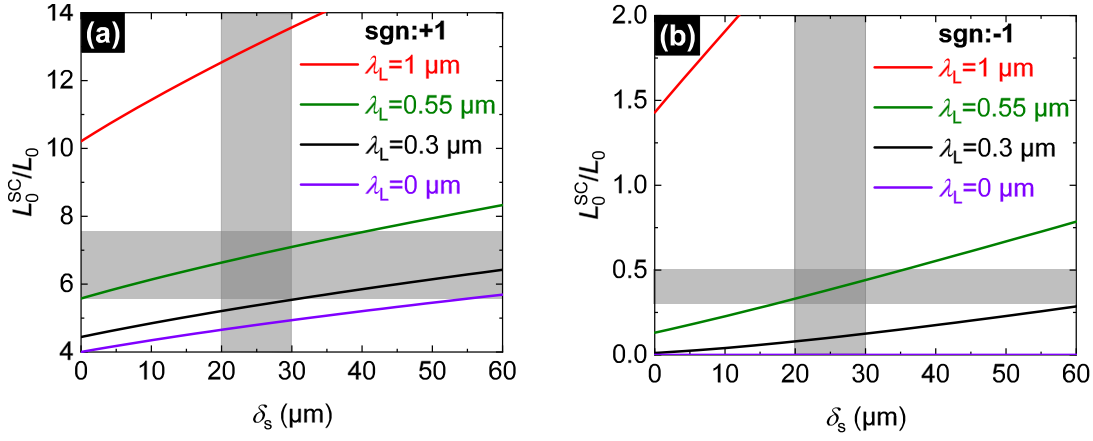


Figure 6.5: Theoretically expected enhancement (a)/ attenuation (b) of the FMR-amplitude as a function of δ_s for varying λ_L . From the data analysis procedure in [29], we extract $\delta_s^{\text{exp}} = [20-30] \mu\text{m}$ and observe an experimental increase in amplitude of 5.5-7.5 for $\text{sgn} = +1$ and an attenuation of 0.3-0.5 for $\text{sgn} = -1$. These ranges are marked as grey boxes.

Notably the absence of L_{kin} leads to the overall increase of 4 times in signal amplitude for $\text{sgn} = +1$ essentially describing a cavity resonator, where the sample is symmetrically driven from both sides. Intuitively in this case $\text{sgn} = -1$ means perfect screening of any driving field. For a value of $\lambda_L = 550 \text{ nm}$, the curve of L_0^{SC}/L_0 intersects the experimental results in both (a) and (b) simultaneously. Conversely when using the result from the previous section for $\lambda_L > 1 \mu\text{m}$, we receive too large magnification for $\text{sgn} = +1$ and even enhancement for $\text{sgn} = -1$. The most likely explanation for this discrepancy is the fact that perfect screening of external magnetic fields in our superconducting thin films is likely not valid with a fraction of $h_{\text{rf}}^{\text{CPW}}$ transmitting the SC in reality. Hence our quantitative model overstates the effect of superconductivity in our samples.

6.3 Results for FM/SC-bilayers using different superconductors

In the previous sections we found, that both the complex transmission factor $|S_{21}|$ as function of temperature and the change in inductive coupling strength between sample and CPW L_0^{SC}/L_0 below T_C can be modelled by analytic expressions that both depend strongly on the London penetration depth λ_L . Hence when using a different superconducting material these parameters are expected to exhibit dramatic changes, which would lend credence to our theoretical calculations. To this end, we grew samples with comparable stack sequence and changed the material of the superconducting layer, thereby altering the London penetration depth λ_L . We investigated the enhancement factor L_0^{SC}/L_0 for $\text{sgn} = +1$ of three substrates with Pt (5 nm)/X/Ni₈₀Fe₂₀ (6 nm)/Ta (2 nm), where X represents Nb (40 nm), Nb₇₀Ti₃₀N (16 nm) and NbN (16 nm) respectively. Here, we had to grow a substantially thicker film of Nb to obtain an experimentally accessible T_C . Additionally, we recorded their complex transmission factors $|S_{21}|$ as a function of temperature at 30 GHz [Fig. 6.6] and fitted them according to Eq. (4.2) to extract λ_L . The results are listed in the table of Fig. 6.6.

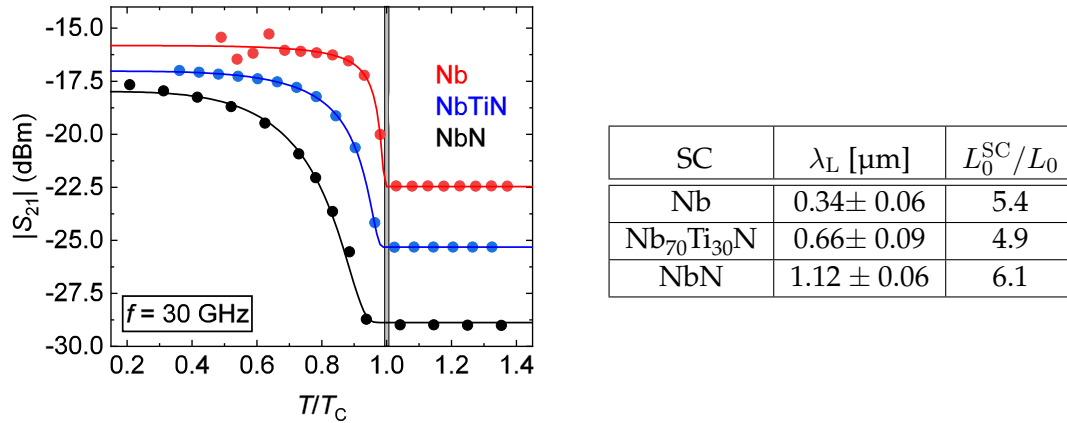


Figure 6.6: Left: Recorded behaviour of $|S_{21}|$ as a function of temperature at the fixed frequency $f = 30$ GHz together with a fitted theory curve according to Eq. (6.4) to extract the London penetration depth λ_L for samples comprising Pt (5 nm)/X/Ni₈₀Fe₂₀ (6 nm)/Ta (2 nm), where X represents Nb (40 nm), Nb₇₀Ti₃₀N (16 nm) and NbN (16 nm) respectively. Right: Table listing the extracted values of λ_L as well as the enhancement factor L_0^{SC}/L_0 for the used superconducting materials. The raw data from which the latter was extracted is given in B.3.

From the results in Fig. 6.6 it becomes clear, that the behaviour of $|S_{21}(T)|$ indeed varies with the used superconducting material apparent in the sharpness of its transition in the vicinity of T_C . As expected the London penetration depth λ_L is the largest for NbN and the lowest for Nb and is also larger than literature values by a factor of 4 for all the investigated materials [55]. This is again attributed to the growth of relatively 'dirty' SC with low mean free path l or the depletion of the superconducting fluid density at the SC/FM interface. Overall both the fit quality and the observed changes in the behaviour of $|S_{21}(T)|$ with the used SC material indicate that our approach, while being overly simplified, indeed provides a measure of λ_L . For the enhancement factor, we found that L_0^{SC}/L_0 is roughly constant for the used superconducting materials being only slightly larger for NbN than in the other samples. However, in the case of the thicker sample comprising Nb, it is unreasonable to compare this quantity with the other superconductors as it may contain larger image currents and consequently screen a bigger fraction of the external driving field. The enhancement factor for Nb₇₀Ti₃₀N can be explained reasonably well assuming a London penetration depth $\lambda_L = 300$ nm being roughly half the value used for NbN which agrees well with literature values [101].

Lastly, we discuss the expected temperature dependence of our model, which is rather complicated as the two contributions to L_{SC} scale opposite with temperature as L_{geo} decreases with the superconducting image currents and L_{kin} increases proportional to $\lambda_L^2(T)$. Yet the observed effects as function of temperature in Fig. 6.2 decrease monotonously with rising T , following the expected behaviour of L_{geo} in the absence of L_{kin} . Here, it must be noted that the validity of our local-response model, where the superconducting current distribution mirrors that of the CC, is limited, however the development of a more sophisticated approach taking into account the magnitude of electromagnetic waves propagating from the CC and spreading throughout the superconducting layer goes beyond the scope of this thesis. Therefore, we can only hand-wavily argue, that the image currents tra-

verse a rectangular path with a width that might be substantially larger than that of the CC effectively reducing the impact of L_{kin} . This train of thought is an alternate explanation for the discrepancy between our theoretically predicted and experimentally measured enhancement factor. Furthermore a 7-fold increase in FMR-amplitude has already been observed in samples containing thick Au backing layers instead of superconductors and thus in the absence of a sizeable L_{kin} [95]. These experimental results seem to indicate that our theoretical model may not suffice to describe the observed effect. There are several arguments to explain an enhancement of more than 4 in BBFMR-experiments. For one thing in thin films, it is feasible to assume that a fraction of the external oscillatory driving field h_{rf} transmits the sample without being absorbed by the FM. This fraction is likely to change in the presence of a superconducting layer below its transition temperature. Alternatively, we note that the CPW detects only the upper half of the flux Φ_{dyn} generated by the precessing macrospin \mathbf{M} of the FM layer in the normal state. This fraction is enhanced below T_C , where the underlying superconductor expels the lower half of Φ_{dyn} from its interior via image currents and thereby essentially enhances the flux felt by the CPW. Consequently in the superconducting state the FM is not only driven with twice the driving field \mathbf{h}_{rf} , enhancing the signal amplitude by a factor of 4, but the CPW also detects twice the net flux generated by the dynamically precessing \mathbf{M} . This would give rise to an overall signal-enhancement factor of 8. We assume that in reality all these effects play a role and would need to be taken into account for a realistic model of the physics in this system.

7 Inductive detection of Spin-Orbit Torques in SC/FM heterostructures

The development of novel spintronics devices for memory or logical applications requires the fast switching of the magnetization M in ferromagnetic layers via means of parameters that are easily controllable and applicable in nanoscale environments. For this purpose spin-orbit torques [SOT] are of vast interest as they allow the control of M with electrical currents or fields [72] as first demonstrated by Miron *et al.*, who used in-plane currents through a NM with large spin-orbit interaction to switch the perpendicular magnetization of a FM [102].

The physical origin of these torques is the coupling of the electron's orbital angular momentum with its spin, which can be used in manifold ways to affect the ferromagnetic magnetization. A prominent example is the conversion of charge currents through a heavy metal with large SOI into a perpendicular spin current via means of spin-dependent scattering mechanisms [103] and directing it into an adjacent FM, where it can exert a torque on M . This effect is called the spin Hall effect [SHE] [104, 105].

We phenomenologically distinguish between two types of SOT depending on their orientation with respect to M : The damping- and field-like SOT. As the name suggests, damping-like torques have the same symmetry as the damping-contribution of the LLG equation and point towards the equilibrium position of the magnetization. The previously explained SHE is one example [106]. Conversely, the symmetry of field-like torques is that of an external magnetic field applied perpendicular to both M and the damping-like torques. As an example we name the Rashba-Edelstein effect, where a current flowing at a NM/FM-interface exerts a field-like torque via Rashba-spin-orbit interaction [107, 108].

For now we have only been talking about effects, where charge currents in NM/FM-thin films create SOT and thereby affect the magnetization. However, we know from Onsager reciprocity [109] that the reversed process, where a dynamically precessing ferromagnet induces a charge current flow, is also possible. The most common example for Onsager reciprocity in this system is the relation between Faraday's and Ampère's law. Here, a precessing magnetization in the FM layer induces a charge current in the NM due to Faraday's law. On the other hand, a charge current flowing in the normal metal according to Ampère's law creates an Oersted field, which acts on the magnetization in the ferromagnet [72]. The method to detect SOT outlined in this chapter relies on this reciprocity and probes the inverse spin orbit torques [iSOT], in contrast to other methods probing the direct SOT like e.g. employed by Miron *et al.* [102].

We start our analysis of the spin-orbit torques in SC/FM-heterostructures with the goal to detect and quantify the spin current \mathbf{j}_s injected from our FM via spin pumping into the Pt layer by investigating the iSHE in these samples and comparing it for samples with and without spin sink layer. To this end, our first task was to reduce the layer thickness of NbN d_{SC} as much as possible while maintaining a reasonable T_C to increase the magnitude of \mathbf{j}_s entering the Platinum. We hence reduced d_{SC} from 20 nm to 16 nm in our experiments. Additionally we aimed to invert the sample's stack sequence from Substrate/NM/FM [$\text{sgn} = +1$] to Substrate/FM/NM [$\text{sgn} = -1$] as the anticipated sign change in the parameters related to SOT would allow us to unambiguously attribute them to the

corresponding field- and damping-like iSOT effects. As explained in Chapter 6, we used $\text{Ni}_{80}\text{Fe}_{20}$ as our FM instead of $\text{Co}_{25}\text{Fe}_{75}$ for its resilient growth properties. Within the course of this chapter we will illustrate and compare the results of BBFMR in magnetization dynamics parameters and iSOT analysis for 4 FM/SC-samples varying both $\text{sgn} = \pm 1$ and with or without a Pt spin sink. Their stack sequences are shown in Tab. 7.1, where the used framing color also represents the color of their data points in the following plots of this chapter.

	no Pt spin sink	Pt spin sink
$\text{sgn} = +1$		
$\text{sgn} = -1$		

Table 7.1: List of samples, whose BBFMR results are on display in this chapter. We varied both the stack sequence $\text{sgn} = \pm 1$ and the application of a Pt (5 nm) spin sink layer to investigate their respective changes in the parameters related to iSOT. The used colour of the sample framing denote that used for the experimental results of this chapter and the number in brackets denotes the thickness of the respective layer in nm.

We begin the discussion of our experimental results by illustrating the magnetization dynamics parameters of these samples and compare them to that obtained for $\text{Co}_{25}\text{Fe}_{75}$ from chapter 5. As a follow up, we turn our attention to the iSOT in these samples. We use the amplitude A and phase ϕ from the fits of our BBFMR raw data to determine the normalized inductance \tilde{L} and show how to extract the so-called iSOT conductivities ($\sigma_f^{\text{SOT}} - \sigma_f^{\text{F}}$) and σ_d^{SOT} from its slope in the real and imaginary part. In similar fashion to the results of chapter 5, we verify that these parameters exhibit only minor changes when cooling the samples down to cryogenic temperatures slightly above T_C and thereby verify that this method of quantifying SOT is also valid for low temperatures. We then show results for \tilde{L} below T_C and discuss how the method of [29] has to be adapted for SC/FM-heterostructures. Thereafter, we plot the inductive coupling strength \tilde{L}_0 as well as the iSOT conductivities ($\sigma_f^{\text{SOT}} - \sigma_f^{\text{F}}$) and σ_d^{SOT} as function of the reduced temperature and discuss the dramatic changes manifesting in the superconducting range. For the former σ_d^{SOT} , we are able to relate our observations to the so-called quasiparticle mediated inverse spin Hall effect [QMISHE] [30], while changes in the latter have to our knowledge not been reported yet. However, we presume its origin is a Rashba-like confinement of electrons at the SC/FM-interface by the BCS-gap parameter Δ . To conclude our experimental results, we show the iSOT data obtained in symmetric SC/FM/SC-sandwiches and in oop-geometry.

7.1 Magnetization dynamics parameters of NbN/Ni₈₀Fe₂₀-bilayers below T_C

We begin by illustrating the magnetization dynamics parameters of the NbN/Ni₈₀Fe₂₀ samples at cryogenic temperatures in the vicinity of T_C in Fig. 7.1. Their temperature dependence upon cooling from RT to low temperatures is shown in the Appendix B.4. In particular the temperature dependence of α will provide us with insight on what to expect for the damping-like iSOT σ_d^{SOT} in the superconducting state.

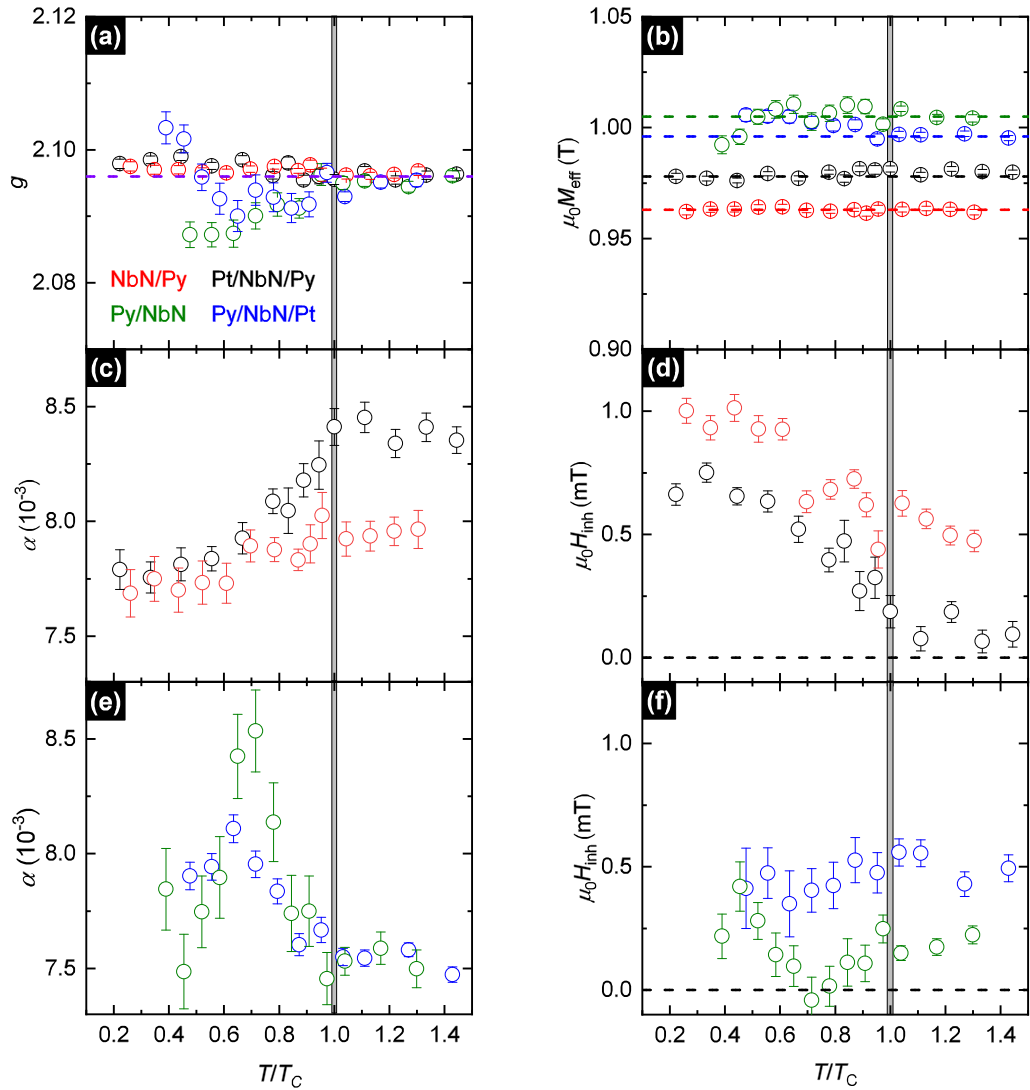


Figure 7.1: Temperature dependence of magnetization dynamics parameters for the samples from Tab. 7.1 measured in the CHAOS cryostat in the range from above T_C to 2 K. Both The g -factor (a) and the effective magnetization (b) remain constant throughout all samples. (c) and (d) illustrate the changes of the Gilbert damping α and inhomogeneous broadening $\mu_0 H_{\text{inh}}$ respectively for the samples with $\text{sgn} = +1$. The apparent decrease in α indicates a suppression of spin pumping into the superconductor. In panels (e) and (f) the Gilbert damping α and inhomogeneous broadening $\mu_0 H_{\text{inh}}$ for the samples with $\text{sgn} = -1$ are shown, respectively. Here an increase in α becomes apparent at temperatures below T_C .

In agreement with the results for NbN/Co₂₅Fe₇₅ heterostructures both g -factor [Fig. 7.1(a)] and effective magnetization $\mu_0 M_{\text{eff}}$ [Fig. 7.1(b)] remain roughly constant within the exam-

ined range of temperatures for all samples. For more clarity, we plotted α and inhomogeneous broadening $\mu_0 H_{\text{inh}}$ separately for the samples with stack sequence $\text{sgn} = +1$ and $\text{sgn} = -1$. Regarding the former in Fig. 7.1(c) & (d), we observe a continuous decrease in damping α decaying more gradually than for the Nb/Co₂₅Fe₇₅-film in Fig. 5.5 and remaining constant for even lower temperatures. Notably, their damping differs above T_C , due to spin pumping into Pt, and takes approximately the same value for $T \ll T_C$. This strongly indicates that in these samples spin pumping in the superconducting state is also mediated by BVQP and hence it freezes out for lower temperatures. However, we do not detect a coherence peak in neither sample. We attribute this to the larger FMR resonance width ΔH in Permalloy, where subtle changes of α_{SP} are overshadowed by other contributions to α . Again, we observe a change in $\mu_0 H_{\text{inh}}$ below T_C , the origin of this observation is not clear. Surprisingly, in samples with the inverted stack sequence $\text{sgn} = -1$ in Fig. 7.1(e) & (f), a coherence peak manifests itself again, which is especially pronounced in the green data points of the NbN/Ni₈₀Fe₂₀-bilayer devoid of Pt. For this finding we must make several remarks:

- The growth of NbN on Permalloy led to detrimental superconducting properties in the inverted samples with a reduced transition of 6-8 K instead of from 9-11 K and thereby likely entailed a SC/FM-interface that is less transparent to the injection of spin currents. Hence, we observe a lower total Gilbert damping α in these samples. According to Gubin *et al.* [58], a reduced mean free path l is a possible explanation for the observed reduction in T_C with respect to the samples with $\text{sgn} = +1$. As established in chapter 5, this reduces the superconducting coherence length ξ_0 and thereby the normalized theoretical parameters $\tilde{\lambda}_{\text{sd}}$ and mean free path \tilde{l}_{tr} , which in turn determine the magnitude of the coherence peak. Their drastic reduction in the inverted samples might give rise to a visible peak.
- We note that a perfect inversion of the stack sequence for the $\text{sgn} = +1$ samples is not possible as Permalloy couldn't be grown on a Ta seedlayer while still maintaining comparable magnetization dynamics parameters. Therefore, we chose to provide for it the same growth conditions as in the normal case and grew a thin NbN seedlayer, that is not becoming superconducting on itself.
- Lastly, we must note that the signal strength reduction to 0.4 times its magnitude in the normal state in the inverted samples affects the fitting quality for worse signal to noise ratios and leads to falsified results. An indicator of this is that $\mu_0 H_{\text{inh}}(T)$ mirrors the behaviour of $\alpha(T)$ in contrast to the results in chapter 5, where we detected peak-like structures in samples with enhanced FMR-amplitudes.

While we can not entirely rule out that the results in (e) are indeed generated by the manifestation of BVQP, we deem the problematic fitting process with low signal to noise ratio the more likely origin of this result.

7.2 Spin-Orbit Torques in NbN/Ni₈₀Fe₂₀-heterostructures

7.2.1 Results in the normalconducting range

For the inductive method to analyse iSOT we start by plugging the background-corrected change in the complex transmission parameter ΔS_{21} as defined in Eq. (4.2) into Eq. (4.9) and obtain

$$\Delta S_{21} = \frac{S_{21} - S_{21}^0}{S_{21}^0} = -i \frac{Ae^{i\Phi}}{C_0 + C_1 H_0} \frac{[\chi_{yy}(\omega, H_0) + \chi_{zz}(\omega, H_0)]}{\mu_0 M_s}. \quad (7.1)$$

This result is inserted into Eq. (4.5), which relates ΔS_{21} to the inductive coupling strength L between sample and CPW under the usual assumption $\omega L_0 \ll Z_0$ to obtain

$$\tilde{L} = \frac{1}{\mu_0 M_s} \frac{Ae^{i\Phi}}{C_0 + C_1 H_0} \frac{Z_0}{\pi f} \quad (7.2)$$

where we introduced the normalized inductance $\tilde{L} = L/[\chi_{yy}(\omega, H_0) + \chi_{zz}(\omega, H_0)]$.

The results of this data processing are shown in Fig. 7.2(a) and (b) displaying \tilde{L} in real and imaginary part respectively, for all the samples enlisted in Tab. 7.1 at room temperature.

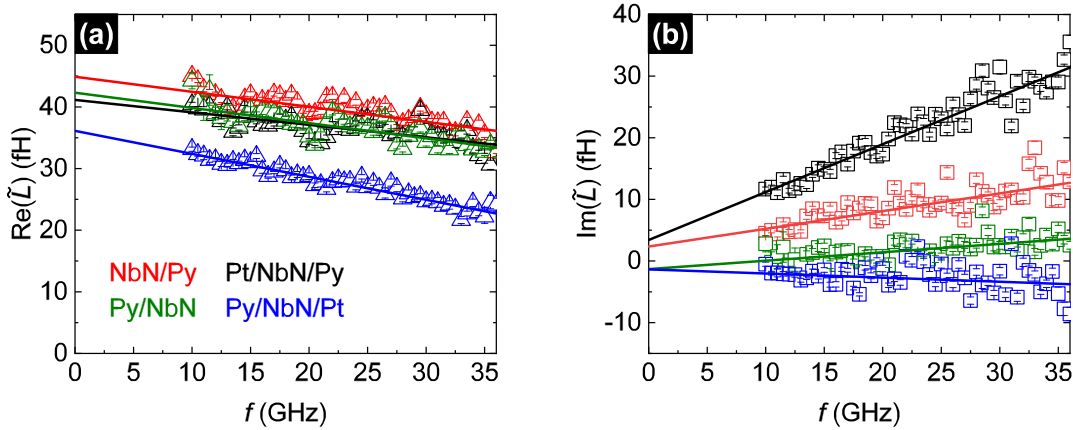


Figure 7.2: Real (a) and imaginary part (b) of the normalized inductance \tilde{L} at room temperature for all the investigated samples. The y-axis intercept of $\text{Re}(\tilde{L})$ in (a), denoting the inductive coupling strength L_0 is almost the same in all samples, but the absence of a sign change of the slopes in (a) upon stack sequence inversion indicate varying Faraday and Rashba-Edelstein contributions ($\sigma_f^{\text{SOT}} - \sigma_f^{\text{F}}$). This shows, that inversion of the stack sequence leads to different interfacial properties at the SC/FM-interface. The samples containing a Pt spin sink exhibit a large iSHE as apparent from the slopes of $\text{Im}(\tilde{L})$ in (b).

The real parts of the normalized inductive coupling strength $\text{Re}(\tilde{L})$ in Fig. 7.2(a) have a similar y-axis intercept for all of the samples and decay linearly with frequency. For its imaginary part $\text{Im}(\tilde{L})$ in Fig. 7.2(b), the samples display different behaviours. The one with $\text{sgn} = +1$ containing Pt exhibits a large positive slope, while its inverted counterpart displays a slight negative slope. The samples without platinum spin sink both show small positive slopes. All converge towards the origin for zero frequency, which is expected as in the DC limit [$f = 0$ Hz], the inductance must be strictly real.

The behaviour of \tilde{L} in real and imaginary part can be linearly described with

$$\text{Re}(\tilde{L}) = \tilde{L}_0 + \text{Re}(\tilde{L}_j) \cdot f \quad (7.3)$$

$$\text{Im}(\tilde{L}) = \text{Im}(\tilde{L}_j) \cdot f. \quad (7.4)$$

We distinguish between the frequency-independent normalized inductive coupling strength offset \tilde{L}_0 between ferromagnetic layer and CC as defined in Eq. (4.5) and the complex slope \tilde{L}_j . This term stems from currents flowing in the normal metal that are induced by the oscillating part of the magnetization $\partial\mathbf{m}/\partial t$ and are hence linear in frequency. With the help of \tilde{L}_j we can extract the spin orbit torque conductivity σ^{SOT} , which is a complex quantity that comprises both field- and damping like spin-orbit torques. In analogy to Ohm's law $\mathbf{j} = \sigma\mathbf{E}$, it relates $\partial\mathbf{m}/\partial t$ to the charge current in the normal metal [29]

$$\sigma^{\text{SOT}} = \sigma_{\text{d}}^{\text{SOT}} + i(\sigma_{\text{f}}^{\text{SOT}} - \sigma_{\text{f}}^{\text{F}}). \quad (7.5)$$

Here 'f' and 'd' denote the field- and damping-like spin orbit torques respectively. The former corresponds to both Faraday 'F' and inverse Rashba-Edelstein effect ($\sigma_{\text{f}}^{\text{SOT}} - \sigma_{\text{f}}^{\text{F}}$), while the latter $\sigma_{\text{d}}^{\text{SOT}}$ quantifies the inverse spin Hall effect. In our samples $\sigma_{\text{d}}^{\text{SOT}}$ is primarily created by the conversion of spin currents originating from the spin pumping into heavy metals like e.g. Pt with large SOI.

The inductive coupling strength \tilde{L}_j between NM and CPW is related to σ^{SOT} as follows:

$$\tilde{L}_j = i \cdot \text{sgn} \cdot L_{12} \eta(\delta_s, w_{\text{cc}}) \frac{\hbar\omega}{4M_{\text{s}}} \sigma^{\text{SOT}}, \quad (7.6)$$

where $\eta(\delta_s, w_{\text{cc}})$ accounts for the finite spacing as defined in Eq. (4.6) and L_{12} is the mutual inductance between sample and CPW. We note that the polarity of \tilde{L}_j depends on the stack sequence. The FM layers in our samples are commonly sandwiched between various materials and we hence observe contributions to σ^{SOT} from both sides. As we will see, in most samples this is not a problem, as in the presence of heavy metals the impact of one side will be dominant, however in their absence deviations in the behaviour of σ^{SOT} from typical expectations can occur. We select the same sign convention for sgn as used in chapter 6.

By again modelling the sample-CPW system as two identical current-carrying sheets with finite spacing δ_s , we can apply Eq. (6.6) for their mutual inductance L_{12} . By applying this data procedure, we are hence able to extract the spin orbit torque conductivities ($\sigma_{\text{f}}^{\text{SOT}} - \sigma_{\text{f}}^{\text{F}}$) and $\sigma_{\text{d}}^{\text{SOT}}$ out of our BBFMR raw data from the obtained frequency-dependence of \tilde{L} . In Fig. 7.3 we plot these quantities as function of temperature in the range above T_{C} .

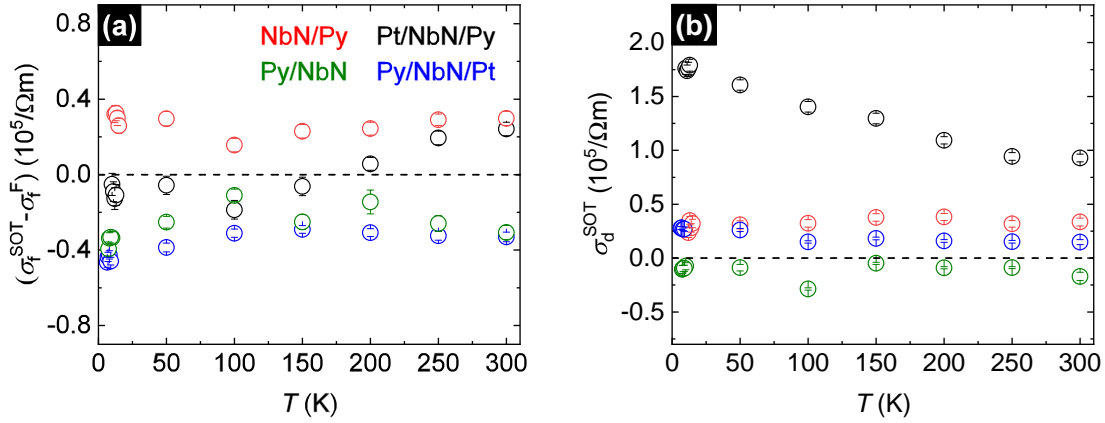


Figure 7.3: Extracted field- (a) and damping-like (b) iSOT conductances ($\sigma_f^{\text{SOT}} - \sigma_f^{\text{F}}$) and σ_d^{SOT} plotted as a function of T in the normal state for a broad range of temperatures spanning from RT to slightly above T_C . Both iSOT parameters remain roughly constant for all samples except for the Pt/NbN/Ni₈₀Fe₂₀-trilayer with $\text{sgn} = +1$ including a Pt seedlayer. Here we observe a decrease in σ_d^{SOT} and a sign change in ($\sigma_f^{\text{SOT}} - \sigma_f^{\text{F}}$) with rising temperature. We attribute the former to enhanced spin pumping properties and the latter to stronger Faraday currents in Pt for low temperatures.

From these results, it becomes apparent that the iSOT in our samples remain roughly constant with temperature save for the black data points of the Pt/NbN/Py-trilayer, which exhibit a sign change in ($\sigma_f^{\text{SOT}} - \sigma_f^{\text{F}}$) and a substantial decrease in the magnitude of σ_d^{SOT} . Starting our discussion with the field-like SOT in Fig. 7.3(a), we note that the samples with matching sgn also display similar ($\sigma_f^{\text{SOT}} - \sigma_f^{\text{F}}$) at room temperature. We attribute their growing divergence with reducing T to a stronger contribution of Faraday currents in the Pt layer for its enhanced conductivity. Upon comparing samples with opposite sgn , we note that they possess a similar magnitude, but opposite signs. A possible explanation for this is a Rashba-like confinement of electrons at the bottom NbN/Ni₈₀Fe₂₀-interface in all samples. Following this train of thought, the opposite sign is just an artefact of our data procedure and the upper FM/SC-interface in our inverted samples is indeed of low transparency and hence not contributing to ($\sigma_f^{\text{SOT}} - \sigma_f^{\text{F}}$). This argument supports the results of section 7.1, where we attributed their lower α to reduced spin pumping. For the damping-like σ_d^{SOT} in Fig. 7.3(b), the observations are more straightforward. It is generated by the conversion of spin pumping into charge currents via the iSHE in heavy metals like Pt or Ta. Consequently, we observe a substantial σ_d^{SOT} in the black data points of the Pt/NbN/Py-trilayer with a Pt seed- and Ta cappinglayer. The contributions of these two materials add due to their opposite sgn and spin Hall angle sign. In order to single out the impact of the Ta-layer to σ_d^{SOT} , we turn our attention to the red data points of the sample identical except for the Pt-seedlayer. Here, we observe a smaller positive value roughly constant with temperature. We deduce that the resulting T -dependence in the black data points is caused by enhanced spin pumping into Pt at lower T . For the inverted samples we observe a low σ_d^{SOT} , which indicates only minor spin pumping in these samples. The negative sign for the green data points belonging to the inverted sample without Pt can only be explained by spin pumping into the bottom NbN-layer under the assumption of a minor negative spin Hall angle following the results in [31]. This backs the assumption of a transparent bottom

NbN/Ni₈₀Fe₂₀-interface in the inverted samples. Notably, the growth of a Pt cap layer still impacts σ_d^{SOT} despite of the bad quality of the top Ni₈₀Fe₂₀/NbN-interface. Consequently, we detect a small but finite contribution of spin pumping into Pt in the inverted samples. As a final remark, we note that one can use σ_d^{SOT} in our samples to quantify the spin Hall angle Θ_{SH} of Pt, Ta and NbN in the spirit of [81], but forego its determination here as we are dealing with complicated multistacks, where multiple materials contribute to the total σ_d^{SOT} . From a qualitative viewpoint, we can explain the results well by assuming they are governed by spin pumping into these respective layers.

7.2.2 Results in the superconducting range

For the data below T_C , we observe dramatic changes to \tilde{L} . Depending on the stack sequence, we either observe an enhancement or attenuation of \tilde{L} and hence we plot $\tilde{L}(f)$ separately for the samples with $\text{sgn} = +1$ (a) and $\text{sgn} = -1$ (b) in Fig. 7.4.

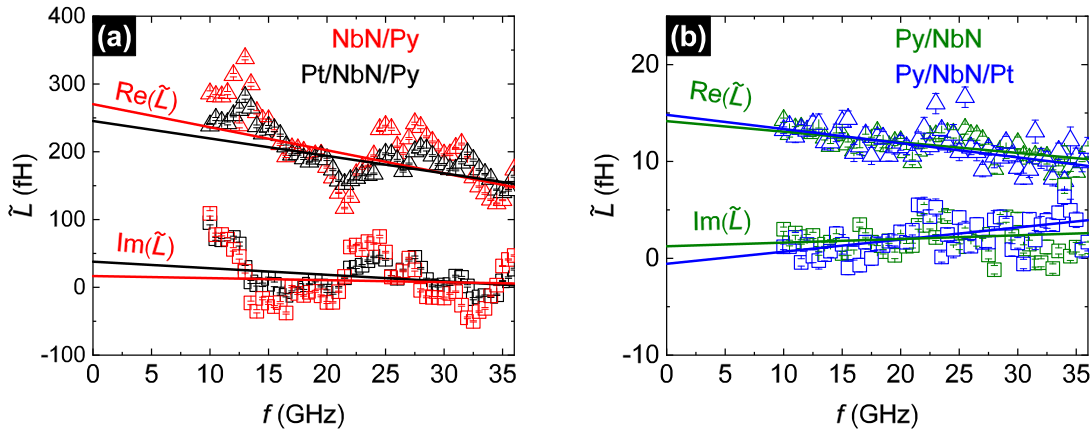


Figure 7.4: Real and imaginary part of the normalized inductance \tilde{L} for our sample series with $\text{sgn} = +1$ (a) and $\text{sgn} = -1$ (b) below the superconducting transition temperature $T \approx 0.5 \cdot T_C$. The apparent changes in inductive coupling strength L_0^{SC} have already been discussed in chapter 6. However, the slopes related to σ^{SOT} also exhibit dramatic alterations. In (a), the imaginary part of \tilde{L} does not intercept 0 at $f = 0$ Hz, which we attribute to Faraday currents in the superconductor.

We begin our discussion with the results in Fig. 7.4(a). Apart from the already discussed dramatic increase in inductive coupling strength \tilde{L}_0 due to superconducting image currents, we observe a rather noisy behaviour of \tilde{L} in both real and imaginary part. The oscillatory features are reproducible and stable with temperature, decaying only in magnitude \tilde{L}_0 for rising T . Superimposed on this pattern, we find a linear dependence on frequency. Notably, the results look suspiciously similar for both samples indicating that the presence of a Pt spin sink layer does not impact \tilde{L}_0 . The inverted samples in Fig. 7.4(b) for $\text{sgn} = -1$ also roughly maintain a linear scaling with f in the superconducting state. An attenuation of \tilde{L}_0 is caused by the screening of the oscillatory driving field \mathbf{h}_{rf} as established in section 6.2. Finally, we note that the results of \tilde{L} for the blue and green data points are very similar regardless of the inclusion of a Pt spin sink in the inverted samples.

In the following, we explain the modifications, that need to be made, to adapt the existing theory of Berger *et al.* for the application to superconducting materials instead of normal metals.

- First and foremost, we must account for the different strength of the driving field h_{rf} below T_C due to superconducting image currents. As h_{rf} scales quadratically with the magnitude of the inductive coupling strength, we normalize our results by multiplying the square root of the experimentally determined enhancement factor $\tilde{L}_0^{\text{SC}}/\tilde{L}_0$. The resulting inductive coupling to SC via SOT \tilde{L}_j^{SC} takes the form

$$\tilde{L}_j^{\text{SC}} = i \cdot \text{sgn} \cdot L_{12} \sqrt{\frac{\tilde{L}_0^{\text{SC}}}{\tilde{L}_0}} \eta(\delta_s, w_{\text{cc}}) \frac{\hbar\omega}{4M_s} \cdot \sigma^{\text{SOT}}. \quad (7.7)$$

- According to the results of Berger *et al.* [29], the contribution of Faraday currents to σ^{SOT} is reciprocally proportional to the effective surface impedance Z_{eff} , assumed to be constant with frequency. To account for superconductors we insert the SC-expression for Z_{eff} from Eq. (6.2) into the formula for σ_f^{F} derived by Berger *et al.*

$$\sigma_f^{\text{F}} = \frac{e\mu_0 M_s d_{\text{FM}}}{\hbar Z_{\text{eff}}(\omega)} = i \cdot \frac{eM_s d_{\text{FM}} \cdot d_{\text{SC}}}{\hbar\omega\lambda_L^2}. \quad (7.8)$$

The resulting σ_f^{F} scales inversely with ω and thus when plugging it into Eq. 7.7, its frequency dependence cancels out. The resulting contribution of Faraday currents to \tilde{L} takes the form

$$\tilde{L}_{\text{F}} = i \cdot \text{sgn} \cdot \frac{e d_{\text{FM}} d_{\text{SC}} L_{12}}{4\lambda_L^2} \sqrt{\frac{\tilde{L}_0^{\text{SC}}}{\tilde{L}_0}} \eta(\delta_s, w_{\text{cc}}). \quad (7.9)$$

Thus, Faraday currents create an offset \tilde{L}_{F} in the imaginary part below T_C . We do indeed observe a substantial y-axis intercept for the samples with $\text{sgn} = +1$ in Fig. 7.4(a). By plugging its magnitude into Eq. (7.9), we obtain another method to extract the London penetration depth λ_L . For the used samples it takes the values $\lambda_L = (1.9 \pm 0.3) \mu\text{m}$ [black data points] and $\lambda_L = (2.8 \pm 0.7) \mu\text{m}$ [red data points] respectively. These values are a factor 2 larger than those extracted by fitting $|S_{21}|$ and obviously a lot higher than literature values. As a concluding remark about this subject we mention the research of Silva *et al.* [97, 110] who measured the resistance ρ of superconducting thin films as function of frequency and observed similar effects.

We now briefly turn our attention towards the temperature dependence of the enhancement/attenuation factor $\tilde{L}_0^{\text{SC}}/\tilde{L}_0$ in the superconducting range. We proposed that the value of $\tilde{L}_0^{\text{SC}}/\tilde{L}_0$ is governed exclusively by superconducting image currents I_{SC} following Eq. (6.12) of the previous chapter 6. Furthermore, we discussed its relative magnitude and were able to show that the kinetic inductance L_{kin} only plays a minor role in our measurements by comparing the results for various superconducting materials. Thus, in the absence of a diverging contribution of L_{kin} , we expect the enhancement/attenuation effect of $\tilde{L}_0^{\text{SC}}/\tilde{L}_0$ to monotonically diminish with the superconducting image currents for rising T . To test this conjecture, we plot the measured enhancement/attenuation-factor as function

of reduced temperature in Fig. 7.5 both for the samples with $\text{sgn} = +1$ (a) and $\text{sgn} = -1$ (b).

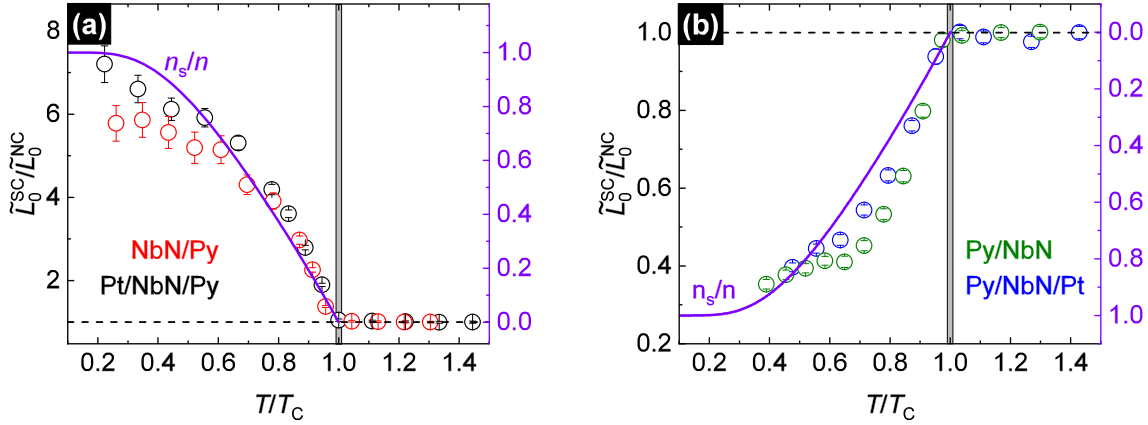


Figure 7.5: Enhancement and attenuation of the normalized inductive coupling strength $\tilde{L}_0^{\text{SC}}/\tilde{L}_0$ as function of the reduced temperature for samples with $\text{sgn} = +1$ (a) and $\text{sgn} = -1$ (b). The results are plotted together with the normalized BCS-superfluid density n_s/n .

The results shown in Fig. 7.5(a) and (b) are in agreement with our expectations. In Fig. 7.5(a), we observe the continuous reduction in $\tilde{L}_0^{\text{SC}}/\tilde{L}_0$ from roughly 7 to 1 with rising T . Likewise in the inverted samples shown in Fig. 7.5(b), the attenuating effect of the superconducting layer diminishes for elevated temperatures. Furthermore, we empirically found that we can describe the temperature dependence for all samples with that of the superfluid density from the ordinary BCS-theory n_s , indicated as purple lines in Fig. 7.5(a) and (b). While they match the general trend of our experimental results remarkably well, deviations are visible especially in vicinity of the transition temperature. Thus one may conclude that the theoretical calculations of Inoue *et al.* [19] from Fig. 3.5 for the spin susceptibility χ_s in the presence of impurity spin-orbit scattering would match our results better. However when applying this theory to our case we found that the used correction terms primarily reduce the magnitude of $n_s(T)$ and leave its temperature dependence mostly unchanged. Consequently, we attribute this deviation at temperatures close to T_C to a non negligible influence of the kinetic inductance L_{kin} , which is expected to increase dramatically with T . To comprehend how the superconducting image currents \mathbf{j}_{sc} are related to the superfluid density n_s , we use the naive expression

$$\mathbf{j}_{\text{sc}} = -2en_s(T) \cdot \mathbf{v}_s, \quad (7.10)$$

where e is the electron charge and \mathbf{v}_s is the velocity of the superconducting phase. Since these image currents give rise to a net driving field that quadratically scales with L_0 according to Eq. (6.13), we would expect the enhancement/attenuation to scale quadratically rather than linearly with n_s . However we have already established in chapter 6, that this theoretical model does not suffice to explain the physics in our samples. Hence we merely note a surprising correspondence between the temperature dependence of $\tilde{L}_0^{\text{SC}}/\tilde{L}_0$ and n_s , the origin of which is left up to debate for future studies on this subject. Nonetheless, this observation is a strong evidence that the superconducting image currents are responsible

for the enhancement/attenuation effects observed in the superconducting state.

Starting our discussion of the iSOT in the superconducting range with the damping-like torque, we plot σ_d^{SOT} as function of reduced temperature for both the samples with $\text{sgn} = +1$ and $\text{sgn} = -1$ in Fig. 7.6(a) and (b).

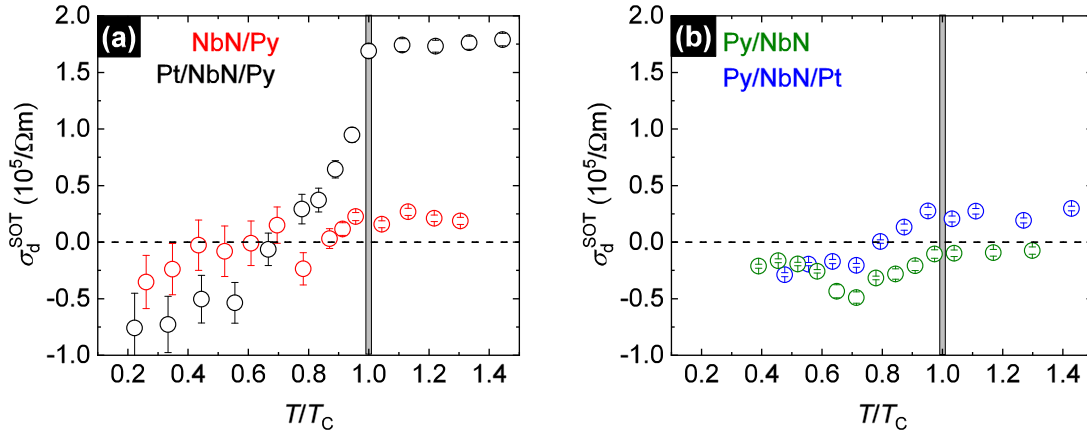


Figure 7.6: Extracted damping-like iSOT conductances σ_d^{SOT} plotted as a function of reduced temperature for the samples with $\text{sgn} = +1$ (a) and $\text{sgn} = -1$ (b). In the normal state, the samples including Pt exhibit a positive σ_d^{SOT} due to iSHE. Conversely below T_C , the results of samples with comparable stack sequence exhibit very similar and negative σ_d^{SOT} for both sgn irrespective of Pt sink layer.

Regarding the dampinglike iSOT in Fig. 7.6(a), we in particular observe a substantial σ_d^{SOT} in the Pt/NbN/Py-trilayer, while the red data points of the NbN/Py-bilayer exhibit smaller positive values. Below T_C the σ_d^{SOT} of both samples take small negative values decaying slightly further for lower T . The inverted samples in Fig. 7.6(b) exhibit a similar behaviour though greatly diminished in magnitude. The blue data points of the Py/NbN/Pt-trilayer assume only slight positive values in the normal state, while those of the Py/NbN-bilayer are negligible. In the superconducting state they also both exhibit slight negative values. The results of the normal state are easily understood. Both samples containing a Pt spin sink exhibit a positive σ_d^{SOT} , especially pronounced in the black data points of that with $\text{sgn} = +1$. We attribute this to a high transparency at its NbN/ $\text{Ni}_{80}\text{Fe}_{20}$ -interface. Below the superconducting transition temperatures, the values of σ_d^{SOT} drop into the negative range with or without Pt spin sink. This can either be attributed to the superconductor blocking spin currents or that it exhibits altered spin transport properties altogether. Following the former train of thought the remaining damping-like iSOT originates from spin pumping into either the Ta cap layer in Fig. 7.6(a) or the NbN bottom layer in Fig. 7.6(b). For (b), this explanation works well as the green data points of the sample without Pt exhibit no change below T_C apart from a cusp-like structure that is attributed to noisy fitting. However for the samples in (a), this theory no longer holds as for spin pumping into the Ta cap layer we would expect a minor positive σ_d^{SOT} as seen in the red data points above T_C . While the error bars here are substantial, the general trend in all our investigated samples was to exhibit negative σ_d^{SOT} when cooled below the superconducting transition temperature. Hence, we attribute this observation to altered properties of a spin current carried by BVQP in NbN. Hence our σ_d^{SOT} indicates the fraction of this BVQP spin

current that is converted into a charge current via the iSHE. This proposed Quasiparticle mediated inverse spin Hall effect [QMISHE] has been theoretically predicted in [111–114] and demonstrated experimentally to our knowledge only by Wakamura *et al.* [30] in a non-local spin injection device also using Permalloy as the ferromagnetic spin current injector and superconducting NbN as detector. Wakamura *et al.* found that below T_C the detected voltage signal due to the iSHE V_{iSHE} in the NbN wire is enhanced up to 2000 times compared to that in the normal state. This was attributed to a large spin Hall resistance ΔR_{SH} for temperatures substantially below the superconducting transition temperature, where the BVQP are greatly depleted [30, 115]. In our experiments, we are dealing with a system, where the equilibrium distribution of the BVQP governed by the Fermi distribution function $f_0(E_{\mathbf{k}}) = 1/(e^{E_{\mathbf{k}}/k_{\text{B}}T} + 1)$ is perturbed by a spin current \mathbf{j}_s injected from the adjacent FM layer. In a linear response approach, we can model the shift of the quasiparticle distribution $\delta f_{\mathbf{k},\sigma}$ as [111, 114]

$$\delta f_{\mathbf{k},\sigma} \approx -\sigma \left[\frac{\partial f_0(E_{\mathbf{k}})}{\partial E_{\mathbf{k}}} \right] \delta \mu_s. \quad (7.11)$$

Here $\delta \mu_s$ is the difference in chemical potential between spin up and spin down quasiparticles generated by the spin current \mathbf{j}_s . The shift in quasiparticle distribution is illustrated in Fig. 7.7(a) together with the Cooper-pair density as function of $\xi_{\mathbf{k}}$.

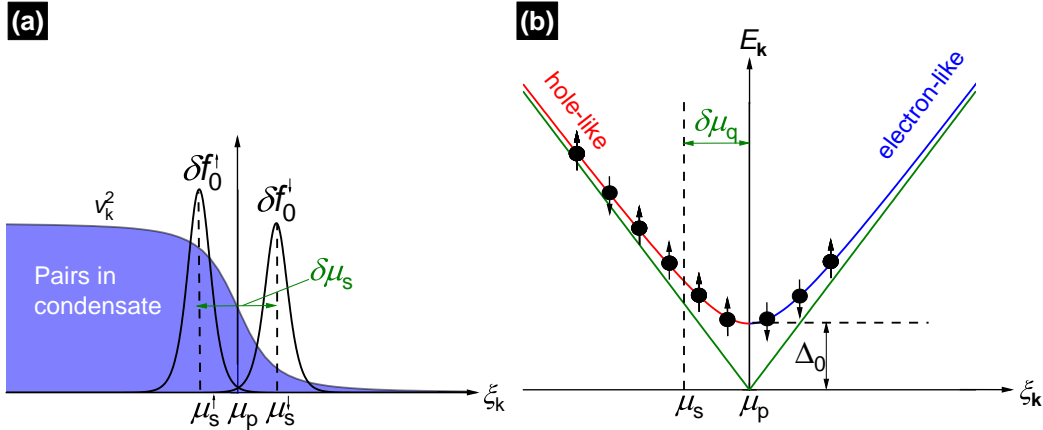


Figure 7.7: (a): Quasiparticle distribution functions $\delta f_{\mathbf{k}}^{\uparrow}$ and $\delta f_{\mathbf{k}}^{\downarrow}$ for spin up and spin down BVQP. The injection of a spin current generates a spin imbalance, which yields a splitting of the $\delta f_{\mathbf{k}}^i$ by $\delta \mu_s$. (b): Nonequilibrium distribution of quasiparticles on the excitation spectrum $E_{\mathbf{k}}$. Due to the spin imbalance, the QP excitation states are filled asymmetrically, which generates a relative shift $\delta \mu_q$ between the chemical potentials of the superfluid μ_p and quasiparticles μ_s . Illustration is based on Fig. 1. in [111].

From the quasiparticle excitation spectrum $E_{\mathbf{k}}$ in Fig. 7.7(b), we notice that different magnitudes of the nonequilibrium distribution of $\delta f_{\mathbf{k}}^i$ create an asymmetric filling of $E_{\mathbf{k}}$ with respect to $\xi_{\mathbf{k}}$ with more spin-up electrons in the hole-like branch than spin-down electrons in the electron-like one. Hence, the spin imbalance created by an injected spin current \mathbf{j}_s in turn gives rise to charge imbalance $\delta \mu_q$ between the Cooper-pair chemical potential μ_p and that of the BVQP, μ_s . Through this mechanism, a spin polarization of the BVQP condensate via the injection of a spin current entails a simultaneous charge polarization. Consequently, just like in the normal state, a BVQP spin current \mathbf{j}_s is partly converted into a transverse

BVQP charge current \mathbf{j}_q by means of spin-dependent scattering processes [111,112,114]. We are able to detect the flux generated by this dynamic \mathbf{j}_q as a change in inductive coupling strength between sample and CPW, whereas Wakamura *et al.* [30] measured the accumulation of electron- and holelike QP on opposite sides of his superconducting NbN antennas as a voltage signal .

We will not detail the involved calculations from Ref. [111] and merely enlist its most important results. For nonlocal devices the spin Hall resistance ΔR_{SH} generated by quasiparticles is proportional to both quasiparticle resistance ρ_{qp} and spin Hall angle Θ_{SH} . Following [30,115], the former can be obtained by normalizing the normal state resistance ρ_n to the amount of QP populated above the superconducting gap Δ . This share is governed by the Fermi distribution $f_0(\Delta(T))$

$$\rho_{\text{qp}} = \rho_n/[2f_0(\Delta(T))]. \quad (7.12)$$

From this expression the increase in ρ_{qp} for low temperatures immediately becomes apparent, as the Fermi distribution takes lower values for rising gap values $\Delta(T)$. The spin Hall angle Θ_{SH} comprises two contributions namely side jump scattering, which is independent of T and skew scattering rising with decreasing temperature proportional to $\chi_s(T)/2f_0(\Delta(T))$. As a result, in non-local spin current experiments, a dramatically enhanced spin Hall resistance ΔR_{SH} as observed by Wakamura *et al.* is in agreement with theoretical predictions.

In contrast, in our experiments we measure the flux generated by \mathbf{j}_q instead of ΔR_{SH} . For BVQP charge currents, the contributions of ρ_{qp} and Θ_{SH} counteract each other as the part of \mathbf{j}_q governed by Θ_{SH} is reduced by ρ_{qp} . The corresponding damping-like SOT conductivity is $\sigma_{\text{d}}^{\text{SOT}} \propto \Theta_{\text{SH}}/\rho_{\text{qp}}$ in accordance to [29]. Consequently its net temperature dependence is governed by the BVQP spin susceptibility $\chi_s(T)$. This result is intuitive as it relates the QP charge current generated by the QMiSHE to the density of the BVQP, $\chi_s(T)$. However, our results for $\sigma_{\text{d}}^{\text{SOT}}$ in Fig. 7.6 do not exhibit the expected freezeout with decreasing temperature, but rather increase in magnitude at lower temperatures. Here, it is important to keep in mind, that in the presence of impurity spin orbit scattering, a finite fraction of BVQP survives even at $T = 0$ K [19]. Hence, this share can generate a sizeable QMiSHE for low temperatures. Furthermore in the works of Takahashi *et al.* [111], the spin diffusion length λ_s has been assumed to be equal to that in the normal state. However, experiments in [116] revealed extremely long spin diffusion lengths in the μm -range of superconducting Al-wires in the presence of a Zeeman-field. An increasing λ_s for lower T would counterbalance the decreasing χ_s . Additionally, Ref. [112] hints at a continuous evolution of the QP charge polarization with temperature. In simple terms, the transport of a constant spin current \mathbf{j}_s with temperature requires a larger spin imbalance $\delta\mu_s$ for a lower fraction of BVQP. As previously established, a large $\delta\mu_s$ entails a strong charge imbalance $\delta\mu_q$ in the filling of the QP excitation spectrum. To our knowledge this continuous evolution of the BVQP charge polarization with temperature has so far not been taken into account. We note that the similarity in $\sigma_{\text{d}}^{\text{SOT}}$ throughout our samples in Fig. 7.6 suggests that the BVQP-mediated spin-current can not enter the opposite Pt layer.

Summarizing, by using existing theoretical models for the quasiparticle-mediated inverse

spin Hall effect [QMISHE], we can satisfactorily explain our results for the damping-like SOT σ_d^{SOT} below T_C . Deviations in our quantitative magnitude of this effect from results of Wakamura *et al.* originate from the different applied detection methods.

It is worth mentioning that in contrast to previous studies for the determination of the spin Hall angle in superconductors [30,31], our measurement technique measures the currents rather than voltage V_{SH} induced by the inverse spin Hall effect. In his research Wakamura *et al.* [30] was able to demonstrate that the observed V_{SH} in his devices was dependent on the distance d_{SH} between the voltage probes. He attributed this phenomenon to the relaxation of the quasiparticle current into the Cooper-pair condensate within a characteristic length scale that he named the charge imbalance length λ_q . As a consequence, the magnitude of the detected V_{SH} depends on d_{SH} , which explains why in Ref. [31] no iSHE was detected. Moreover, the charge imbalance length λ_q decreases with rising temperature and thus V_{SH} in [30] exhibits the opposite dependence on T than theoretically predicted. Our measurements detect the integrated flux of charge currents induced via iSHE and are hence independent of λ_Q . This is why we are able to observe the theoretically predicted scaling of σ_{SH} with T . Summarizing, our measurement technique circumnavigates the problems of voltage-based methods for the determination of Θ_{SH} for being exclusively sensitive to the current generated via iSHE.

Finally, we turn our attention towards the arguably most peculiar results in Fig. 7.4, the unexpected change in the slope of $\text{Re}(\tilde{L})$ below T_C . While changes in $\text{Im}(\tilde{L})$ were expected for the altered spin pumping properties in superconductors, this finding suggests the manifestation of an unexpected current-flux due to the inverse Rashba-Edelstein effect at the SC/FM-interface. For comparison we plot the field-like SOT conductivities ($\sigma_f^{\text{SOT}} - \sigma_f^{\text{F}}$) as function of reduced temperature for samples with $\text{sgn} = +1$ (a), (c) and $\text{sgn} = -1$ (b), (d) separately in Fig. 7.6. As previously established, the Faraday currents contribute to σ^{SOT} only in the normal state and we consequently highlight the corresponding temperature range with an orange background.

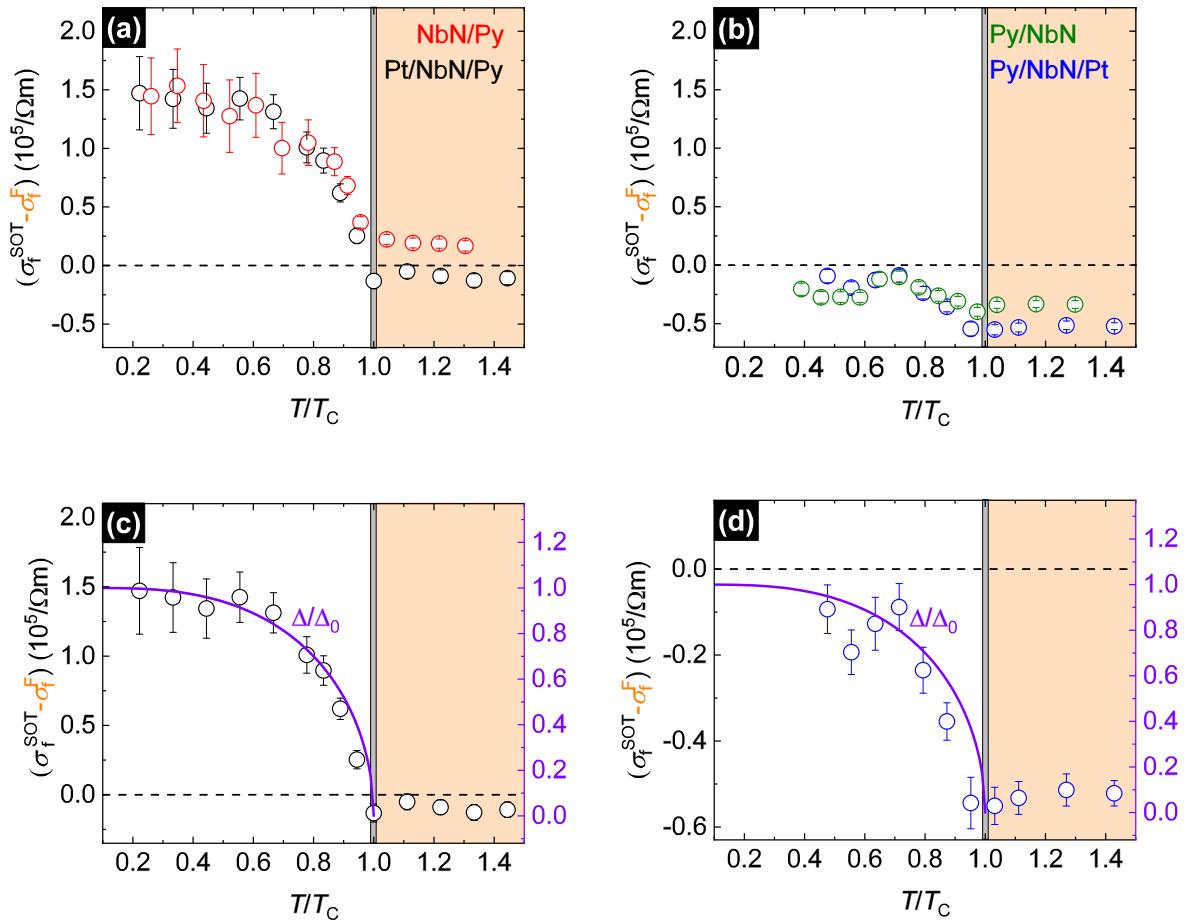


Figure 7.8: Extracted field-like iSOT conductance $(\sigma_f^{\text{SOT}} - \sigma_f^{\text{F}})$ plotted as a function of reduced temperature for the samples with $\text{sgn} = +1$ (a) and $\text{sgn} = -1$ (b). From our calculations, we deduce that σ_f^{F} creates an offset in $\text{Im}(\tilde{L})$ below T_C and only contributes to σ_f above T_C . We marked the corresponding temperature range with an orange background. For both stack sequences we plot the temperature dependence of one sample together with the normalized superconducting gap parameter Δ in (c) and (d). They match astonishingly good indicating a Rashba-like confinement of electrons at the SC/FM-interface due to the superconducting gap Δ .

We begin our discussion for the field-like iSOT below T_C with the resulting $(\sigma_f^{\text{SOT}} - \sigma_f^{\text{F}})$ of the normal samples in Fig. 7.8(a). In the normal state, we detect negligible values for the Pt/NbN/Py-trilayer [black data points] and a minor positive $(\sigma_f^{\text{SOT}} - \sigma_f^{\text{F}})$ for the NbN/Py-bilayer [red data points]. Below T_C , both samples exhibit a large positive $(\sigma_f^{\text{SOT}} - \sigma_f^{\text{F}})$ that gradually increases for decreasing T . Here the data for both samples coincide astonishingly well irrespective of Pt seedlayer. As previously established, Faraday currents do not contribute to the slope of $\text{Re}(\tilde{L})$ in the superconducting state. Therefore we attribute its large value entirely to the inverse Rashba-Edelstein effect denoted by σ_f^{SOT} . Moving on to the results in (b), we observe minor negative values in the normalconducting range. Just like in (a), the blue data points of the inverted Py/NbN/Pt-trilayer are slightly lower than the green ones of the Py/NbN-bilayer. Hence we infer that this difference is generated by Faraday currents in the Pt layer. For $T < T_C$, the data points of both samples gradually approach zero with decreasing temperatures. While the general trend of $(\sigma_f^{\text{SOT}} - \sigma_f^{\text{F}})$ here is the same as for the normal samples, the magnitude of the changes below T_C is a

lot lower. As demonstrated in Fig. 7.8(c) the results can be matched well to the temperature dependence of the superconducting gap $\Delta(T)$ following the BCS theory. While we do by no means understand this peculiar result from a quantum mechanical standpoint, it is nonetheless worth mentioning that this correspondence hints at a Rashba-like confinement of electrons by the potential $\Delta(T)$ at the FM/SC-interface. The reason for this bold claim is simply that σ_f^{SOT} scales linearly with the Rashba-parameter α_R , which is in turn proportional to the gradient of the confining potential $\nabla V = \Delta(T)$ [53, 107]. The gap Δ is suppressed at the FM/SC-interface due to the proximity effect. For the sake of simplicity, we assume that it increases linearly inside the NbN layer $\Delta(z, T) = \Delta_0(T)z/\xi_0$. In this simple picture, the superconducting gap does indeed define the temperature dependence of σ_f^{SOT} . Moving on to the results in Fig. 7.8 (b), we observe a decrease in σ_f^{SOT} , which can be easily understood under the premise that the bottom NbN/Permalloy interface exhibits a substantial inverse Rashba-Edelstein effect in the normalconducting state, while the upper interface does not contribute. Below T_C , a Rashba-like confinement of electrons manifests at the upper FM/SC-interface and gives rise to an additional contribution to σ_f^{SOT} . The magnitude of this contribution is lower than that in Fig. 7.8 (a), which we attribute to the reduced interface quality. To test this assumption we again plot σ_f^{SOT} for one sample together with the gap parameter $\Delta(T)$ as a function of reduced temperature in Fig. 7.8(d). Again we observe a very good agreement between superconducting gap $\Delta(T)$ and σ_f^{SOT} . The field of superconducting spintronics is still in a very early phase and we were not able to find existing literature nor derive a theoretical model explaining this manifestation of σ_f^{SOT} in superconductor/ferromagnet-heterostructures. Thus, we can only provide an overview over the scarce research we were able to find on this subject.

- On the experimental side a Rashba-interaction in SC/FM-interfaces has to our knowledge been experimentally observed only by Nadj-Perge *et al.* [117] for 1D-Fe-chains deposited on top of superconducting Pb. They attributed it to the strong spin-orbit interaction of the heavy metal Pb.
- Theoretical research on this topic by Bobovka *et al.* [118] revealed that supercurrents injected into ferromagnetic layers can generate field-like spin-orbit torques. Conversely, Mironov *et al.* showed that the presence of Rashba-spin-orbit interaction at SC/FM-interfaces should give rise to the flux of a spontaneous charge current flowing along the interface [119, 120]. Hence from a theoretical standpoint the Onsager reciprocity of currents giving rise to SOT and in turn SOT inducing currents also holds true in these systems. Hence, the used method of data analysis should be valid.

We conclude by noting that the observed field-like SOT σ_f^{SOT} in the superconducting phase are quite substantial, as they are of the same magnitude as the damping-like SOT σ_d^{SOT} observed in Py/Pt-structures by [81]. The switching of the out-of-plane magnetization in a ferromagnetic layer by utilizing the damping-like SHE has already been demonstrated by Miron *et al.* [102]. Following this approach, we propose that our observed field-like spin orbit torque in SC/FM-interfaces can likewise be utilized for the switching of an in-plane \mathbf{M} by applying substantial currents in the superconducting layer. As these currents flow without dissipation, this approach might reduce the heating effects commonly found in spintronics devices. We will discuss this prospect in depth in chapter 9, where we outline

our experimental result for a device fabricated to probe this dissipationless switching via GMR.

7.3 Concluding remarks

We conclude this chapter by illustrating and discussing some of our additional results in the field of spin-orbit torques in superconducting materials.

In the course of this master's thesis we have been exclusively investigating the effects of superconductivity in SC/FM-bilayers using different stack sequences and brought them into contact to HM layers to investigate spin pumping effects. In literature, however, it is more common to use symmetric SC/FM/SC-sandwiches [23, 28, 89]. Yet in our experiments we realized that the superconducting transition temperature varies drastically with the used seedlayer to grow NbN on. Particularly when grown on Permalloy, T_C was reduced by up to 4 K. As a result, a major shortcoming of existing literature is the fact that the instantaneous transition of both SC layers in unison at the same temperature is taken for granted and hence they merely rely on transport measurements to determine T_C . Thus, alterations in the magnetization dynamics parameters observed in these papers can in reality not exclusively be attributed to altered transport properties of superconductors but might just as well originate from noisy fitting, when the opposite layer transitions into superconductivity. Moreover, superconducting image currents are present in both SC layers and impact the inductive coupling strength L_0 . Here, it is not certain whether this leads to an attenuation or enhancement of the net L_0 . Furthermore, their different transition temperatures might induce a complicated behaviour of the corresponding FMR amplitude A with temperature, which can also give rise to features in the magnetization dynamics parameters through noisy fitting. Our inductive spin orbit torque analysis procedure is sensitive to L_0 and hence we can determine the transition temperatures of both SC layers simultaneously in our samples. To probe the inductive coupling in symmetric SC/FM/SC-structures, we fabricated a sample comprising 16 nm NbN/6 nm Ni₈₀Fe₂₀/ 16 nm NbN/ 2 nm AlO_x. Its resulting inductive coupling strength in the superconducting range normalized by that of the normal state is plotted in Fig. 7.9(a) as a function of T/T_C . Here T_C denotes the higher transition temperature of the bottom NbN layer.

The change in inductive coupling strength exhibits a cusp-like shape and is enhanced by a factor of merely 1.3 when compared to the normalconducting range. We can match its behaviour well by assuming two separate condensate densities n_s^{top} and n_s^{bottom} , where we used the analytic expression $n_s^i \propto 1 - (T/T_C^i)^4$ for the sake of simplicity. The extracted transition temperatures are $T_C^{\text{top}} = 7.5$ K and $T_C^{\text{bottom}} = 8$ K. These results reveal that the transition temperatures of top and bottom superconducting layer deviate only slightly and that the change in FMR amplitude is also rather small in these structures. Fortunately this suggests that symmetric SC/FM/SC-sandwich samples can be reliably used to investigate changes in the magnetization dynamics parameters, as their inductive coupling strength L_0 appears to remain roughly constant with temperature and the T_C of the two layers are in close proximity.

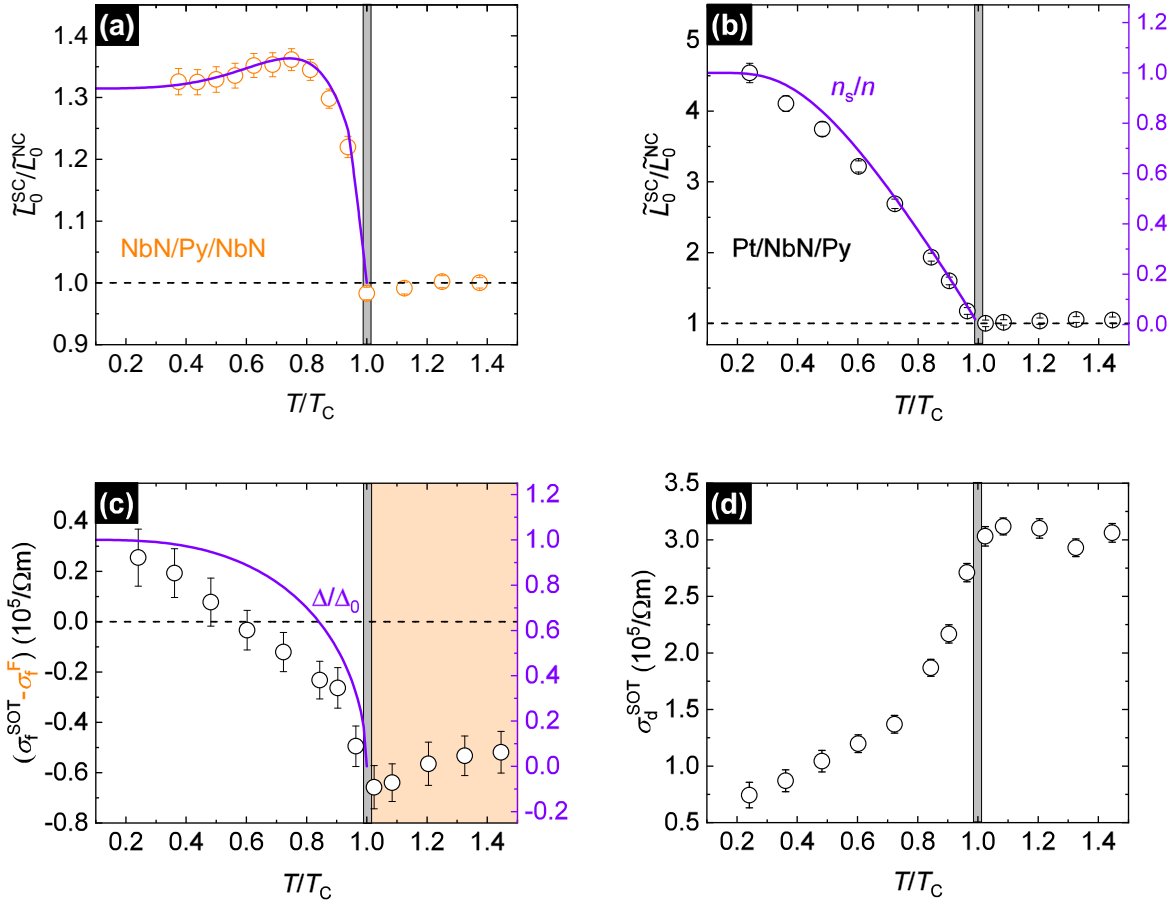


Figure 7.9: (a): Change in normalized inductive coupling strength in the superconducting phase $\tilde{L}_0^{\text{SC}}/\tilde{L}_0$ as function of the reduced temperature for the symmetric SC/FM/SC-sample. From the matching curve using two separate condensate densities n_s^{top} and n_s^{bottom} , we can simultaneously extract the T_C of both superconducting layers. The extracted transition temperatures are $T_C^{\text{top}} = 7.5$ K and $T_C^{\text{bottom}} = 8.0$ K. (b): Enhancement factor $\tilde{L}_0^{\text{SC}}/\tilde{L}_0$ of NbN/Py-bilayer with $\text{sgn} = +1$ grown on a Pt (5 nm) spin sink as function of reduced temperature together with superfluid condensate density n_{BCS} extracted from BBFMR results in oop-geometry. The temperature-dependence of field- and damping-like SOT ($\sigma_f^{\text{SOT}} - \sigma_f^{\text{F}}$) and σ_d^{SOT} in this configuration are shown in (c) and (d) respectively. The former is plotted together with the superconducting gap parameter Δ .

Finally, we note that the lower saturation magnetization of $\mu_0 M_s = 1$ T in Permalloy additionally permitted the performance of BBFMR in oop-geometry in the CHAOS cryostat. Using this configuration, the superconducting NbN layer responds to the perpendicular magnetic field by letting it penetrate in the form of normalconducting vortices. Hence, we expect changes in both the inductive coupling strength and iSOT when compared to ip-geometry. Since the recording of an entire temperature series is rather time consuming we decided to perform oop-BBFMR at varying T for only one sample namely the Pt/NbN/Ni₈₀Fe₂₀-trilayer with $\text{sgn} = +1$ and a 5 nm Pt spin sink layer. The results of these measurements are shown in Fig. 7.9(b)-(d). We start with the discussion of the inductive coupling strength $\tilde{L}_0^{\text{SC}}/\tilde{L}_0$ in (b). The formation of vortices with normal cores depletes the superconducting fluid density n_s and hence we observe an enhancement factor of only up to 5 as opposed to 7 in ip-geometry. For both field- and damping-like iSOT in 7.9(c) and

(d), we observe the same qualitative changes in the superconducting range as in Fig. 7.6 and 7.4. Merely their quantitative magnitude seems to be reduced in the presence of vortices. Notably, the matching of field-like iSOT with the superconducting gap parameter Δ works discernibly worse, which hints to vortices present at the SC/FM-interface depleting the 2DEG confined by the potential Δ . In this picture, we essentially view the vortices as leaks through which electrons can enter the SC layer. The behaviour of σ_d^{SOT} supports this model as, while being reduced in the superconducting range, it still exhibits a large positive value that can only be explained by substantial spin pumping into the Pt layer. We note that the values of σ_d^{SOT} in the normal range for ip- and oop-geometry deviate in magnitude. This effect is attributed to a difference in spin pumping for different geometries and has also been observed as a varying α_{SP} in [36], though its precise origin remains unknown. This phenomenon is called spin pumping anisotropy.

To summarize, we observe the same qualitative changes in both the inductive coupling strength and iSOT as detected in ip-geometry, but their respective quantitative values are reduced for the presence of vortices with normal cores in this geometry.

8 Summary

In this thesis, the magnetization dynamics of ferromagnetic metals in direct contact to superconducting materials have been investigated at cryogenic temperatures. To this end, we used the Superbowl sputtering machine for the in-situ growth of FM/SC-heterostructures. The blanketed film was mounted flip-chip onto a coplanar waveguide at the end of a dipstick and placed into the CHAOS cryostat which provides an environment where both temperature and external magnetic field can be varied in a vast range. For its characterization a ferromagnetic resonance technique using a coplanar waveguide and a vector network analyzer [VNA] has been used. The first experiments were dedicated to the detection of a peaklike structure in the Gilbert damping α theoretically predicted by Ref. [19] as function of temperature in the FM $\text{Co}_{25}\text{Fe}_{75}$ adjacent to the superconductor NbN. Furthermore we discussed how the exotic properties of superconductivity like perfect conductance or the screening of external fields via image currents additionally impact further measurement quantities in VNA-based broadband FMR. In particular, we observed that the latter can drastically impact the measured amplitude of the FMR resonances and derived a simplified theoretical model to explain and quantify this effect. Thereafter, we employed an amplitude sensitive data analysis procedure developed by Berger *et al.* [29] to analyse spin-orbit torques in our SC/FM-structures in both the normal- and in the superconducting state for the first time. In the latter we outlined how to modify the existing theory to account for the exotic properties of superconductors and altered inductive coupling \tilde{L}_0 . Finally, we showed both field- and damping-like iSOT as a function of temperature and discussed their dramatic changes below T_C . With our novel analysis protocol, we were able to relate the reduction in the damping-like iSOT parameter to the freeze-out of superconducting particles mediating the spin current. This finding matches with previous results [23, 89], as a freeze-out behaviour is also evident in the well-established Gilbert damping parameter α as function of temperature. Moreover, we report the discovery of a previously unknown Rashba-SOT at the SC/FM-interface, which might be employed for the dissipationless in-plane switching of the magnetization \mathbf{M} in a FM layer. Our findings reveal symmetry and strength of iSOTs at the SC/FM interface and provide guidance for future superconducting spintronics devices.

8.1 Superconducting coherence peak in NbN/ $\text{Co}_{25}\text{Fe}_{75}$ -multilayers

In chapter 5 we outlined our efforts to detect a peak-like structure in the Gilbert damping of NbN/ $\text{Co}_{25}\text{Fe}_{75}$ -multilayers as a function of temperature, which has been predicted by Refs. [19, 20]. In order to compare our results to theory, we had to determine the net contribution of spin pumping α_{SP} to the total α . Thus, we conducted two ip-BBFMR layer thickness series at room temperatures for NbN (20 nm)/ $\text{Co}_{25}\text{Fe}_{75}$ (d_{FM})/ Ta (2 nm) grown with and without a Pt (5 nm) spin sink seedlayer for comparison. By fitting the Gilbert damping α as a function of the reciprocal layer thickness of the ferromagnetic layer d_{FM} , we were able to extract values for α_{SP} , that matched well with previous studies on $\text{Co}_{25}\text{Fe}_{75}$ [36, 80]. Thereafter, we verified that these results are also valid at cryogenic temperatures by illustrating the negligible changes in the magnetization dynamics parameters for two NbN/ $\text{Co}_{25}\text{Fe}_{75}$ -bilayers with and without a Pt spin sink seedlayer recorded over

a broad temperature range reaching from RT to slightly above T_C . We presented the ip-BBFMR results for these two samples below T_C in the CHAOS cryostat. Most importantly, we indeed detected a small, but finite coherence peak in α_{SP} of about 5% magnitude within the predicted temperature region $[0.7-0.8]T_C$ in both samples, which is significantly lower than theoretical predictions in [19]. This discrepancy was attributed to the suppression of superconductivity at the SC/FM-interface, when SC charge carriers are able to enter the ferromagnetic metal. Furthermore, the absence of such a peak-like structure in samples containing Nb as superconducting layer indicated that a resilient SC is required to observe this phenomenon.

8.2 Manifestations of superconductivity in VNA-based BBFMR

The magnetization dynamics parameters of the FM layer are not the only measurement quantities to exhibit changes, when the adjacent layer transitions into superconductivity. The perfect conductance of SC changes the sample's surface impedance Z_{eff} and consequently the magnitude of the complex transmission parameter $|S_{21}|$. We illustrated this effect and used an existing formula for $|S_{21}(Z_{\text{eff}})|$ derived by Schmidt *et al.* [95] to fit the recorded behaviour of $|S_{21}|$ as a function of temperature. With this expression we were able to simultaneously obtain estimates for both T_C and the London penetration depth λ_L . The larger values $\lambda_L = [1-2] \mu\text{m}$ in the latter, when compared to literature values, are attributed to impurities in our thin film superconductors. Moreover, the expulsion of oscillatory magnetic driving fields \mathbf{h}_{rf} in the superconducting layer can either enhance or reduce the sample's inductive coupling strength L_0 and consequently the observed FMR amplitude. In our experiments with NbN/Ni₈₀Fe₂₀-heterostructures we observed both an enhancement by a factor of 7- and an attenuation by a factor of 0.4 as in the normal state depending on the used stack sequence. In the enhancement case, the Permalloy was sandwiched between SC and CPW, effectively being driven from both sides, while in the attenuation case the superconductor was grown on top of the FM layer and attenuated \mathbf{h}_{rf} leading to a reduction of L_0 . We derived a simple theoretical model to describe this effect and were able to reproduce the observed behaviour by varying the impact of the superconducting kinetic inductance L_{kin} . Finally, we discussed how these parameters vary depending on the used superconducting material. Here, we found that the fitted London penetration depth λ_L indeed changed as expected with the used SC, while the enhancement factor L_0^{SC}/L_0 remained nearly unchanged despite expectations of a varying L_{kin} .

8.3 Inductive detection of Spin-Orbit Torques in SC/FM heterostructures

In chapter 7 we aimed to detect and discuss possible changes in the field- and damping-like SOT, which can be quantified using an FMR-amplitude sensitive data procedure derived by Berger *et al.* [29]. Within the course of this chapter we showed and compared the results of BBFMR for 4 different NbN/Ni₈₀Fe₂₀-samples investigated in the temperature range from 3K to 300K. We examined how the inclusion of a 5 nm Pt spin sink in two of these samples would impact in particular the damping-like SOT related to the spin Hall effect. We began this chapter by illustrating and discussing the magnetization dynamics parameters of these samples in the temperature range around T_C and discussed differences and similarities to

the results from those in chapter 5 for $\text{Co}_{25}\text{Fe}_{75}$. For these four samples we found that their effective magnetization $\mu_0 M_{\text{eff}}$ and g -factor were comparable. For samples with $\text{sgn} = +1$ [Substrate/SC/FM], we observed a gradual reduction of α in the superconducting range, while simultaneously the inhomogeneous line broadening $\mu_0 H_{\text{inh}}$ was rising with decreasing T . Conversely, for the ones with inverted stack sequence $\text{sgn} = -1$ [Substrate/FM/SC] we observed a peak-like structure in α , mirrored in the behaviour of $\mu_0 H_{\text{inh}}$. We attributed its origin to the noisy fitting procedure in these samples below T_C due to the low FMR amplitude. Afterwards we turned our attention to the iSOT and used the amplitude A and phase ϕ from the fits of the BBFMR results to determine the normalized inductance \tilde{L} . To quantify the magnitude of spin orbit torques, the so-called iSOT conductivities ($\sigma_{\text{f}}^{\text{SOT}} - \sigma_{\text{f}}^{\text{F}}$) and $\sigma_{\text{d}}^{\text{SOT}}$ can be extracted from its slope in the real and imaginary part. In similar fashion to the results of chapter 5 we showed that the extracted σ^{SOT} exhibit only minor changes when cooling the samples down to cryogenic temperatures slightly above T_C and thereby demonstrated that this method of quantifying SOT is also valid for low temperatures. We then displayed results for \tilde{L} below T_C and discussed how the method in [29] has to be adapted for SC/FM-heterostructures to investigate iSOT in SC/FM-heterostructures for the first time. We showed that the dramatic changes in our inductive coupling strength \tilde{L}_0 in the superconducting state could be attributed entirely to image currents in the superconductor by matching its temperature dependence to the superfluid density n_s from BCS-theory. Starting our discussion of the iSOT with the dampinglike $\sigma_{\text{d}}^{\text{SOT}}$, we detected a dramatic change in $\sigma_{\text{d}}^{\text{SOT}}$ particularly in the samples with $\text{sgn} = +1$, where irrespective of the presence of spin pumping into Pt above T_C , it decreases to a minor negative value in the superconducting temperature range. To the best of our knowledge this result can only be explained by spin transport into the NbN-layer via BVQP. This so-called quasiparticle mediated inverse spin Hall effect [QMISHE] has previously been detected by Wakamura *et al.* [30]. We modified theoretical calculations in [111, 112, 114] for our used current-sensitive measurement method and found that $\sigma_{\text{d}}^{\text{SOT}}$ should decrease with temperature due to the freezing out of BVQP, which we did not observe in our measurements. Based on the calculations of Inoue *et al.* [19] however, we argue that a finite fraction of BVQP can manifest even at $T = 0$ K to carry spin currents with exceptionally long spin diffusion lengths [116]. The similarity in the temperature-dependent behaviour of both our extracted $\sigma_{\text{d}}^{\text{SOT}}$ and the Gilbert damping α reveal, that our inductive analysis approach provides a new way to probe spin pumping into superconductors. Our arguably most peculiar result was the detection of substantial field-like iSOT ($\sigma_{\text{f}}^{\text{SOT}} - \sigma_{\text{f}}^{\text{F}}$) via the inverse Rashba-Edelstein effect below T_C . Following a linear approximation for $\Delta(z, T)$, as the gap is reduced at the SC/FM-interface due to the proximity effect, we attributed this result to the confinement of electrons by the potential well of the superconducting gap Δ . As we could not find a theoretical paper explaining this finding at the date this thesis was written, we merely outlined existing experimental and theoretical works in this field. Notably, an Onsager reciprocity between superconducting image currents and Rashba-spin-orbit interaction can be deduced from Refs. [118–120]. Regarding future spintronics devices, the discovery of this field-like iSOT might pave the way towards the dissipationless switching of the magnetization \mathbf{M} of ferromagnetic layers. We concluded our experimental results with the discussion of additional findings for a symmetric SC/FM/SC-sample and for applying out-of plane

geometry. For the former experiment, we were able to extract the transition temperatures T_C for both superconducting layers simultaneously with our inductive analysis technique. We found that they do not transition into superconductivity in unison at the same temperature and hence a mere transport measurement as conducted in previous studies [23,28,89] is not sufficient to characterize the superconducting properties in these samples. Finally, we compared the iSOT in ip- and oop-geometry for one of our 4 samples and found that both \tilde{L}_0 and the σ^{SOT} exhibit the same qualitative changes in the superconducting range merely being diminished in magnitude due the presence of Abrikosov-vortices in the oop-case.

9 Outlook

The field of superconducting spintronics is still in a very early stage and despite manifold promising theoretical propositions and fascinating experimental results, the quantum-mechanical mechanisms taking place at the interface between superconductors and ferromagnets are as of yet not fully understood. Its arguably most exciting prospect is the dissipationless switching of the magnetization \mathbf{M} in an adjacent FM and spin transport to reduce heating effects in existing data storage and magnetic random access memory devices. Promising results in this field for FM/SC-heterostructures are the detection of giant spin Hall angles [30], the potential discovery of spin-triplett Cooper-pairs [22, 23] as well as the generation field-like spin-orbit torques [118]. In the course of this master's thesis we aimed at detecting changes of the spin-pumping properties of a FM adjacent to a thin film superconductor. By conducting VNA-based BBFMR at cryogenic temperatures we were indeed able to discover several theoretically proposed effects in our SC/FM-samples. First of all, as suggested in [19] we did detect a small coherence peak of about 5% in our NbN/Co₂₅Fe₇₅-thin films but not in those comprising Permalloy instead. We attributed this to its larger linewidth ΔH overshadowing an enlarged spin pumping contributions. However, we should investigate several other FMs, favourably with low damping to verify this assumption. Furthermore, we aim to extend our research to include ferromagnetic insulators like YIG or GdN instead of metals as the coherence peak magnitude is expected to be more pronounced when superconducting charge carriers are unable to enter the ferromagnet [19]. Both the height and shape of the coherence peak allow to probe the dynamic spin susceptibility of superconducting thin films potentially with a better signal-to-noise ratio than in the common NMR-measurements of the spin-relaxation rates in bulk SC [121, 122]. Additionally, our discoveries from chapter 6 offer manifold future application. Firstly, we were able to fit $|S_{21}|$ as function of temperature to extract the superconducting London penetration depth λ_L . This method to quantify T_C requires no bonding for transport measurement leaving the thin film entirely unharmed. Moreover, we found that λ_L does indeed vary with the used superconducting material indicating the validity of our approach. Like most methods for the determination of λ_L , we are particularly sensitive to its changes with temperature rather than its absolute magnitude. Hence, as we use merely estimates for phase velocity v_{ph} , thickness of the superconductor d_{SC} and $Z_0 = 50 \Omega$, we observed the right temperature dependence, but too high values for λ_L . To reliably use our approach for the precise quantification of the London penetration depth we therefore require both precise values for these constants and more sophisticated expressions for the superconducting surface impedance $Z_{eff}(\omega)$ as provided for example in [97, 123]. The enhancement of inductive coupling between sample and CPW, \tilde{L}_0 , in samples comprising a highly conductive buffer layer has applications far beyond the field of superconducting spintronics as it improves the signal-to-noise ratio in BBFMR to enable the detection of signals that were previously too small to detect. Just one possible use is the measurement of spin pumping in NM/FM-samples using thinner ferromagnetic metals, where its contribution to the Gilbert damping α_{SP} is more pronounced.

Finally, our method used to detect and quantify spin-orbit torques in SC/FM-heterostructures offers the intriguing possibility to study both superconducting spin Hall effects and the

generation of supercurrents via the Rashba-Edelstein effect simultaneously as field- and damping-like effects are phase shifted by 90° with respect to each other. Moreover, as previously established its sensitivity to currents rather than voltages allows us to quantify the QMiSHE without having to take the charge imbalance length λ_Q into account. This is a major advantage when compared to existing studies [30,31] of superconducting spin Hall effects using non-local devices with superconducting strips.

Towards the goal of dissipationless switching, the substantial field-like SOT σ_f^{SOT} detected in our measurements offers a new and to our knowledge previously unknown possibility in the application of substantial superconducting currents to control the in-plane magnetization \mathbf{M} of a FM layer via the Rashba-Edelstein effect. Our detected σ_f^{SOT} is of the same magnitude as the damping-like SOT σ_d^{SOT} generated by the iSHE by Py/Pt-bilayers in [81]. The switching of an out-of-plane magnetization in a ferromagnetic layer by utilizing the damping-like SHE has already been demonstrated by Miron *et al.* [102]. Consequently, we propose that likewise we can utilize our observed field-like spin orbit torque in SC/FM-interfaces to switch the orientation of \mathbf{M} in an in-plane magnetized sample. However, a major problem is the competition between the high current densities required to generate a sufficient torque to affect \mathbf{M} and the limited superconducting critical current density j_C . Naive estimates suggested that both should be roughly of the same order of magnitude [102,124,125].

To probe this exciting possibility we grew a ferromagnetic spin valve structure on top of a superconducting bar to detect the switching of \mathbf{M} via the GMR effect in CPP-geometry. In Fig. 9.1 we illustrate the pattern of these GMR spinvalves as well as our used measurement geometry. The fabrication process for these spinvalve is described in the Appendix A.2.

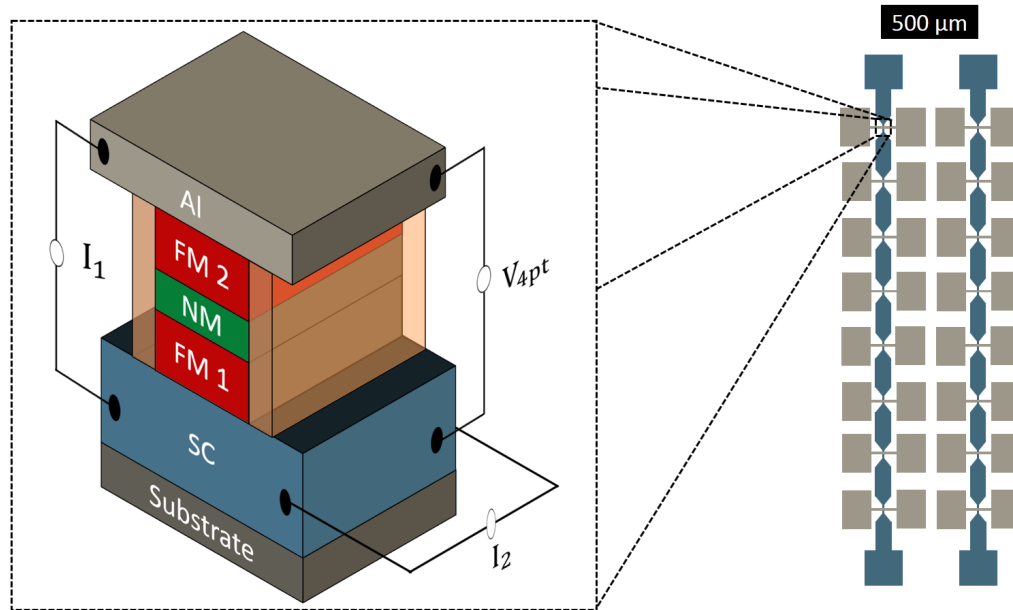


Figure 9.1: Example of the pattern for the fabrication of superconducting GMR spin valve structures. Vertical bars of the SC are topped with a GMR stack, which are contacted via Al pads. To achieve high current densities, the superconducting strip underneath the stack exhibits constriction. We apply a large in-plane current I_2 within the superconducting NbN that should exert a torque on the magnetization of the FM1-layer. To probe this effect, an additional small perpendicular current I_1 is driven through the GMR-stack and we simultaneously measure its voltage drop V_{4pt} . Here the used SC layer is NbN (30 nm) and the GMR stack comprises FM 1= Py (6 nm), NM= Cu (3 nm) an FM 2= Fe (10 nm) respectively. Furthermore we grew a thin conducting Pt capping layer on FM 2 to prevent oxidization, which is not shown for the sake of clarity.

Theses samples were then mounted on a dipstick and placed inside the MORIA-cryostat to record the stack's resistance for varying temperatures and magnetic fields. We applied a small current I_1 through the spinvalve while driving a large current I_2 in the superconducting bar to generate a torque on the magnetization of FM 1. To probe the GMR effect we measured the parallel voltage V_{4pt} in a 4 point measurement. Unfortunately, in our measurements we were not able to generate a sufficient current density in DC-operation as the superconducting NbN-layer transitioned at $j_C = 3 \times 10^9 \text{ A/m}^2$. This result is about an order of magnitude lower than literature results suggest [124, 125] indicating that j_C is also affected by the presence of a FM. By applying current pulses of $\Delta t = 110 \mu\text{s}$ with a 6221 AC and DC current source, we could increase it to merely $j_C = 5 \times 10^9 \text{ A/m}^2$. We found that these values were too low to impact the magnetization \mathbf{M} in FM 1. However, we did unexpectedly detect changes in the GMR-effect itself below the transition temperature. In Fig. 9.2(a) we show the magnetoresistive hysteresis-curve of our GMR-stacks both in the normal- and superconducting state.

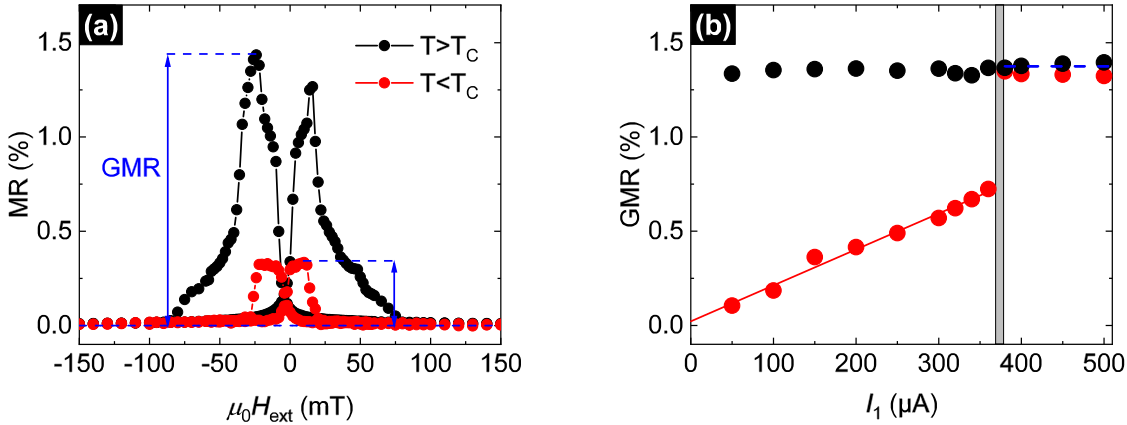


Figure 9.2: (a): Magnetoresistive hysteresis of the GMR spin valves recorded in the normal- and superconducting state for $I_1 = 150 \mu\text{A}$. The relative magnitude and coercitive field of the hard ferromagnet $\text{Fe } H_c^{\text{Fe}}$ is drastically reduced below T_C . (b): Value of the GMR-effect as function of applied current I_1 . The critical current through the NbN-bars is $I_C = (370 \pm 10) \mu\text{A}$. In the superconducting range, it increases linearly with I_1 , while remaining constant in the normal state.

From the results in Fig. 9.2 it becomes apparent that in the superconducting state both magnitude of the GMR effect and width of the hysteresis curve are drastically reduced. Changes in the latter are expected as SQUID-magnetometry measurements for an unstructured sample with identical stack sequence revealed that the coercitive field of the hard ferromagnet $\text{Fe } H_c^{\text{Fe}}$ varies with temperature. A dramatically reduced GMR effect of spinvalves in contact to a superconducting material has been theoretically proposed in Refs. [126, 127]. This effect is attributed to Andreev-reflection where an incident electron can enter the superconducting layer forming a Cooper pair with the retroreflection of a hole of opposite spin but equal momentum [128, 129]. In a simple picture, said reflected hole cancels the GMR as for parallel alignment of \mathbf{M} in both FM, while the spin majority electrons will experience low resistance R , they generate minority holes at the SC/FM-interface reflected back into the spinvalve under high R . Conversely for antiparallel alignment the net resistance for electrons and holes is equal. Consequently, independent of the spin polarization properties of the FM, the same net amount of charge carriers experience enhanced and diminished magnetoresistance within the spin valve in CPP-geometry. Following this train of thought, the finite remaining GMR-effect is generated by both quasiparticle transmission and interfacial spin-flip scattering [126, 130]. This leads us to the last surprising finding of this Master thesis as we find that the GMR magnitude scales linearly with the applied current I_1 in the superconducting phase as illustrated in Fig. 9.2(b). Our result verifies these assumptions, as it is intuitive that the fraction of both transmitting and spin-flipped charge carriers scales linearly with the applied current. Additionally, our fitted linear curve almost perfectly intersects the origin, suggesting a complete suppression of the GMR in absence of these mechanisms. One final open question for this experiment is whether we can somehow enhance either transmission or spin-flip scattering to obtain an enhanced magnetoresistance effect in the superconducting state. This may become possible since the Andreev-reflection is highly sensitive to the coherence length ξ_0 , which can be altered simply by choosing a different superconducting material.

A Appendix: Sample Fabrication

A.1 Sputtering parameters

Target material	P [W]	r [$\text{\AA}/\text{s}$]	T [$^{\circ}\text{C}$]	hysteresis	N_2/Ar -ratio
Nb	120	7.2	RT	-	-
NbN	120	4.0	400	yes	1.9/18.1
$\text{Nb}_{70}\text{Ti}_{30}\text{N}$	54	5.4	700	yes	1.9/18.1

Table A.1: Sputtering parameters of the superconducting materials grown in the SP2. The above were all grown at $p = 5 \times 10^{-3}$ mbar and $\text{MT2}=80$ mm in face-to-face configuration.

Target material	P [W]	r [$\text{\AA}/\text{s}$]	p [10^{-3} mbar]	MT4 position [mm]	type
Al	40	1.4	5.0	70	tilt-in
$\text{Co}_{25}\text{Fe}_{75}$	25	1.0	5.0	40	face-to-face
Co	30	3.8	10.0	70	face-to-face
Cu	30	1.3	5.0	70	tilt-in
Fe	80	1.9	5.0	70	tilt-in
$\text{Ni}_{80}\text{Fe}_{20}$	80	2.1	5.0	70	tilt-in
Pt	30	4.2	5.0	52	face-to-face
SiO_2	35	1.2	5.0	70	tilt-in
Ta	30	0.5	5.0	70	tilt-in
W	45	2.1	5.0	30	face-to-face

Table A.2: Sputtering parameters of the materials grown in the SP4. SiO_2 is RF-sputtered at the parameters $C_{\text{tune}}=726$, $C_{\text{load}}=942$. To ignite the plasma, the pressure is increased to $p = 5 \times 10^{-2}$ mbar and the magnetron shutter is opened.

A.2 Fabrication of the superconducting spin valves

The following section outlines the fabrication process for our superconducting spin valve samples for magnetoresistance measurements at cryogenic temperatures. To this end we spin-coated our samples with a homogeneous positive e-beam resist layer and wrote a previously defined pattern onto it via electron beam lithography. Wherever the resist is exposed to electrons, its chemical composition changes making it removable via the usage of a suitable developer. For deposition and etching processes we again used the Superbowl sputtering machine. It comprises of three major steps: the growth of the superconducting bar itself, the patterning of the GMR-stacks and finally the deposition of Al-contact pads. In the following we will describe the fabrication procedure for each step separately. We note that our used recipe is based on that in [131], where the fabrication process is described in greater detail.

A.2.1 The first step

Fig. A.1 illustrates the pattern that is repeatedly written on a blanketed SiO_2 -substrate. It consists of vertical bars that are contracted underneath the future position of the spinvalves to enlarge the current density in the superconducting layer underneath and consequently the fieldlike torques via Rashba-Edelstein effect. Additionally alignment markers are written at the edges of the substrate to define a coordinate system for the future writing processes.

This pattern is then filled with both the SC-layer and the individual materials comprising the spin-valve in the Superbowl sputtering machine. Finally it is capped with a thin Pt layer, which has not been included in Fig. A.1 for the sake of clarity. The individual parameters for the e-beam-writing- and sputtering process are listed in Tab. A.3.

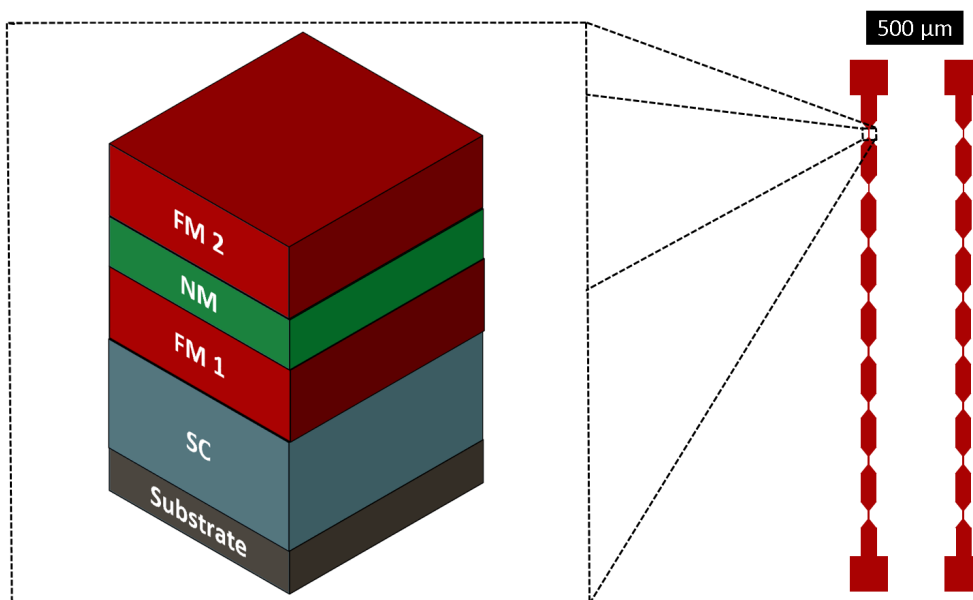


Figure A.1: Pattern of the superconducting GMR spin valve structures after the first step of the fabrication. The bar structure comprising both superconducting ground layer and GMR spinvalve are deposited in the Superbowl sputtering machine.

First step	Details
Resist coating [1]	PMMA 600K: 4000 rpm for 1 min 170 °C for 5 min
Resist coating [2]	PMMA 950K: 4000 rpm for 1 min 170°C for 5 min
Exposure dose	7.0 C/m ² , factor 1.25 for fine structures
Development	[90-120]s in Ar 600-56
Deposition	SV-recipe
Lift-off	2 min in hot Acetone [70 °C] Short US pulses with the lowest power level

Table A.3: Optimized parameters for the first step

A.2.2 The second step

In the next step we pattern the areas of the GMR-stack using the unconventional method of negatively writing a positive resist. The reason for this method is that we needed an etching-durable resist and were unlike [131] not able to use the negative resist maN-2403, which was virtually irremovable from the GMR-pads after etching. Consequently we resorted to the positive PMMA 33% and wrote with a reduced dose in the proximity of the GMR-stacks. In the Superbowl sputtering machine, the surrounding area of the spinvalves is etched down to the superconducting layer and subsequently filled with insulating SiO₂ to even out the surface and avoiding short circuits between SC layer and the Al-contacts structured in the next step. The sample's pattern after the second step is shown in Fig. A.2.

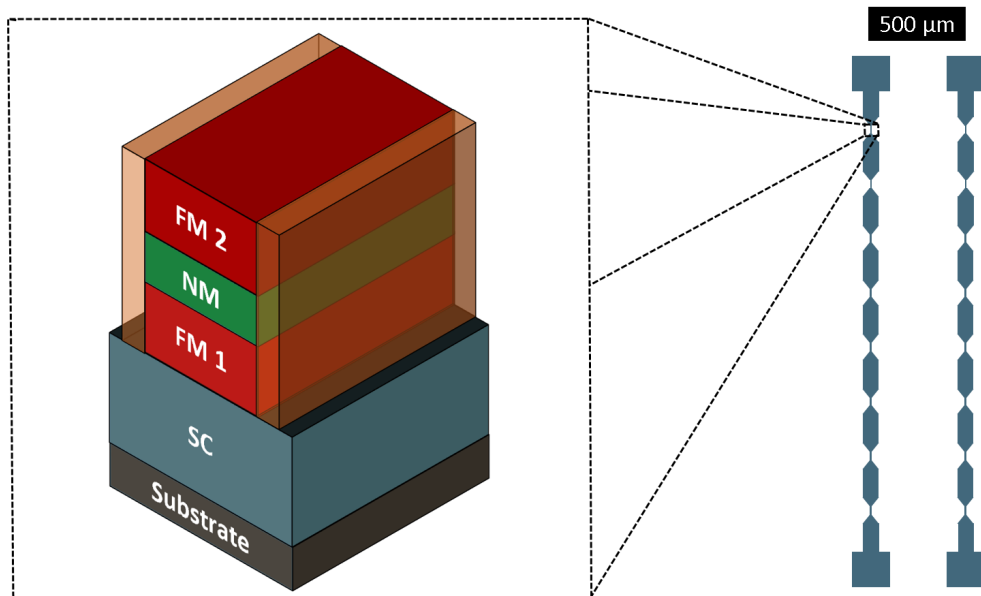


Figure A.2: Pattern of the superconducting GMR spin valve structures after the second step of the fabrication- The bars are etched down to the superconducting layer save for $4 \times 4 \mu\text{m}^2$ GMR-stacks, which are protected by resist. The missing volume is refilled with insulating silicon dioxide to avoid a short circuit between SC and contact pads.

Second step	Details
Resist coating	PMMA 33%: 4000 rpm for 1 min 170°C for 2 min
Exposure dose	6.0 C/m ² , factor 0.75 for the contact pads
Development	[60-90]s in Ar 600-56
Deposition	6 min Etching at EC=0.5 A (Process 1) then SiO ₂ -deposition at MT4=40 mm, P=60 W and tilt-in configuration
Lift-off	2 min in hot Acetone [70 °C] Short US pulses with the lowest power level

Table A.4: Optimized parameters for the second step

A.2.3 The third step

In the last steps, we deposit Al contact $150 \times 200 \mu\text{m}^2$ -pads for wire bonding attached to horizontal bars grown on top of the GMR stack. Furthermore the upper and lower end of the superconducting bar is covered with a contact pad as shown in Fig. A.3.

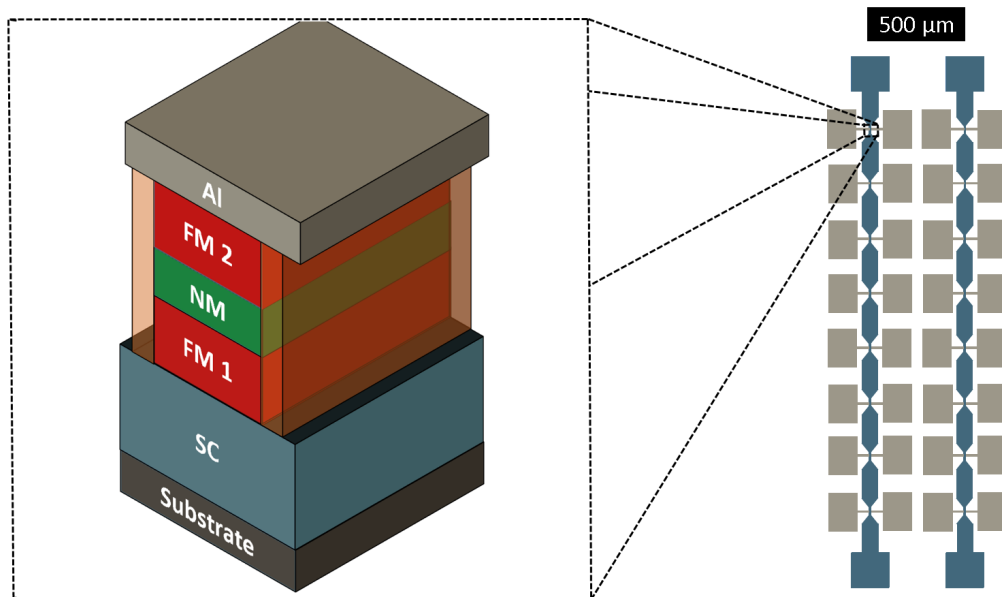


Figure A.3: Pattern of the superconducting GMR spin valve structures after the third step of the fabrication. Horizontal bars of Al are deposited on top of the GMR-stacks together with contact pads for bonding.

Third step	Details
Resist coating [1]	PMMA 600K: 4000 rpm for 1 min 170 °C for 5 min
Resist coating [2]	PMMA 950K: 4000 rpm for 1 min 170 °C for 5 min
Exposure dose	7.0 C/m ² , factor 1.25 for fine structures
Development	[90-120]s in Ar 600-56
Deposition	50 nm Al at MT2=40mm, P=30 W and face-to-face configuration
Lift-off	2 min in hot Acetone [70 °C] Short US pulses with the lowest power level

Table A.5: Optimized parameters for the third step

B Appendix: Miscellaneous Results

B.1 Mathematica code

Mathematica-code used to numerically calculate n_s and Δ .

```
dsc = Pi/Exp[N[EulerGamma, 40]];
N[lambda1 = 8/(7*Zeta[3])];
T = 0.1;
Tc = 10;
r = T/Tc;
Step = 0.1;
Gap = {};
Condensatedensity = {};
TList = {};

For[i = T, T < Tc + Step, i++, r = T/Tc;
gap = Tanh[Pi/dsc*Sqrt[lambda1*(1 - r)/r]];
gapEV =
1000*1.764*Tc*1.38*10^(-23)/(1.6022*10^(-19))*
Tanh[Pi/dsc*Sqrt[lambda1*(1 - r)/r]];
d = dsc/(2*r)*gap; AppendTo[TList, T/Tc]; AppendTo[Gap, gapEV];
AppendTo[Condensatedensity,
1 - NIntegrate[1/(Cosh[Sqrt[t^2 + d^2]])^2, {t, 0, 14}]];
T = T + Step];
data = Transpose@{TList, Gap, Condensatedensity};
Transpose@{TList, Gap, Condensatedensity} // TableForm
condensateplot = Transpose@{TList, Condensatedensity};
Gapplot = Transpose@{TList, Gap};

ListPlot[condensateplot, PlotRange -> {{0, 1}, All}, Axes -> False,
Frame -> True, PlotLabel -> {ns}]
ListPlot[Gapplot, PlotRange -> {{0, 1}, All}, Axes -> False,
Frame -> True, PlotLabel -> {\[CapitalDelta] "(meV)"}]
```

B.2 Additional coherence peaks for NbN/Co₇₅Fe₂₅-heterostructures

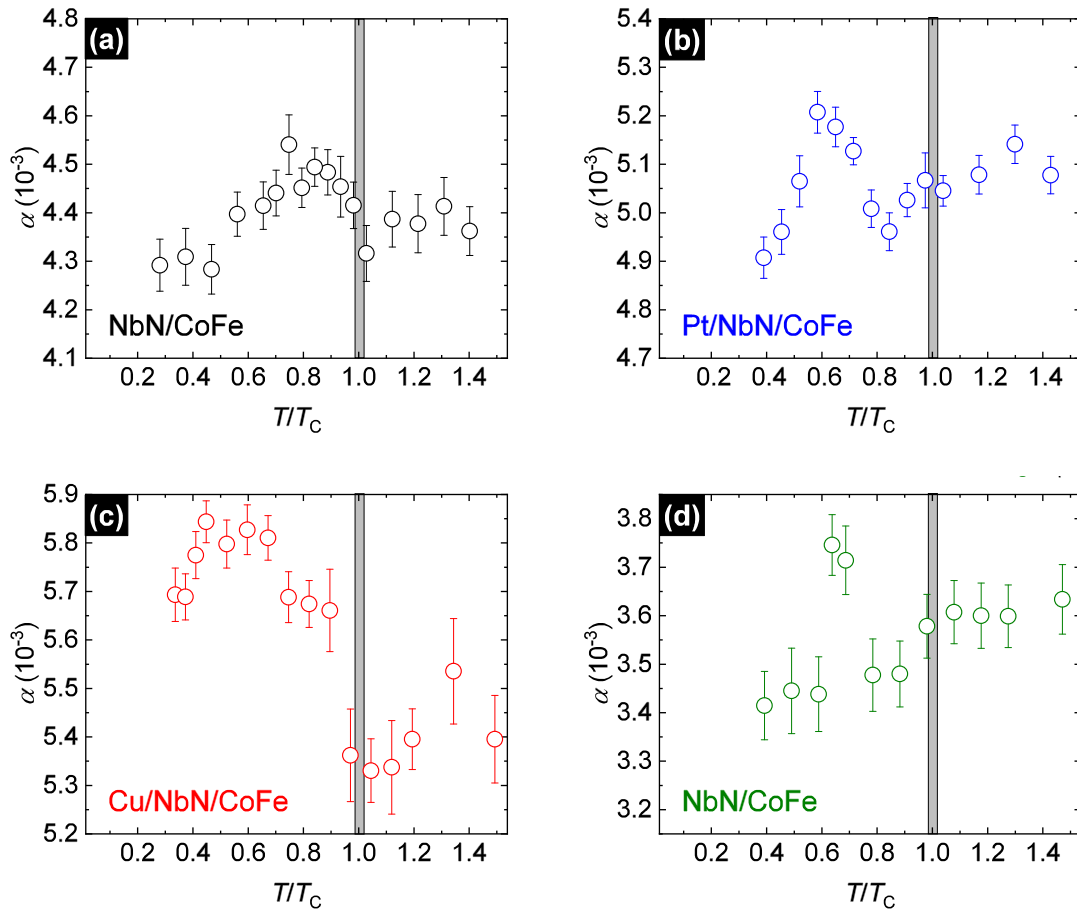


Figure B.1: Gilbert damping α in the temperature range around T_C for various SC/FM-bilayers. The samples in (a)-(c) comprise NbN (16 nm)/Co₇₅Fe₂₅ (3 nm)-samples with varying seedlayers. In (d), the results for a NbN (20 nm)/ Co₇₅Fe₂₅ (6 nm)-bilayer are shown. In all samples a coherence peak at around $[0.7-0.8]T_C$ is visible albeit of different magnitude and temperature width.

B.3 Raw data of the enhancement parameter for varying superconductors

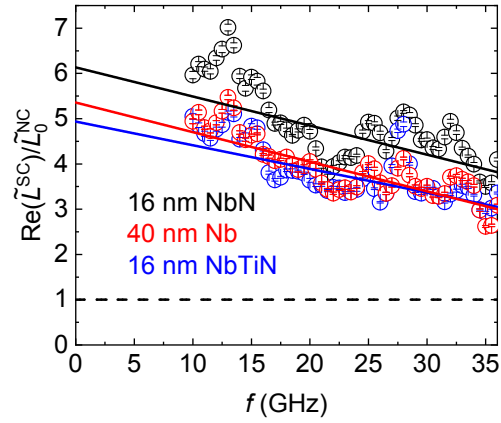


Figure B.2: Raw data of the real part of the inductive coupling $\text{Re}(\tilde{L})$ for varying SC/FM-bilayers with stack sequence [Pt (5 nm)/X/Ni₈₀Fe₂₀ (6 nm)/Ta (2 nm), where X represents Nb (40 nm), Nb₇₀Ti₃₀N (16 nm) and NbN (16 nm) respectively] at $T = 0.5T_C$ normalized to its y-axis intercept \tilde{L}_0^{NC} in the normalconducting range.

B.4 Temperature dependence of magnetization dynamics parameters for NbN/Ni₈₀Fe₂₀-samples

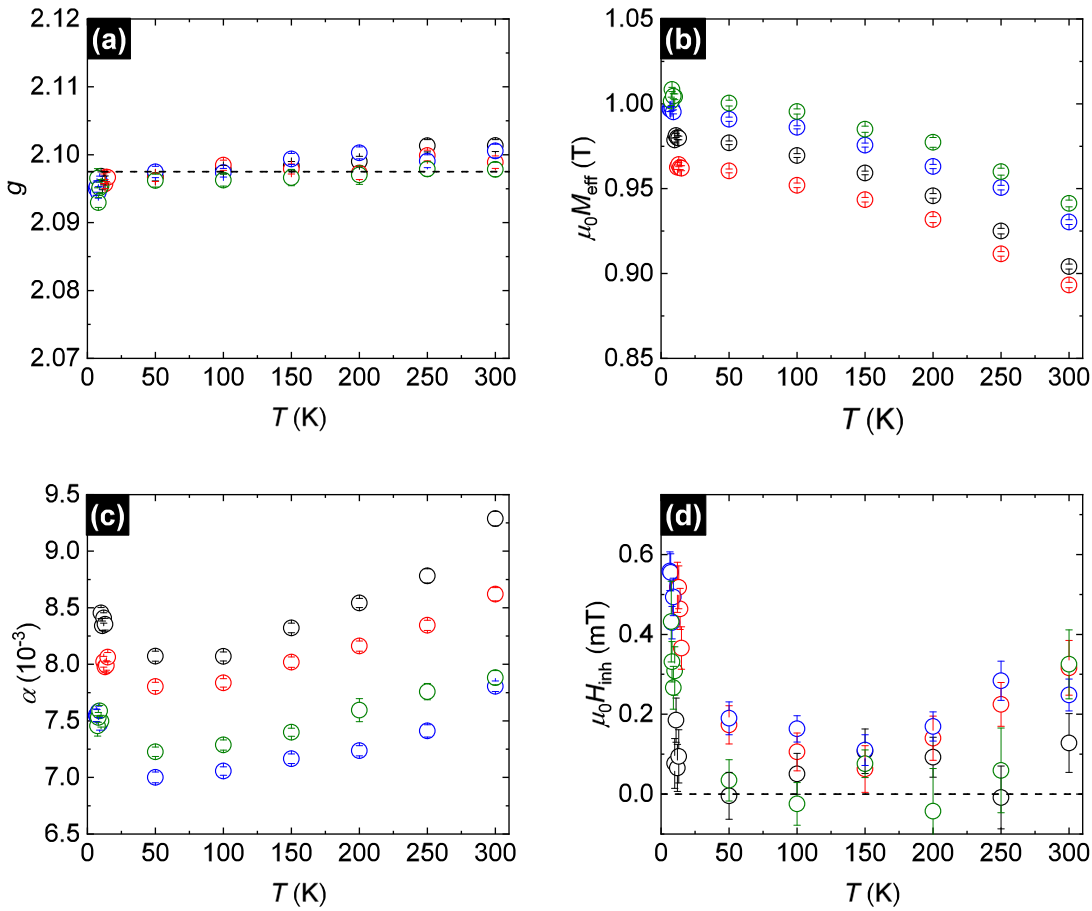


Figure B.3: Temperature dependence of spectroscopic parameters in the normalconducting range for the NbN/Ni₈₀Fe₂₀-samples investigated in the CHAOS-cryostat [See 7.1]. (a): The g -factor displays no clear dependence on T , while the effective magnetization decreases for increasing temperature due to the thermal excitation of magnons. (c) and (d) illustrate the changes of the Gilbert damping α and inhomogeneous broadening $\mu_0 H_{\text{inh}}$ respectively.

References

- [1] D. KAHNG. *A historical perspective on the development of MOS transistors and related devices*. IEEE Trans. Electron Devices **23**, 655–657 (1976), [URL](#).
- [2] W. BINASCH, G. AND GRÜNBERG, P. AND SAURENBACH, F. AND ZINN. *Enhanced magnetoresistance in layered magnetic structures with antiferromagnetic interlayer exchange*. Phys. Rev. B **39**, 4828–4830 (1989), [URL](#).
- [3] M. N. BAIBICH, J. M. BROTO, A. FERT, F. N. VAN DAU, F. PETROFF, P. ETIENNE, G. CREUZET, A. FRIEDERICH AND J. CHAZELAS. *Giant Magnetoresistance of (001)Fe/(001)Cr Magnetic Superlattices*. Phys. Rev. Lett. **61**, 2472–2475 (1988), [URL](#).
- [4] V. GINZBURG. *An experimental manifestation of instability of the normal phase in superconductors*. J. Exptl. Theor. Phys. **8**, 541–543 (1956), [URL](#).
- [5] B. T. MATTHIAS, H. SUHL AND E. CORENZWIT. *Spin Exchange in Superconductors*. Phys. Rev. Lett. **1**, 92–94 (1958), [URL](#).
- [6] S. K. SINHA, G. W. CRABTREE, D. G. HINKS AND H. MOOK. *Study of Coexistence of Ferromagnetism and Superconductivity in Single-Crystal $ErRh_4B_4$* . Phys. Rev. Lett. **48**, 950–953 (1982), [URL](#).
- [7] S. S. SAXENA, P. AGARWAL, K. AHILAN, F. M. GROSCHE, R. K. W. HASELWIMMER, M. J. STEINER, E. PUGH, I. R. WALKER, S. R. JULIAN, P. MONTHOUX, G. G. LONZARICH, A. HUXLEY, I. SHEIKIN, D. BRAITHWAITE AND J. FLOUQUET. *Superconductivity on the border of itinerant-electron ferromagnetism in UGe_2* . Nature **406**, 587–592 (2000), [URL](#).
- [8] F. LEVY. *Magnetic Field-Induced Superconductivity in the Ferromagnet URhGe*. Science (80-.). **309**, 1343–1346 (2005), [URL](#).
- [9] J. S. JIANG, D. DAVIDOVIĆ, D. H. REICH AND C. L. CHIEN. *Oscillatory Superconducting Transition Temperature in Nb/Gd Multilayers*. Phys. Rev. Lett. **74**, 314–317 (1995), [URL](#).
- [10] M. G. KHUSAINOV AND Y. N. PROSHIN. *Possibility of periodically reentrant superconductivity in ferromagnet/superconductor layered structures*. Phys. Rev. B **56**, R14283–R14286 (1997), [URL](#).
- [11] Z. YANG, M. LANGE, A. VOLODIN, R. SZYMCZAK AND V. V. MOSHCHALOV. *Domain-wall superconductivity in superconductor–ferromagnet hybrids*. Nat. Mater. **3**, 793–798 (2004), [URL](#).
- [12] J. FRITZSCHE, V. V. MOSHCHALOV, H. EITEL, D. KOELLE, R. KLEINER AND R. SZYMCZAK. *Local Observation of Reverse-Domain Superconductivity in a Superconductor-Ferromagnet Hybrid*. Phys. Rev. Lett. **96**, 247003 (2006), [URL](#).
- [13] G. BLATTER, V. B. GESHKENBEIN AND L. B. IOFFE. *Design aspects of superconducting-phase quantum bits*. Phys. Rev. B **63**, 174511 (2001), [URL](#).

- [14] A. K. FEOFANOV, V. A. OBOZNOV, V. V. BOL'GINOV, J. LISENFELD, S. POLETO, V. V. RYAZANOV, A. N. ROSSOLENKO, M. KHABIPOV, D. BALASHOV, A. B. ZORIN, P. N. DMITRIEV, V. P. KOSHELETS AND A. V. USTINOV. *Implementation of superconductor/ferromagnet/superconductor π -shifters in superconducting digital and quantum circuits*. Nat. Phys. **6**, 593–597 (2010), [URL](#).
- [15] Y. A. IZYUMOV, Y. N. PROSHIN AND M. G. KHUSAINOV. *Competition between superconductivity and magnetism in ferromagnet/superconductor heterostructures*. Physics-Uspekhi **45**, 109–148 (2002), [URL](#).
- [16] T. NACHTRAB, D. KOELLE, R. KLEINER, C. BERNHARD AND C. T. LIN. *Intrinsic Josephson Effects in the Magnetic Superconductor $RuSr_2GdCu_2O_8$* . Phys. Rev. Lett. **92**, 117001 (2004), [URL](#).
- [17] J. Y. GU, C.-Y. YOU, J. S. JIANG, J. PEARSON, Y. B. BAZALIY AND S. D. BADER. *Magnetization-Orientation Dependence of the Superconducting Transition Temperature in the Ferromagnet-Superconductor-Ferromagnet System: $CuNi/Nb/CuNi$* . Phys. Rev. Lett. **89**, 267001 (2002), [URL](#).
- [18] I. C. MORARU, W. P. PRATT AND N. O. BIRGE. *Magnetization-dependent shift in ferromagnet/superconductor/ferromagnet trilayers with a strong ferromagnet*. Phys. Rev. Lett. **96**, 037004 (2006), [URL](#).
- [19] M. INOUE, M. ICHIOKA AND H. ADACHI. *Spin pumping into superconductors: A new probe of spin dynamics in a superconducting thin film*. Phys. Rev. B **96**, 024414 (2017), [URL](#).
- [20] T. KATO, Y. OHNUMA, M. MATSUO, J. RECH, T. JONCKHEERE AND T. MARTIN. *Microscopic theory of spin transport at the interface between a superconductor and a ferromagnetic insulator*. Phys. Rev. B **99**, 144411 (2019), [URL](#).
- [21] J. LINDER AND J. W. A. ROBINSON. *Superconducting spintronics*. Nat. Phys. **11**, 307–315 (2015), [URL](#).
- [22] R. S. KEIZER, S. T. B. GOENNENWEIN, T. M. KLAPWIJK, G. MIAO, G. XIAO AND A. GUPTA. *A spin triplet supercurrent through the half-metallic ferromagnet CrO_2* . Nature **439**, 825–827 (2006), [URL](#).
- [23] K.-R. JEON, C. CICCARELLI, A. J. FERGUSON, H. KUREBAYASHI, L. F. COHEN, X. MONTIEL, M. ESCHRIG, J. W. A. ROBINSON AND M. G. BLAMIRE. *Enhanced spin pumping into superconductors provides evidence for superconducting pure spin currents*. Nat. Mater. **17**, 499–503 (2018), [URL](#).
- [24] N. POLI, J. P. MORTEN, M. URECH, A. BRATAAS, D. B. HAVILAND AND V. KORENIVSKI. *Spin Injection and Relaxation in a Mesoscopic Superconductor*. Phys. Rev. Lett. **100**, 136601 (2008), [URL](#).
- [25] H. YANG, S.-H. YANG, S. TAKAHASHI, S. MAEKAWA AND S. S. P. PARKIN. *Extremely long quasiparticle spin lifetimes in superconducting aluminium using MgO tunnel spin injectors*. Nat. Mater. **9**, 586–593 (2010), [URL](#).

- [26] J. Y. GU, J. A. CABALLERO, R. D. SLATER, R. LOLOEE AND W. P. PRATT. *Direct measurement of quasiparticle evanescent waves in a dirty superconductor*. Phys. Rev. B **66**, 140507 (2002), [URL](#).
- [27] Y. TSEKOVNYAK, A. BRATAAS AND G. E. W. BAUER. *Spin pumping and magnetization dynamics in metallic multilayers*. Phys. Rev. B **66**, 224403 (2002), [URL](#).
- [28] Y. YAO, Q. SONG, Y. TAKAMURA, J. P. CASCALES, W. YUAN, Y. MA, Y. YUN, X. C. XIE, J. S. MOODERA AND W. HAN. *Probe of spin dynamics in superconducting NbN thin films via spin pumping*. Phys. Rev. B **97**, 224414 (2018), [URL](#).
- [29] A. J. BERGER, E. R. EDWARDS, H. T. NEMBACH, A. D. KARENOWSKA, M. WEILER AND T. J. SILVA. *Inductive detection of fieldlike and dampinglike ac inverse spin-orbit torques in ferromagnet/normal-metal bilayers*. Phys. Rev. B **97**, 94407 (2018), [URL](#).
- [30] T. WAKAMURA, H. AKAIKE, Y. OMORI, Y. NIIMI, S. TAKAHASHI, A. FUJIMAKI, S. MAEKAWA AND Y. OTANI. *Quasiparticle-mediated spin Hall effect in a superconductor*. Nat. Mater. **14**, 675–678 (2015), [URL](#).
- [31] K.-R. JEON, C. CICCARELLI, H. KUREBAYASHI, J. WUNDERLICH, L. F. COHEN, S. KOMORI, J. W. A. ROBINSON AND M. G. BLAMIRE. *Spin-Pumping-Induced Inverse Spin Hall Effect in Nb/Ni₈₀Fe₂₀ Bilayers and its Strong Decay Across the Superconductor*. Phys. Rev. Appl. **10**, 014029 (2018), [URL](#).
- [32] N. N. BOGOLJUBOV. *On a new method in the theory of superconductivity*. Nuovo Cim. **7**, 794–805 (1958), [URL](#).
- [33] J. G. VALATIN. *Comments on the theory of superconductivity*. Nuovo Cim. **7**, 843–857 (1958), [URL](#).
- [34] J. BARDEEN, L. N. COOPER AND J. R. SCHRIEFFER. *Theory of Superconductivity*. Phys. Rev. **108**, 1175–1204 (1957), [URL](#).
- [35] M. REICHERT. *Hochwertige supraleitende Dünnschichten für fortgeschrittene Spinelektronik*, Bachelor thesis, Technische Universität München (2018), [URL](#).
- [36] L. FLACKE. *Spin-Pumping and Spin Wave Damping in Co₂₅Fe₇₅ Thin-Film Heterostructures*, Master thesis, Technische Universität München (2018), [URL](#).
- [37] *Visual science: Technical illustration of magnetron sputtering technology* (accessed: 29.08.2019), [URL](#).
- [38] A. ANDERS. *Tutorial: Reactive high power impulse magnetron sputtering (R-HiPIMS)*. J. Appl. Phys. **121**, 171101 (2017), [URL](#).
- [39] H. HEDBABNY AND H. ROGALLA. *dc and rf magnetron sputter deposition of NbN films with simultaneous control of the nitrogen consumption*. J. Appl. Phys. **63**, 2086–2090 (1988), [URL](#).

- [40] D. M. GLOWACKA, D. J. GOLDIE, S. WITHINGTON, H. MUHAMMAD, G. YASSIN AND B. K. TAN. *Development of a NbN Deposition Process for Superconducting Quantum Sensors* **XX**, 1–6 (2014), [URL](#).
- [41] G. HORN AND E. SAUR. *Präparation und Supraleitungseigenschaften von Niobnitrid sowie Niobnitrid mit Titan-, Zirkon- und Tantalzusatz*. *Zeitschrift für Phys. A Hadron. Nucl.* **210**, 70–79 (1968), [URL](#).
- [42] D. HAZRA, N. TSAVDARIS, S. JEBARI, A. GRIMM, F. BLANCHET, F. MERCIER, E. BLANQUET, C. CHAPELIER AND M. HOFHEINZ. *Superconducting properties of very high quality NbN thin films grown by high temperature chemical vapor deposition*. *Supercond. Sci. Technol.* **29**, 105011 (2016), [URL](#).
- [43] M. CHAND, A. MISHRA, Y. M. XIONG, A. KAMLAPURE, S. P. CHOCKALINGAM, J. JESUDASAN, V. BAGWE, M. MONDAL, P. W. ADAMS, V. TRIPATHI AND P. RAYCHAUDHURI. *Temperature dependence of resistivity and Hall coefficient in strongly disordered NbN thin films*. *Phys. Rev. B* **80**, 134514 (2009), [URL](#).
- [44] L. FLACKE, L. LIENSBERGER, M. ALTHAMMER, H. HUEBL, S. GEPRÄGS, K. SCHULTHEISS, A. BUZDAKOV, T. HULA, H. SCHULTHEISS, E. R. J. EDWARDS, H. T. NEMBACH, R. SHAW, JUSTIN M. AND AND M. WEILER. *New Spin-Wave Propagation Length Scales in Low Damping Metallic Ferromagnets* **2**, 2–6 (2019), [URL](#).
- [45] M. A. W. SCHOEN, D. THONIG, M. L. SCHNEIDER, T. J. SILVA, H. T. NEMBACH, O. ERIKSSON, O. KARIS AND J. M. SHAW. *Ultra-low magnetic damping of a metallic ferromagnet*. *Nat. Phys.* **12**, 839–842 (2016), [URL](#).
- [46] V. HOLY', J. KUBĚNA, I. OHLÍDAL, K. LISCHKA AND W. PLOTZ. *X-ray reflection from rough layered systems*. *Phys. Rev. B* **47**, 15896–15903 (1993), [URL](#).
- [47] L. G. PARRATT. *Surface Studies of Solids by Total Reflection of X-Rays*. *Phys. Rev.* **95**, 359–369 (1954), [URL](#).
- [48] S. K. SINHA, E. B. SIROTA, S. GAROFF AND H. B. STANLEY. *X-ray and neutron scattering from rough surfaces*. *Phys. Rev. B* **38**, 2297–2311 (1988), [URL](#).
- [49] C. R. A. CATLOW, J. M. THOMAS, C. M. FREEMAN, P. A. WRIGHT AND R. G. BELL. *Simulating and Predicting Crystal Structures*. *Proc. R. Soc. A Math. Phys. Eng. Sci.* **442**, 85–96 (1993), [URL](#).
- [50] H. KAHLER. *The Crystalline Structures of Sputtered and Evaporated Metallic Films*. *Phys. Rev.* **18**, 210–217 (1921), [URL](#).
- [51] D. POLDER. *On the theory of ferromagnetic resonance*. *Physica* **15**, 253–255 (1949), [URL](#).
- [52] C. KITTEL. *On the Theory of Ferromagnetic Resonance Absorption*. *Phys. Rev.* **73**, 155–161 (1948), [URL](#).
- [53] R. GROSS AND A. MARX. *Festkörperphysik* (De Gruyter, Berlin, Boston, 2018), 3 edn., [URL](#).

- [54] W. BUCKEL AND R. KLEINER. *Supraleitung* (Wiley-VCH Verlag GmbH & Co. KGaA, Weinheim, Germany, 2012), [URL](#).
- [55] A. GROSS, RUDOLF AND MARX. *Applied Superconductivity Chapter 8: Microwave Applications* (2005), [URL](#).
- [56] F. LONDON AND H. LONDON. *The electromagnetic equations of the supraconductor*. Proc. R. Soc. London. Ser. A - Math. Phys. Sci. **149**, 71–88 (1935), [URL](#).
- [57] W. MEISSNER AND R. OCHSENFELD. *Ein neuer Effekt bei Eintritt der Supraleitfähigkeit*. Naturwissenschaften **21**, 787–788 (1933), [URL](#).
- [58] A. I. GUBIN, K. S. IL'IN, S. A. VITUSEVICH, M. SIEGEL AND N. KLEIN. *Dependence of magnetic penetration depth on the thickness of superconducting Nb thin films*. Phys. Rev. B **72**, 064503 (2005), [URL](#).
- [59] A. A. ABRIKOSOV. *Magnetic properties of superconductors of the second group*. JETP **5**, 1174–1182 (1957), [URL](#).
- [60] P. E. GOA, H. HAUGLIN, M. BAZILJEVICH, E. IL'YASHENKO, P. L. GAMMEL AND T. H. JOHANSEN. *Real-time magneto-optical imaging of vortices in superconducting NbSe₂*. Supercond. Sci. Technol. **14**, 729–731 (2001), [URL](#).
- [61] V. L. GINZBURG AND L. D. LANDAU. *On the Theory of superconductivity*. Zh. Eksp. Teor. Fiz. **20**, 1064–1082 (1950), [URL](#).
- [62] A. B. PIPPARD AND W. L. BRAGG. *An experimental and theoretical study of the relation between magnetic field and current in a superconductor*. Proc. R. Soc. London. Ser. A. Math. Phys. Sci. **216**, 547–568 (1953), [URL](#).
- [63] A. KAMLAPURE, M. MONDAL, M. CHAND, A. MISHRA, J. JESUDASAN, V. BAGWE, L. BENFATTO, V. TRIPATHI AND P. RAYCHAUDHURI. *Measurement of magnetic penetration depth and superconducting energy gap in very thin epitaxial NbN films*. Appl. Phys. Lett. **96**, 072509 (2010), [URL](#).
- [64] S. KUBO, M. ASAHI, M. HIKITA AND M. IGARASHI. *Magnetic penetration depths in superconducting NbN films prepared by reactive dc magnetron sputtering*. Appl. Phys. Lett. **44**, 258–260 (1984), [URL](#).
- [65] D. EINZEL. *Theory of Superconductivity* (2008), [URL](#).
- [66] D. EINZEL. *Universal Parameters in the Response of Unconventional Superconductors*. J. Low Temp. Phys. **126**, 867–879 (2002), [URL](#).
- [67] D. EINZEL. *Interpolation of BCS response functions*. J. Low Temp. Phys. **130**, 493–509 (2003), [URL](#).
- [68] K. YOSIDA. *Paramagnetic Susceptibility in Superconductors*. Phys. Rev. **110**, 769–770 (1958), [URL](#).

- [69] J. M. MACLAREN, T. C. SCHULTHESS, W. H. BUTLER, R. SUTTON AND M. MCHENRY. *Electronic structure, exchange interactions, and Curie temperature of FeCo*. J. Appl. Phys. **85**, 4833–4835 (1999), [URL](#).
- [70] W. HEISENBERG. *Mehrkörperproblem und Resonanz in der Quantenmechanik*. Zeitschrift für Phys. **38**, 411–426 (1926), [URL](#).
- [71] T. GILBERT. *Classics in Magnetism A Phenomenological Theory of Damping in Ferromagnetic Materials*. IEEE Trans. Magn. **40**, 3443–3449 (2004), [URL](#).
- [72] L. LIENSBERGER. *Spin-Orbit Torques and Magnetization Dynamics in Non-collinear Magnets*. Masters Thesis , Master thesis, Technische Universität München (2017), [URL](#).
- [73] L. DREHER, M. WEILER, M. PERNPEINTNER, H. HUEBL, R. GROSS, M. S. BRANDT AND S. T. B. GOENNENWEIN. *Surface acoustic wave driven ferromagnetic resonance in nickel thin films: Theory and experiment*. Phys. Rev. B **86**, 134415 (2012), [URL](#).
- [74] D. D. STANCIL AND A. PRABHAKAR. *Spin Waves* (Springer US, Boston, MA, 2009), [URL](#).
- [75] B. LAX, K. J. BUTTON AND H. J. HAGGER. *Microwave Ferrites and Ferrimagnetics*. Phys. Today **16**, 57–58 (1963), [URL](#).
- [76] P. D. LOUIS. *Broadband-Spectroscopy of Magnetic Materials at Low Temperatures* , Master thesis, Technische Universität München (2016), [URL](#).
- [77] J.-M. BEAUJOUR, D. RAVELOSONA, I. TUDOSA, E. E. FULLERTON AND A. D. KENT. *Ferromagnetic resonance linewidth in ultrathin films with perpendicular magnetic anisotropy*. Phys. Rev. B **80**, 180415 (2009), [URL](#).
- [78] D. HUERTAS HERNANDO, Y. V. NAZAROV, A. BRATAAS AND G. E. W. BAUER. *Conductance modulation by spin precession in noncollinear ferromagnet normal-metal ferromagnet systems*. Phys. Rev. B **62**, 5700–5712 (2000), [URL](#).
- [79] A. BRATAAS, Y. TSEKOVNYAK AND G. E. BAUER. *Spin-pumping in ferromagnet-normal metal systems*. J. Magn. Magn. Mater. **272-276**, 1981–1982 (2004), [URL](#).
- [80] M. A. W. SCHOEN, J. M. SHAW, H. T. NEMBACH, M. WEILER AND T. J. SILVA. *Radiative damping in waveguide-based ferromagnetic resonance measured via analysis of perpendicular standing spin waves in sputtered permalloy films*. Phys. Rev. B **92**, 184417 (2015), [URL](#).
- [81] A. J. BERGER, E. R. J. EDWARDS, H. T. NEMBACH, O. KARIS, M. WEILER AND T. J. SILVA. *Determination of the spin Hall effect and the spin diffusion length of Pt from self-consistent fitting of damping enhancement and inverse spin-orbit torque measurements*. Phys. Rev. B **98**, 024402 (2018), [URL](#).
- [82] J.-C. ROJAS-SÁNCHEZ, N. REYREN, P. LACZKOWSKI, W. SAVERO, J.-P. ATTANÉ, C. DERANLOT, M. JAMET, J.-M. GEORGE, L. VILA AND H. JAFFRÈS. *Spin Pumping and Inverse Spin Hall Effect in Platinum: The Essential Role of Spin-Memory Loss at Metallic Interfaces*. Phys. Rev. Lett. **112**, 106602 (2014), [URL](#).

- [83] A. A. ABRIKOSOV, L. P. GORKOV, I. E. DZHALOSHINSKI, R. A. SILVERMAN AND G. H. WEISS. *Methods of Quantum Field Theory in Statistical Physics*. Phys. Today **17**, 78–80 (1964), [URL](#).
- [84] O. KARLQVIST. *Calculation of the Magnetic Field in the Ferromagnetic Layer of a Magnetic Drum*. Acta polytechnica (Elanders boktr.; H. Lindståhls bokhandel i distribution, 1954), [URL](#).
- [85] H. T. NEMBACH, T. J. SILVA, J. M. SHAW, M. L. SCHNEIDER, M. J. CAREY, S. MAAT AND J. R. CHILDRESS. *Perpendicular ferromagnetic resonance measurements of damping and Landé g-factor in sputtered $(Co_2Mn)_{1-x}Ge_x$ thin films*. Phys. Rev. B **84**, 054424 (2011), [URL](#).
- [86] F. HARTZ. *Herstellung eines Breitband-Messstabs zur Untersuchung ferromagnetischer Resonanz* 65 (2014), [URL](#).
- [87] H. B. MAIER-FLAIG. *Magnetic resonance of ferrimagnetic insulators*, PhD thesis, Technische Universität München (2017), [URL](#).
- [88] C. T. BOONE, J. M. SHAW, H. T. NEMBACH AND T. J. SILVA. *Spin-scattering rates in metallic thin films measured by ferromagnetic resonance damping enhanced by spin-pumping*. J. Appl. Phys. **117**, 223910 (2015), [URL](#).
- [89] C. BELL, S. MILIKISYANTS, M. HUBER AND J. AARTS. *Spin Dynamics in a Superconductor-Ferromagnet Proximity System*. Phys. Rev. Lett. **100**, 047002 (2008), [URL](#).
- [90] S. P. CHOCKALINGAM, M. CHAND, J. JESUDASAN, V. TRIPATHI AND P. RAYCHAUDHURI. *Superconducting properties and Hall effect of epitaxial NbN thin films*. Phys. Rev. B **77**, 214503 (2008), [URL](#).
- [91] K. ROGDAKIS, A. SUD, M. AMADO, C. M. LEE, L. MCKENZIE-SELL, K. R. JEON, M. CUBUKCU, M. G. BLAMIRE, J. W. A. ROBINSON, L. F. COHEN AND H. KUREBAYASHI. *Spin transport parameters of NbN thin films characterized by spin pumping experiments*. Phys. Rev. Mater. **3**, 014406 (2019), [URL](#).
- [92] B. MÜHLSCHLEGEL. *Die thermodynamischen Funktionen des Supraleiters*. Zeitschrift für Phys. **155**, 313–327 (1959), [URL](#).
- [93] G.-X. MIAO, A. V. RAMOS AND J. S. MOODERA. *Infinite Magnetoresistance from the Spin Dependent Proximity Effect in Symmetry Driven bcc-Fe/V/Fe Heteroepitaxial Superconducting Spin Valves*. Phys. Rev. Lett. **101**, 137001 (2008), [URL](#).
- [94] J. P. MORTEN, A. BRATAAS, G. E. W. BAUER, W. BELZIG AND Y. TSERKOVNYAK. *Proximity-effect-assisted decay of spin currents in superconductors*. EPL (Europhysics Lett. **84**, 57008 (2008), [URL](#).
- [95] H. GŁOWIŃSKI, M. SCHMIDT, I. GOŚCIAŃSKA, J.-P. ANSERMET AND J. DUBOWIK. *Coplanar waveguide based ferromagnetic resonance in ultrathin film magnetic nanostructures: Impact of conducting layers*. J. Appl. Phys. **116**, 053901 (2014), [URL](#).

- [96] C. GORTER AND H. CASIMIR. *On supraconductivity I*. *Physica* **1**, 306–320 (1934), [URL](#).
- [97] E. SILVA, N. POMPEO AND O. V. DOBROVOLSKIY. *Vortices at Microwave Frequencies*. *Phys. Sci. Rev.* **2**, 1–16 (2017), [URL](#).
- [98] E. B. ROSA. *The self and mutual-inductances of linear conductors*. *Bull. Bur. Stand.* **4**, 301 (1908), [URL](#).
- [99] A. J. ANNUNZIATA, D. F. SANTAVICCA, L. FRUNZIO, G. CATELANI, M. J. ROOKS, A. FRYDMAN AND D. E. PROBER. *Tunable superconducting nanoinductors*. *Nanotechnology* **21**, 445202 (2010), [URL](#).
- [100] P. NATZKIN. *Superconducting Microwave Resonator Designs for Electron Spin Resonance Applications*, Master thesis, Technische Universität München (2017), [URL](#).
- [101] L. YU, R. SINGH, H. LIU, S. WU, R. HU, D. DURAND, J. BULMAN, J. ROWELL AND N. NEWMAN. *Fabrication of Niobium Titanium Nitride Thin Films With High Superconducting Transition Temperatures and Short Penetration Lengths*. *IEEE Trans. Applied Supercond.* **15**, 44–48 (2005), [URL](#).
- [102] I. M. MIRON, K. GARELLO, G. GAUDIN, P.-J. ZERMATTEN, M. V. COSTACHE, S. AUFFRET, S. BANDIERA, B. RODMACQ, A. SCHUHL AND P. GAMBARDELLA. *Perpendicular switching of a single ferromagnetic layer induced by in-plane current injection*. *Nature* **476**, 189–193 (2011), [URL](#).
- [103] S. LOWITZER, M. GRADHAND, D. KÖDDERITZSCH, D. V. FEDOROV, I. MERTIG AND H. EBERT. *Extrinsic and Intrinsic Contributions to the Spin Hall Effect of Alloys*. *Phys. Rev. Lett.* **106**, 056601 (2011), [URL](#).
- [104] J. SINOVA, S. O. VALENZUELA, J. WUNDERLICH, C. H. BACK AND T. JUNGWIRTH. *Spin Hall effects*. *Rev. Mod. Phys.* **87**, 1213–1260 (2015), [URL](#).
- [105] P. M. HANEY, H.-W. LEE, K.-J. LEE, A. MANCHON AND M. D. STILES. *Current induced torques and interfacial spin-orbit coupling: Semiclassical modeling*. *Phys. Rev. B* **87**, 174411 (2013), [URL](#).
- [106] K. GARELLO, I. M. MIRON, C. O. AVCI, F. FREIMUTH, Y. MOKROUSOV, S. BLÜGEL, S. AUFFRET, O. BOULLE, G. GAUDIN AND P. GAMBARDELLA. *Symmetry and magnitude of spin-orbit torques in ferromagnetic heterostructures*. *Nat. Nanotechnol.* **8**, 587–593 (2013), [URL](#).
- [107] Y. A. BYCHKOV AND É. I. RASHBA. *Properties of a 2D electron gas with a lifted spectral degeneracy*. *JETP Lett.* **39**, 78–81 (1984), [URL](#).
- [108] V. EDELSTEIN. *Spin polarization of conduction electrons induced by electric current in two-dimensional asymmetric electron systems*. *Solid State Commun.* **73**, 233–235 (1990), [URL](#).
- [109] L. ONSAGER. *Reciprocal Relations in Irreversible Processes. I*. *Phys. Rev.* **37**, 405–426 (1931), [URL](#).

- [110] E. SILVA, N. POMPEO AND S. SARTI. *Wideband microwave measurements in Nb/Pd₈₄Ni₁₆/Nb-structures and comparison with thin Nb films*. *Supercond. Sci. Technol.* **24**, 024018 (2011), [URL](#).
- [111] S. TAKAHASHI AND S. MAEKAWA. *Spin Hall Effect in Superconductors*. *Jpn. J. Appl. Phys.* **51**, 010110 (2012), [URL](#).
- [112] S. TAKAHASHI AND S. MAEKAWA. *Spin Current in Metals and Superconductors*. *J. Phys. Soc. Japan* **77**, 031009 (2008), [URL](#).
- [113] H. KONTANI, J. GORYO AND D. S. HIRASHIMA. *Intrinsic Spin Hall Effect in the s-Wave Superconducting State: Analysis of the Rashba Model*. *Phys. Rev. Lett.* **102**, 086602 (2009), [URL](#).
- [114] S. TAKAHASHI AND S. MAEKAWA. *Hall Effect Induced by a Spin-Polarized Current in Superconductors*. *Phys. Rev. Lett.* **88**, 116601 (2002), [URL](#).
- [115] S. TAKAHASHI, T. YAMASHITA, H. IMAMURA AND S. MAEKAWA. *Spin-relaxation and magnetoresistance in FM/SC/FM tunnel junctions*. *J. Magn. Magn. Mater.* **240**, 100–102 (2002), [URL](#).
- [116] F. HÜBLER, M. J. WOLF, D. BECKMANN AND H. V. LÖHNEYSSEN. *Long-Range Spin-Polarized Quasiparticle Transport in Mesoscopic Al Superconductors with a Zeeman Splitting*. *Phys. Rev. Lett.* **109**, 207001 (2012), [URL](#).
- [117] S. NADJ-PERGE, I. K. DROZDOV, J. LI, H. CHEN, S. JEON, J. SEO, A. H. MACDONALD, B. A. BERNEVIG AND A. YAZDANI. *Observation of Majorana fermions in ferromagnetic atomic chains on a superconductor*. *Science* **346**, 602–607 (2014), [URL](#).
- [118] I. V. BOBKOVA, A. M. BOBKOV AND M. A. SILAEV. *Spin torques and magnetic texture dynamics driven by the supercurrent in superconductor/ferromagnet structures*. *Phys. Rev. B* **98**, 014521 (2018), [URL](#).
- [119] S. MIRONOV AND A. BUZDIN. *Spontaneous Currents in Superconducting Systems with Strong Spin-Orbit Coupling*. *Phys. Rev. Lett.* **118**, 1–7 (2017), [URL](#).
- [120] S. MIRONOV, A. S. MEL'NIKOV AND A. BUZDIN. *Electromagnetic proximity effect in planar superconductor-ferromagnet structures*. *Appl. Phys. Lett.* **113**, 022601 (2018), [URL](#).
- [121] Y. MASUDA AND A. G. REDFIELD. *Nuclear Spin-Lattice Relaxation in Superconducting Aluminum*. *Phys. Rev.* **125**, 159–163 (1962), [URL](#).
- [122] L. C. HEBEL AND C. P. SLICHTER. *Nuclear Spin Relaxation in Normal and Superconducting Aluminum*. *Phys. Rev.* **113**, 1504–1519 (1959), [URL](#).
- [123] E. SILVA, N. POMPEO, K. TOROKHTII AND S. SARTI. *Wideband Surface Impedance Measurements in Superconducting Films*. *IEEE Trans. Instrum. Meas.* **65**, 1120–1129 (2016), [URL](#).

-
- [124] J. R. GAVALER, M. A. JANOCKO, A. PATTERSON AND C. K. JONES. *Very High Critical Current and Field Characteristics of Niobium Nitride Thin Films*. J. Appl. Phys. **42**, 54–57 (1971), [URL](#).
- [125] K. ILIN, D. HENRICH, Y. LUCK, Y. LIANG, M. SIEGEL AND D. Y. VODOLAZOV. *Critical current of Nb, NbN, and TaN thin-film bridges with and without geometrical nonuniformities in a magnetic field*. Phys. Rev. B **89**, 184511 (2014), [URL](#).
- [126] F. TADDEI, S. SANVITO, J. H. JEFFERSON AND C. J. LAMBERT. *Suppression of Giant Magnetoresistance by a Superconducting Contact*. Phys. Rev. Lett. **82**, 4938–4941 (1999), [URL](#).
- [127] A. VEDYAYEV, D. BAGRETS, A. BAGRETS, N. RYZHANOVA, N. STRELKOV, B. DIENY AND C. LACROIX. *The mechanisms of suppression and enhancement of GMR and TMR in magnetic sandwiches*. J. Magn. Magn. Mater. **242-245**, 453–456 (2002), [URL](#).
- [128] A. F. ANDREEV. *The thermal conductivity of the intermediate state in superconductors*. Sov. Phys. JETP **19**, 1228 (1964), [URL](#).
- [129] G. E. BLONDER, M. TINKHAM AND T. M. KLAPWIJK. *Transition from metallic to tunneling regimes in superconducting microconstrictions: Excess current, charge imbalance, and supercurrent conversion*. Phys. Rev. B **25**, 4515–4532 (1982), [URL](#).
- [130] S. WANG, L. TANG AND K. XIA. *Spin transfer torque in the presence of Andreev reflections*. Phys. Rev. B **81**, 094404 (2010), [URL](#).
- [131] M. SCHLEUDER. *Tunneling Spectroscopy in Conductive Ferromagnets*, Master thesis, Technische Universität München (2017), [URL](#).

Acknowledgements

During my work on this thesis, I received a lot of help from several people, without which, this thesis would not have been possible. In particular, I would like to thank:

Prof. Dr. Rudolf Gross for offering me the opportunity to write my Master's thesis here at the Walther-Meißner-Institut (WMI)

Dr. Matthias Althammer for offering me this Master's thesis topic and for being an outstanding supervisor. I am grateful for his open door policy, where he offered open ears for my countless questions and outlandish explanation attempts of my results. Our continuous discussions and exchange of research papers throughout this year has enabled me to derive a coherent picture on the vast field of superconducting spintronics. Furthermore, I would like to say thank you for his proof-reading of this thesis and finally for offering me a PhD position to continue my research in this field.

Dr. Mathias Weiler for providing insight on VNA-based BBFMR and the physics of spin-orbit torques. He also answered many of my questions and offered many suggestions for further experiments. In particular, without his vast input, the chapter on SOT in superconductors would not have been possible. Moreover, I am grateful for his proof-reading of this thesis.

Dr. Matthias Opel for helping me out with various SQUID-issues. Although I didn't include any SQUID-data in this thesis, the ability to quickly determine the superconducting transition temperature of my samples via magnetometry measurements was very helpful.

Dr. Hans Huebl for his additional input, manifold explanatory suggestions and genuine interest in my research.

Dr. Dietrich Einzel for handing me his notes for the calculations of the BCS-theory parameters.

Luis Flacke for teaching me how to use the Superbowl sputtering machine, the Laserwriter and how to conduct VNA-based BBFMR. Additionally, he helped me with countless experimental issues and readily shared his insights and ideas with me.

Lukas Liensberger for providing me with a Mathematica script to quantify the iSOT conductivities and teaching me, how to process my data with Python. Through my discussions with him I learned a lot on spin-orbit torques, but also Spintronics in general.

Tobias Wimmer for teaching me how to use the e-Beam and tremendously helping me out with the sample fabrication process of the GMR-spinvalves. Without him, I would probably not have been able to fabricate a working sample.

Tom Brenninger for helping me to develop a new sample mounting method for BBFMR in the CHAOS.

The master student crew. In particular Andreas Faltermeier and Adrian Gomez for helping me out with several issues. Moreover the people in WMI 108, Raffael Ferdig, Robert Neagu and Leander Peis offered endless comic relief from the boring office routine.

The entire "Magnetiker"-group for accepting me with open arms. Everyone offered an open ear for my problems and physics-related questions.

The entire staff of the WMI for the kind work atmosphere.

My parents, Heike and Michael Müller, for their unconditional support throughout this year. Furthermore, I appreciate your genuine interest in my research, despite its relative inaccessibility. In particular, thank you for funding my study in Munich and being there for me, when I need you.